

Biomolecules in Nanoporous Structures

by

Ya Zhou

A thesis submitted in partial fulfillment of the requirements for the degree of

Doctor of Philosophy

Department of Chemistry  
University of Alberta

© Ya Zhou, 2017

## ABSTRACT

Nanomaterials have been widely involved in biomolecular analysis, to refine traditional analytical method or develop complementary techniques. In this thesis, nanoporous structures were utilized in two applications, DNA electrophoresis and solid matrix laser desorption ionization (SMALDI).

Microfabricated devices utilizing ratchet based motion of DNA may offer a far more rapid method for large DNA fragment separation, useful in genetic studies. However, on-chip separation of megabase-sized DNA in nanoporous colloidal self-assembled (CSA) structures within microfluidic devices is limited by DNA trapping, a phenomenon that also limits the speed and efficiency of gel electrophoresis. Megabase-sized DNA is crucial to modern genomics research of all organisms. In chapter 2, we investigated the mechanism of DNA trapping in silica nanoporous structure. We found the primary reason for DNA trapping is the reduced mobility of apex segments of U/J shaped DNA. The pinning of the apex and the thriving of near-apex hernias result in an irreversible trapping conformation of DNA molecule in the separation sieves. Insulator-based dielectrophoresis (DEP) originates from the structure of the separation sieves and is proposed to be the source of the external force on apex segments. The presence of DEP during DNA electrophoretic separation and its effects are often neglected since DEP force is considerably weaker than electrophoretic force. However, we found the perturbation by DEP force at apex confounds the Ratchet model which regulates the DNA motion and separation mechanism by pulsed-field electrophoresis. This clear trapping mechanism contrasts with those for trapping in gels, which give no clear explanation for a strong field dependence. Using reverse or

intermittent field spikes greatly increases the field strength available, allowing much more rapid separations than in gels.

In another work, porous silicon thin film fabricated by glancing angle deposition (GLAD) was utilized for the solid matrix laser desorption ionization (SMALDI). Not involving the organic matrix in the laser desorption ionization (LDI) process, SMALDI is suitable for analyzing small molecules, particularly metabolites, with a simple spot test. However, salt and other sample matrix components in biofluids greatly reduce the performance of SMALDI as a metabolite assay. Herein, we describe a unique approach to surface modification that gives an on-line sample preparation method for SMALDI and possibly other porous silicon based LDI techniques. The approach separates ionic metabolites, such as amino acids, and dominant background electrolytes, which are usually so similar in solubility and hydrophobicity that they are not readily separated by a surface enhanced LDI approach, instead requiring the more laborious and method of LC-MS. The background electrolytes are directly segregated through crystallization on perfluoro coated SMALDI surface, which are prepared with coating defects to cause the salt segregation during spot drying. Combined with desalting, the quantitative analysis of metabolites in salty samples (serum and artificial cerebrospinal fluid) by SMALDI-MS is improved, and the technique has potential to be applied to metabolite profiling in batches.

## **PREFACE**

The literature review in Chapter 1, and Chapter 2 are my original work. Chapter 2 has been published as Y. Zhou, H. Sheng, and D.J. Harrison, “Mechanism of DNA Trapping in Nanoporous Structures during Asymmetric Pulsed-field Electrophoresis,” *Analyst*, 2014, vol. 139, issue 22, 6044-6051. I was responsible for experimental design, data collection, data analysis and interpretation and manuscript drafting. Huiying Sheng assisted with the data collection. D. Jed Harrison was the supervisory author and was involved with concept formation and manuscript composition.

In Chapter 3 and Chapter 4, the development of sample cleanup method, biofluid sample analysis by SMALDI-MS and the customization of TOF/TOF mass spectrometer for SMALDI are my original work. The perfluoro coating on SMALDI for low mass analysis was developed by Chen Peng. The results of pure sample analysis in Chapter 3 were summarized from Peng’s thesis chapter. Chapter 3 and a portion of Chapter 4 have been submitted for publication. The manuscript is under revision. Chen Peng, Ken Harris, Rupasri Mandal are co-authors. Harris contributed to GLAD film fabrication, and Mandal contributed to the NMR analysis. Jed Harrison is the supervisory author. He was involved with concept formation and responsible for manuscript drafting and revision.

## ACKNOWLEDGEMENT

At this moment, I feel I made a right decision to complete a PhD program. The past five years have always been meaningful. It is a challenging and precious journey, and the valuable trainings that I have received will have a very positive impact on my future life and career. Here, I would like to express my gratitude to some people who helped and supported me during my PhD study.

I would like to thank my supervisor, Dr. Jed Harrison, who offered great support and respect to my research. I am very grateful to all the opportunities that he has provided for developing my capability. I feel fortunate to have worked for him, and more importantly, be influenced by him.

I would have not achieved any success in my project without helps from the collaborators. Huiying Sheng and Chen Peng were my former labmates and mentors. All of my work in this thesis is based on their previous research. I sincerely thank them for training me with great patience. I would like to thank Ken Harris and Rupa Mandal for their collaboration and insightful discussions. There are so many people who have provided excellent technical support to my research. They are Randy Whittal, Bela Reiz and Jing Zheng from Mass Spectrometry Lab, Gareth Lambkin from Biological Service at Chemistry Department, and many Nanofab Staffs. I would like to thank them and other staffs at Chemistry Department. They did a wonderful job day by day, and year by year, and their professionalism inspired me.

I would like to thank my supervisory committees, Dr. Charles Lucy and Dr. Julianne Gibbs-Davis, for their kind advises during the past years. We had awkward meetings every

year, discussing about my future career and post-graduate plans, but I feel so grateful that there was somebody who tried to push me forward and suggested me prepare for the future.

I thank other exam committees Dr. Mark Mcdermott, Dr. Michael Serpe and Dr. David Shriemer for coming to my defense and providing constructive comments on my work. I thank Dr. Mcdermott for serving on my supervisory committee, after Dr. Lucy's retirement.

Many thanks to other group members in DJH group for their support and friendship. Chemistry Department is populated by talented and friendly scientists and graduate students. I learned a lot from them.

Finally, I thank my parents for their love. This thesis is dedicated to them.



|           |   |    |
|-----------|---|----|
| 1.4       | Thesis outline.....   | 27 |
| <br>      |   |    |
| Chapter 2 | Mechanism of DNA Trapping in Nanoporous Structures during<br>Asymmetric Pulsed Field Electrophoresis .....                                | 29 |
| 2.1       | Introduction.....   | 29 |
| 2.2       | Experimental.....   | 31 |
| 2.3       | Results and discussions .....   | 35 |
| 2.3.1     | Macroscopic behavior of T4 DNA trapping .....   | 35 |
| 2.3.2     | Dynamics of single DNA trapping and the role of hernias .....   | 38 |
| 2.3.3     | Role of hooking.....  | 44 |
| 2.3.4     | Dielectrophoretic trapping.....   | 49 |
| 2.4       | Conclusion .....  | 53 |
| <br>      |   |    |
| Chapter 3 | Salt Segregation and Sample Cleanup on Perfluoro-coated<br>Nanostructured Surfaces for Laser Desorption Ionization Mass Spectrometry..... | 55 |
| 3.1       | Introduction.....   | 56 |
| 3.2       | Experimental section .....  | 58 |
| 3.2.1     | SMALDI chip preparation .....   | 58 |
| 3.2.2     | Sample preparation.....   | 59 |
| 3.2.3     | Sample deposition and on-chip desalting.....  | 60 |
| 3.2.4     | Mass spectrometry .....   | 60 |
| 3.2.5     | Quantitative analysis .....   | 61 |
| 3.3       | Results and discussion .....  | 61 |
| 3.3.1     | Perfluoro coating improvements for low mass analytes .....  | 61 |
| 3.3.2     | Segregation of salt interferences on perfluoro surfaces.....  | 64 |
| 3.4       | Conclusions .....   | 72 |

|             |   |     |
|-------------|---|-----|
| Chapter 4   | Serum Metabolite Analysis by SMALDI-MS .....                  | 73  |
| 4.1         | Introduction.....   | 73  |
| 4.2         | Experimental section .....                                    | 74  |
| 4.2.1       | SMALDI chip preparation .....                                 | 74  |
| 4.2.2       | Serum sample preparation.....                                 | 74  |
| 4.2.3       | Quantitative analysis by MS and NMR.....                      | 75  |
| 4.3         | Results and discussion .....                                  | 76  |
| 4.3.1       | Serum sample analysis.....                                    | 76  |
| 4.3.2       | SMALDI on Bruker UltrafleXtreme .....                         | 84  |
| 4.4         | Conclusions .....   | 91  |
| Chapter 5   | Concluding Remarks and Future Work.....                       | 92  |
| 5.1         | Concluding remarks .....                                      | 92  |
| 5.2         | Future work.....  | 94  |
| References  | .....   | 98  |
| Appendix A: | Rational for using 105 nm por size.....                       | 111 |
| Appendix B: | Video list .....  | 112 |
| Appendix C: | Effective charge density <i><math>\rho_{eff}</math></i> ..... | 114 |
| Appendix D: | Debye length and high field gradient region .....             | 115 |
| Appendix E: | Quantitative analysis.....                                    | 117 |
| appendix F: | .....   | 118 |

## LIST OF TABLES

|  |    |
|--|----|
| Table 2-1: Parameters of forward pulses and reversed spikes .....  | 37 |
| Table 3-1: Artificial CSF (aCSF) composition and concentration (pH=7.3) .....  | 59 |
| Table 3-2: Instrument Settings of MALDI-TOF-MS .....   | 61 |
| Table 4-1: The concentrations of metabolites in human serum quantified by SMALDI-MS<br>and NMR, compared with the normal concentrations in blood ..... | 81 |
| Table 4-2: The putative metabolites for peaks detected in human serum in negative ion<br>mode by SMALDI-MS .....                                       | 83 |
| Table 4-3: The optimal instrument settings for SMALDI-MS on UltrafleXtreme (negative<br>ion mode) .....  | 87 |

## LIST OF FIGURES

Figure 1-1: A) SEM image of post arrays and fluorescent images of labeled DNA molecules undergoing pulsed field electrophoresis in microfabricated arrays. The DNA is reoriented as the electric field is switched. B) Sketches of the mechanism of DNA separation through APFE and a fluorescence image showing deflection bands. C) Design of the microfluidic device developed by Zeng et al, SEM image of silica crystalline arrays and sketch of 3D nanopore generated by crystalline arrays. Reprinted with permissions from A) ref [19] © 1996 VCH Verlagsgesellschaft mbH, B) ref [13] © 2002 Nature Publishing Group and C) ref [20] © 2008 WILEY-VCH Verlag GmbH & Co. KGaA. .... 5

Figure 1-2: a) Separation of yeast chromosomes in gel electrophoresis. The DNA were first separated by pulsed fields in the left lane and then driven to the right lane by DC field. Trapping and band smearing are obvious. The numbers indicate DNA sizes in megabase pair unit. b-d) DNA trapping mechanisms proposed in several papers. Reprinted with permission from a-b) ref [28] © 1990 Oxford University Press, c) ref [14] © 1992 VCH Verlagsgesellschaft mbH and d) ref [15] © 1999 The National Academy of Sciences. .... 9

Figure 1-3: a) Conformations of stretched DNA in strong confinement, weak confinement and bulk solution. b) Time-lapse images showing the process of single DNA molecule colliding with obstacle, forming U/J shape and unhooking. c) Time-lapse images showing formation and evolution of hernias after electric field was switched. Reprinted with permission from a) ref [52] © 2011 American Chemical Society, b) ref

[22] © 2004 American Chemical Society and c) ref [53] © 1990 American Chemical Society. .... 12

Figure 1-4: a) The DEP trapping of DNA in PDMS microarrays. b) The dipole moment of DNA molecule induced by electric field. c) The deformation of electric field in PDMS microarrays. Reprinted with permission from a) ref [75] © 2004 American Chemical Society, b) ref [76] © 2013 American Chemical Society and c) ref [77] © 2009 The American Physical Society. .... 15

Figure 1-5: a) Sketch of DIOS-MS. b) SEM image of DIOS chip fabricated by electrochemical etching of silicon wafer. c) Sketch of GLAD process. d) SEM image of vertical silicon nanocolumns fabricated through GLAD. Reprinted with permission from a) ref [87] © 1999 Nature Publishing Group, b) ref [90] © 2001 American Chemical Society, c) ref [123] © 2012 Zdenek Michalcik et al and d) ref [117] © 1997 American Vacuum Society. .... 20

Figure 1-6: a) (1H, 1H, 2H, 2H-perfluorooctyl)trichloro silane ( $\text{pFSiCl}_3$ ) silanization on Si GLAD film surfaces. b and c) Mass spectra of 200 pmol histidine obtained on b) uncoated and c)  $\text{pFSiCl}_3$  modified Si GLAD films, in negative ion mode. Reprinted with permission from ref [139] © 2014 Chen Peng. .... 23

Figure 2-1: a) Schematic of the microchip for DNA separation. The separation bed and microchannels are filled with a colloidal crystal of silica particles, except for the injection channel. b) Fluorescence micrograph (4X objective) of deflection band of a T4 DNA plug under asymmetric pulsed field electrophoresis (APFE).  $E_1$  and  $E_2$  are two square wave pulses in APFE.  $E_1 = \sqrt{2} E_2$ . Frequency is 0.5 Hz. The dashed line

represents the position for measuring fluorescent intensity. c) SEM image of the polycrystalline silica (690 nm diameter) in the separation bed. .... 34

Figure 2-2: a-d) Migration of a T4 DNA plug in the separation bed captured by fluorescence microscope (10X objective). The field strengths of asymmetric pulsed-fields  $E_1$  and  $E_2$  were 202.0 V/cm and 142.9 V/cm, respectively, with 0.5 Hz frequency. The time trace started at the beginning of 2D separation. In c), continuous injection was stopped, creating an empty injection channel and a plug of injected material. e) The intensity profile along the blue arrow in d), showing some DNA was trapped in the sieves and did not continue along with the main sample plug..... 36

Figure 2-3: a) Intensity-time curves at several fields pulsed at 0.5Hz. Intensity was measured 0.54 cm downstream (dashed line in Figure 2-1b). Time was normalized by field strength. Trapped DNA causes a broad band, while mobile DNA gives sharper spikes. b) Effect of reversed spikes on DNA trapping at high electric field.  $E_2 = 142.9$  V/cm,  $f = 0.5$ Hz. .... 38

Figure 2-4: TIRF micrograph of a single DNA trapped in APFE.  $E_2 = 142.9$  V/cm,  $f = 2$  Hz. a) DNA collides with, then hooks around a silica particle. b) Hernias form after electric field switches. c) The conformation of trapped DNA at 2 Hz. The process of single DNA being trapped at the same field strength, but 0.5 Hz, was recorded and is displayed in video 2-3..... 39

Figure 2-5: a) The comb-like conformation of hernias after electric field switching. Apart from the apex segments, which should lead the molecule's reorientation according to the ratchet model, other segments responding to the field are labelled as hernias. For all studied molecules, the length of hernias was measured every 33 ms after the field

was switched to  $E_2$ . For the molecule shown in the image, the total length of hernias =  $2h_1+h_2$ . a-c) The total lengths of hernias are shown as a function of time at several field strengths, with 50 molecules presented in each graph. The red lines in c) represent the duration time of the  $E_2$  portion of the field pulse on the x-axis for the frequencies indicated. d) 30 hernias formed at  $E_2 = 142.9$  V/cm were identified as either distant hernias or near-apex hernias (within  $2.8 \mu\text{m}$  of the apex, 5% of contour length). The evolution traces isolated for distant hernias is shown in d), indicating all the long lasting hernias in c) are near-apex hernias. .... 41

Figure 2-6: Time-lapse images of video F4. DNA is trapped at 0.5 Hz. In b), both near-apex hernia (red arrow) and distant hernias (orange arrow) form. The green arrow points at the apex segment which has reoriented, along with the near-apex hernia pointed by the red arrow. The distant hernia disappears with time as seen in c), while the near-apex hernia is substantially stretched. As an overall result, the apex is immobilized. .... 43

Figure 2-7: a) Scheme of “rope-on-pulley” model. The negatively charged molecule should slip away from the J-shape under the external electric field  $E_1$ , due to the unequal lengths of the two arms. b-d) Unhooking times of U/J shaped DNA at different electric fields. The solid lines follow the theoretical model of Randall et al. with  $\beta = 0$ . The red lines follow the modified model of Equation 2-7, for the maximum of  $\beta$  as determined at different field strengths. Dots represent experimental unhooking times. Red dots represent infinite unhooking time, appearing at 1.5 s on the y-axis. The solid dots represent the first data set which was obtained from complete sample statistics in several TIRF videos. The hollow dots represent a second data set which only focused

on shorter  $x_1$ . e) Scaling relation between dielectrophoresis parameter  $\beta$  and electric field strength. .... 47

Figure 2-8: Simulation results of electric field gradient  $\nabla E^2$  in the nanoporous structure. The permittivity of 4X TBE buffer and silica particle are  $77.232 \epsilon_0$  [193] and  $4.2 \epsilon_0$ , respectively. The conductivity of buffer and silica are 0.22 and  $1 \times 10^{-10}$  S/m, respectively. The direction of applied electric field is from left to right. Field strength  $E$  is non-uniform in the nanoporous structure. a) Field strength  $E$  is non-uniform in the nanoporous structure. b-c) Field gradient  $\nabla E^2$  plotted in 2D graphs, showing b) the gradient on the silica surface, as a projection of the upper surface onto a plane passing through the particle's centre, parallel to the direction of the field, and c) a two-dimensional slice taken along the same plane, showing the field gradient in the pore. Red is high field gradient, blue is low. d) Field gradient on a selected buffer-silica interface (blue arc in the inset). The red, green and blue lines represent the field gradient at an average field  $E_1 = 202.0, 161.6$  and  $101.0$  V/cm, respectively. .... 51

Figure 3-1: Mass spectra of a) 10 b) 2 and c) 1  $\mu\text{M}$  pure histidine solution obtained on a 1% concentration pFSiCl<sub>3</sub> SMALDI chip. .... 64

Figure 3-2: a) The nanostructured Si thin films fabricated using GLAD, wherein silicon is evaporated and deposited at an incidence angle of  $86^\circ$  onto silicon wafers, forming vertical nanocolumns. In b) and c), artificial cerebral spinal fluid (aCSF) was deposited on a pFSiCl<sub>3</sub> coated SMALDI chip (1% pFSiCl<sub>3</sub> coating concentration). Salt in the aCSF formed a thick layer, masking the nanoporous structure. (See Appendix F for the SEM image showing the entire sample spot.) 10  $\mu\text{M}$  histidine spiked in aCSF was not ionized and detected by SMALDI-MS. In d-f), the same

sample was deposited on a pFSiCl<sub>3</sub> surface (pFSiCl<sub>3</sub> coated at 0.3% concentration to give a 120° contact angle) and slowly dried at 4 °C in a closed chamber. After slow air-drying, the background electrolyte formed large crystals. Many of the nanopores are salt-free, in contrast to the salt deposits in b). The MS measurements were taken in regions without visible crystals. The interference from salt was greatly reduced. The [His-H]<sup>+</sup> peak at m/z 154.0 was detected. The asterisks mark background peaks at m/z 112.9 and 199.9..... 67

Figure 3-3: a) S/N of 10 μM histidine spiked in aCSF on perfluoro coated SALDI surfaces with different contact angles. b) The contact angles on fluorinated SALDI surfaces, controlled by varying the silane, the silane coating concentration and the storage times of GLAD films (1 day – 6 months). The leftmost line is for pFSiCl<sub>3</sub> coatings on a 3-month old surface; the other lines are for pFMe<sub>2</sub>SiCl coatings, differentiated by GLAD film storage times before surface modification. The error bar in b) is SD of 9 individual measurements. c) The relationship between S/N (lines), noise (shadow) and coating concentration. Red represents the 3-month old film and black represents the 6-month old film. The samples were dried in humid chamber at 4°C (solid lines) or room temperature (dash line), and the duration times of drying are ~5 h and ~1 h, respectively. Slow air drying amplifies the desalting performance, and could consistently be associated with the appearance of a few large salt crystals. Referring to b), the S/N significantly decreases on superhydrophobic surfaces, independent of film age and drying time. .... 69

Figure 3-4: A mass spectrum of aCSF sample containing leucine, glutamine, histidine, and tyrosine, 20  $\mu\text{M}$  for each, obtained on 0.3% concentration pFSiCl<sub>3</sub> SMALDI chip with slow air drying. .... 70

Figure 3-5: The internal standard calibration curves of histidine in aCSF using 20  $\mu\text{M}$  a) 1-methylhistidine, b) glutamine and c) asparagine as internal standards. The linearity ranges are 1-100  $\mu\text{M}$  in a) and 2-50  $\mu\text{M}$  in b) and c). The error bar represents SD of 10 individual measurements. .... 71

Figure 4-1: Workflow for biofluid sample analysis by SMALDI, including silicon GLAD film surface silanization, deproteinization by ultrafiltration, on-chip desalting through segregated salt crystallization and SMALDI-MS acquisition. .... 77

Figure 4-2: SMALDI-MS spectra of human serum. The serum samples were deproteinized through ultrafiltration, and then acidified in b) and c) by adding HCl. The samples were desalted on 1.2 % pFMe<sub>2</sub>SiCl coated SMALDI chips during slow air drying. .. 78

Figure 4-3: SMALDI-MS for the analysis of metabolites in human serum. The deproteinated serum was spotted on a pFMe<sub>2</sub>SiCl SMALDI coated chip (1.2% coating concentration) and slowly air dried. The salt in the sample aggregated in a small region of the dried sample spot, as observed under a) optical and b) helium ion microscope. c) shows the nanopores are salt free after the sample deposition, but there is some nanocolumn clumping. The MS measurements in d) and e) were taken in regions without visible crystals, obtained in negative and positive ion modes, respectively. The mass spectra of serum metabolites in the low mass range are assigned in accompanying tables. .... 78

Figure 4-4: The standard addition curves of a) malic acid, b) aspartic acid, c) glutamic acid and d) taurine in human serum. SMALDI chips were coated with a 1.2% concentration of pFMe<sub>2</sub>SiCl, 120° contact angle. Before deproteinization by ultrafiltration, 0.5 ml serum was mixed with standard solution and subsequently diluted to 1 ml. The x-axis in a-d) represents the final concentration of the standard in the 1 ml mixture. Therefore, the readings at y=0 represents half of the analyte concentrations in the serum sample. The error bar is the SD of 9 individual measurements..... 80

Figure 4-5: The coefficients of variation (CVs) of the peak heights at a) m/z 100-250 (negative ion mode) and b) m/z 110-300 (positive ion mode). The CVs were calculated from mass spectra of 8 serum sample spots on SMALDI chips. Excluding the peaks with S/N less than 20, 36 and 34 peaks were detected in negative mode. Red Xs in a) represent the five quantified metabolites in Table 4-1. .... 82

Figure 4-6: Mass spectra of a) 15 pmol (10 μM) histidine and b) deproteinated human serum deposited on 1.2 % pFMe<sub>2</sub>SiCl coated SMALDI film, taken in negative ion mode using UltrafleXtreme. .... 89

Figure 4-7: Schematic of time-lag ion source..... 89

Figure 4-8: a) MS and b) MS/MS spectra of CHCA saturated solution (water/acetonitrile, 50/50) acquired in negative mode. The sample was spotted on 1% pFSiCl<sub>3</sub> coated SMALDI chip. In a), the m/z peaks at 189.9, 188.0 and 144.0 represent [M]<sup>-</sup>, [M-H]<sup>-</sup> and [M-CO<sub>2</sub>H]<sup>-</sup> ions, respectively, consistent with the record on MassBank ([www.massbank.jp](http://www.massbank.jp), Accession: MCH00004)..... 91

## List of Symbols and Abbreviations

### Symbols:

|                        |   |
|------------------------|---|
| $D$                    | Diameter of pore size                                 |
| $E$                    | Electric field strength                               |
| $E_1$                  | The higher electric field in APFE                     |
| $E_2$                  | The lower electric field in APFE                      |
| $E_{\text{crit}}$      | Critical field strength for trapping                  |
| $E^*$                  | Electric field of reverse spike                       |
| $F_{\text{ext}}$       | External force at the apex of U/J shaped DNA          |
| $g_r$                  | Radius of gyration                                    |
| $I$                    | Ionic strength  |
| $j$                    | Number of base pairs on the short arm of J shaped DNA |
| $L$                    | DNA contour length                                    |
| $N$                    | Number of base pairs of DNA                           |
| $q_{\text{eff}}$       | Effective charge density of DNA                       |
| $T$                    | Intramolecular tension                                |
| $t_{\text{unhooking}}$ | Unhooking time  |
| $t_{\text{or}}$        | Reorientation time                                    |
| $w$                    | Width of DNA molecule                                 |
| $x_1$                  | Length of the short arm of U/J shaped DNA             |
| $\Delta x$             | Length difference of two arms of U/J shaped DNA       |

|              |  |
|--------------|--|
| $\alpha$     | Molecular polarizability                           |
| $\beta$      | Defined DEP parameter                              |
| $\epsilon_0$ | Vacuum permittivity                                |
| $\epsilon_b$ | Permittivity of 4x TBE buffer                      |
| $\lambda_D$  | Debye length                                       |
| $\mu$        | Mobility in confined structure                     |
| $\mu_0$      | Mobility in free solution                          |
| $\eta$       | Viscosity  |
| $\xi$        | Hydrodynamic friction coefficient                  |
| $\xi_0$      | Hydrodynamic friction coefficient in free solution |

### **Abbreviations:**

|      |   |
|------|---|
| APFE | Asymmetric pulsed field electrophoresis |
| CHCA | $\alpha$ -Cyano-4-hydroxycinnamic acid  |
| CPD  | Critical point drying                   |
| CSA  | Colloidal self-assembly                 |
| CSF  | Cerebrospinal fluid                     |
| CV   | Coefficient of variance                 |
| aCSF | Artificial cerebrospinal fluid          |
| DEP  | Dielectrophoresis                       |
| iDEP | Insulator based dielectrophoresis       |

|                        |  |
|------------------------|--|
| DIOS                   | Desorption ionization on silicon                     |
| ESI                    | Electrospray ionization                              |
| FAA                    | Free amino acid                                      |
| GC                     | Gas chromatography                                   |
| GLAD                   | Glancing angle deposition                            |
| HMDB                   | Human metabolome data base                           |
| IS                     | Internal standard                                    |
|                        | Ion source voltage                                   |
| ITO                    | Indium tin oxide                                     |
| LC                     | Liquid chromatography                                |
| LDI                    | Laser desorption ionization                          |
| LOD                    | Limit of detection                                   |
| LOQ                    | Limit of quantitation                                |
| MALDI                  | Matrix assisted laser desorption ionization          |
| MS                     | Mass spectrometry                                    |
| MW                     | Molecular weight                                     |
| m/z                    | Mass to charge ratio                                 |
| NIMS                   | Nanostructure-initiator mass spectrometry            |
| NMR                    | Nuclear magnetic resonance                           |
| pAD                    | Probable Alzheimer's disease                         |
| PFGE                   | Pulsed field gel electrophoresis                     |
| pFMe <sub>2</sub> SiCl | (1H, 1H, 2H, 2H-perfluorooctyl) dimethylchlorosilane |
| pFSiCl <sub>3</sub>    | (1H, 1H, 2H, 2H-perfluorooctyl)trichloro silane      |

|        |  |
|--------|--|
| PIE    | Pulsed ion extraction                        |
| pSi    | Porous silicon                               |
| RPLC   | Reverse phase liquid chromatography          |
| SALDI  | Surface assisted laser desorption ionization |
| SMALDI | Solid matrix laser desorption ionization     |
| S/N    | Signal to noise ratio                        |
| TIRF   | Total internal reflection fluorescence       |
| TOF    | Time of flight                               |

# CHAPTER 1 INTRODUCTION

## 1.1 Overview: Nanostructured material and biomolecules

Nanotechnology converges with biology and medicine through various applications of nanomaterials in biomolecular detection,[1, 2] drug delivery,[3-5] enzymatic reaction,[6] biological sample preparation,[7] etc. Generally, nano devices for biomolecule analysis were designed utilizing unique mechanical, optical or chemical properties of nanomaterials.[8, 9] Among all the advantages offered by nanomaterials, in this thesis, we focus on highly engineered nanoporous materials, utilizing their uniform and easily controlled structure to simplify the complicated problems in biomolecule analysis.

This chapter reviews how two conventional biomolecule analysis techniques, DNA gel electrophoresis and laser desorption ionization (LDI), were refined through adoption of nanoporous materials. In Chapter 2, crystalline nanoparticle arrays serve as separation sieves for DNA pulsed field electrophoresis. The ordered nanoporous structure is believed to provide a uniform pore size. We investigated the mechanism of DNA trapping during pulsed field electrophoresis, which severely limits the efficiency in DNA electrophoretic separation. In Chapter 3 and 4, silicon nanoporous thin film were applied as a solid matrix for LDI, reducing chemical interference generated from conventional matrix assisted LDI, to achieve low detection limits for small molecules. The thin films were fabricated by glancing angle deposition (GLAD) which is a highly engineered fabrication process allowing fine control of the nanostructure. We developed a novel on-chip desalting

technique for GLAD film based LDI and applied it in direct analysis of metabolites in biological samples.

## **1.2 Size-based DNA separation in micro- and nanostructures**

### **1.2.1 Introduction**

This section briefly reviews the use of nanostructured materials and lab-on-a-chip technologies for rapid DNA separation. Pulsed field gel electrophoresis (PFGE) is a routine method for separating large DNA molecules. It is mainly used in epidemiological studies, typing chromosomal DNAs for bacteria isolates.[10] However, PFGE is criticized for being time-consuming and labour-intensive, typically taking more than 24 h, due to the low electric field ( $< 8$  V/cm) applied.[11] The field strength is limited by Joule heating, and by trapping and shearing of DNA in the gels.[12] The development of asymmetric pulsed field electrophoresis (APFE) on microfluidic devices achieved continuous fractionation of DNA molecules, significantly improving the efficiency.[13] However, trapping of large DNA molecules[14, 15] was not solved by these new techniques, and the simple separation model, the ratchet mechanism,[16] does not predict the observed trapping in nanostructures. Therefore, more complex and predictive models of DNA motion during electrophoresis are also reviewed in this section.

### **1.2.2 Rapid DNA separation using microfabricated devices**

Volkmuth and Austin first used microlithographically fabricated arrays (Figure 1A) as an alternative medium for DNA electrophoresis in 1992 and demonstrated DNA mobility

dependent upon to ~100 kbp using DC electrophoresis, establishing that separations should be feasible.[17] The microfabricated devices were later used together with pulsed field electrophoresis for separating DNA larger than 100 kbp. High electric field can be applied in these devices without concerns of Joule heating or damage to the separation media. Bakajin et al achieved separation of T4 DNA (166 kbp) and  $\lambda$ DNA (48 kbp) in 10 second using a 1 cm long post array, with pulsed fields running at 120° and 224 V, while the same separation can take 10 h with PFGE in gels, due to the low electric fields applied.[18]

The mechanism of large DNA separation by pulsed field electrophoresis in microfabricated devices is the same as in gels. DNA molecules can be separated by sizes in pulsed field electrophoresis, because large DNA molecules spends a longer time in reorientation as the field directions alternate, and thus has lower net mobility compared to smaller DNA. Through tracking the motion of dyed DNA molecules in microfabricated devices with a microscope, it was observed that DNA molecules remain in a stretched conformation (elongated but not fully stretched) during pulsed field electrophoresis in micrographically fabricated arrays (Figure 1A). Motion of DNA molecules under pulsed fields at an obtuse angle follows a “ratchet” model,[16, 19] with the leading and trailing ends of DNA switching roles with pulsed fields in alternating directions (Figure 1A). Once the electric field is switched, the DNA molecules first reorient to align the entire molecule parallel with the electric field. During the reorientation, the net distance that DNA travels along the separation lane is zero, because the molecule backtracks along the path it just travelled. As DNA is stretched, the reorientation time  $t_{or}$  is linearly proportional to the number of DNA base pairs  $N$ , hence the larger DNA molecules have lower effective mobility.

The conventional pulsed fields used in DNA electrophoresis, in either gels or microfabricated devices, are symmetric in field strength. Therefore, DNA molecules, independent of the size, move along the symmetrical line of pulsed fields, forming separation bands on one lane. In 2002, Huang et al designed a “DNA prism” chip (Figure 1B) utilizing asymmetric pulsed fields, and DNA from 60 to 200 kbp were fractionated in 15 s using 3 mm x 9 mm post arrays.[13] Motion of a DNA molecule still follows the ratchet model, but molecules of different sizes are deflected into different angles instead of forming parallel bands. The mechanism of asymmetric pulsed field electrophoresis (APFE) is illustrated in Figure 1B. While DNA molecules migrate downstream, led by the high field, they are deflected horizontally by the low field and the deflection distances are determined by the DNA size. Large DNA, that cannot finish reorientation before the lower field is switched, continue migrating downstream from the original pathway in the lattice, while smaller DNA are relocated along the lattice pathways by the low field and then migrate along different lattice pathways. This process allows DNA sizes to be sorted into different deflection bands. Using APFE, microfluidic devices allow the continuous-flow operation of DNA fractionation, therefore offering higher throughput compared to Bakajin’s device.

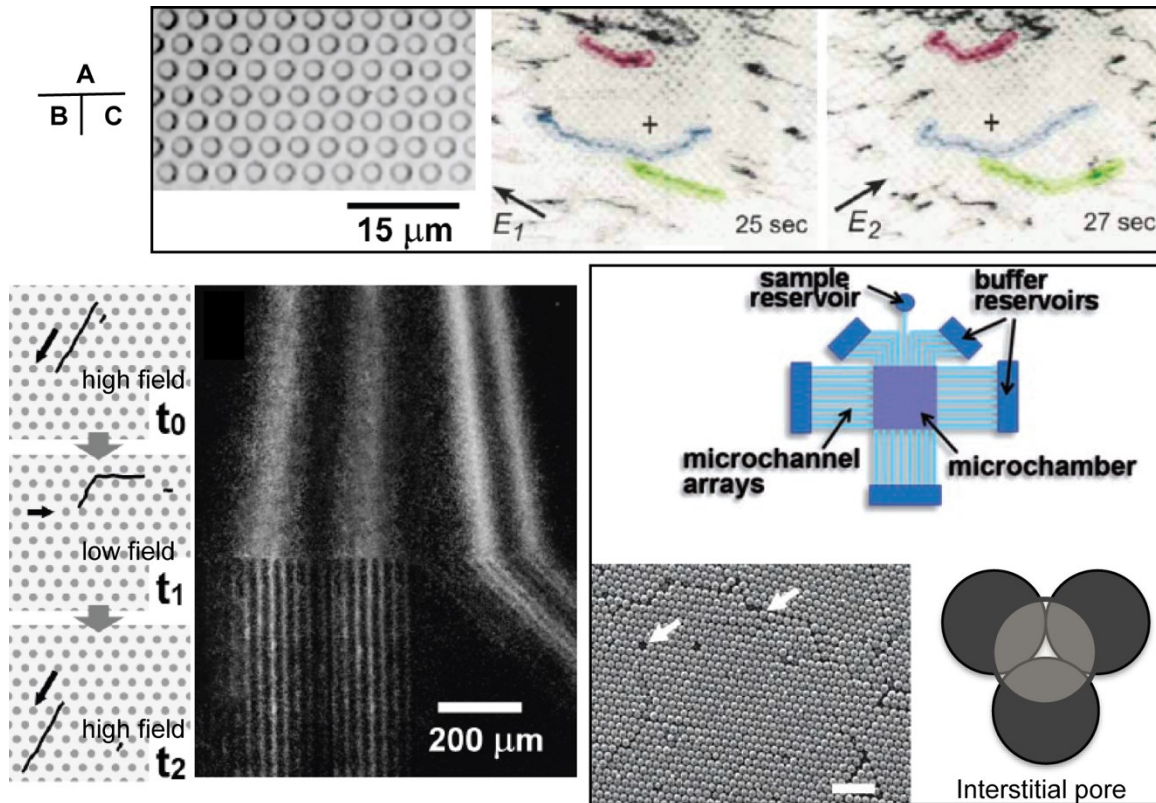


Figure 1-1: A) SEM image of post arrays and fluorescent images of labeled DNA molecules undergoing pulsed field electrophoresis in microfabricated arrays. The DNA is reoriented as the electric field is switched. B) Sketches of the mechanism of DNA separation through APFE and a fluorescence image showing deflection bands. C) Design of the microfluidic device developed by Zeng et al, SEM image of silica crystalline arrays and sketch of 3D nanopore generated by crystalline arrays. Reprinted with permissions from A) ref [19] © 1996 VCH Verlagsgesellschaft mbH, B) ref [13] © 2002 Nature Publishing Group and C) ref [20] © 2008 WILEY-VCH Verlag GmbH & Co. KGaA.

Although separation efficiencies are significantly improved with post arrays, fabricating these arrays is more expensive and complicated than preparing gels. In 2008, Zeng et al developed a low-cost and disposable microfluidic device for DNA electrophoresis and demonstrated separation of 2-20 kbp DNA through APFE.[20] The separation bed, as shown in Figure 1C, is made of large-scale crystalline nanoarrays generated by colloidal self-assembly (CSA) of silica particles. DNA molecules migrate through the interstitial

pores of crystalline sieves during electrophoresis. Compared to post arrays, this nanoporous structure is more like an “artificial gel”. The pore size of crystalline sieves (e.g. 105 nm) is substantially uniform and close to that in 1% agarose gel (100-500 nm), while the microposts are generally 2  $\mu\text{m}$  in diameters and 2  $\mu\text{m}$  apart. DNA of 20-166 kbp were separated with good resolutions in this nanoporous structure. In chapter 2, we will further discuss the capability of this device in rapid separation of larger DNA molecules.

Microfabricated devices for DNA electrophoresis are not limited to the examples discussed above.[21] The materials used for constructing post arrays were various, ranging from silica,[22] to PDMS,[23] to self-assembled magnetic particles[24, 25] with tunable post spacing between submicrometer to 100  $\mu\text{m}$ . Nanofluidic entropic trapping devices developed by Han et al[26] are another category of DNA separation device, which also efficiently separate 5-166 kbp DNA molecules by electrophoresis.

### **1.2.3 DNA trapping during electrophoresis and complexities beyond the ratchet model**

#### **1.2.3.1 Large DNA trapping during electrophoresis**

Microfabricated devices offer rapid DNA separation, but their potential to replace PFGE is not guaranteed. The separation of large DNA molecules (>209 kbp) using these devices has never been reported, except in the work of a former PhD student in our lab, Huiying Sheng. Sheng detailed the results and problems of using crystalline nanoporous structures for megabase DNA separation in her thesis.[27] She determined that trapping of

megabase-sized DNA is very common in CSA-based nanoporous structures, but that separation of DNA from 200 kbp to 1 Mbp can be achieved by using intermittent pulsed fields as it is in conventional gels.[28] Using a total internal reflection fluorescence (TIRF) microscope to track single DNA molecules, she found a few T4 DNA (166 kbp) began to be trapped when the field strength was over 100 V/cm, which is still a much higher field and thus faster separation time than seen in gels for large DNA.

From a broad perspective, DNA trapping is an unsolved problem in PFGE as well as in CSA-based structures and trapping seriously limits separation efficiency. Although PFGE has been successfully applied to separate DNA up to 10 Mbp, the performance above 1 Mbp showed the resolution is very poor, even with a field strength reduced to  $< 2$  V/cm.[29] Using normal field strengths at 6-8 V/cm, separation bands tend to smear at lower molecular weights (Figure 2a), due to partial trapping of DNA.[28, 30] In addition, it is very difficult to force a megabase DNA plug to enter a gel. There are some experimental observations related to this trapping phenomenon: 1) For a certain size DNA, trapping occurs when the field strength is over a critical value.[15] Therefore, trapping restricts the field strength applied in PFGE to a greater extent than Joule heating does for shorter DNA; 2) trapping is irreversible,[14] so that trapped DNA molecules are not released after field strengths are decreased; 3) applying intermittent fields can effectively reduce trapping.[28]

Several mechanisms of DNA trapping in gel electrophoresis were proposed, as illustrated in Figure 2b-2d. The first suggestions came from the inhomogeneous distribution of pore sizes in gel, that DNA was trapped in dense regions with dead end passage ways.[28]

Other mechanisms were proposed based on the fact that the simple “tube” model for DNA conformation in a confined structure is frequently violated during gel electrophoresis. Complex DNA conformations will be discussed in the next section, but simple concepts are given here. DNA molecules were observed to not always take an elongated tube-like conformation, particularly at high field strength.[31] As the electric field was switched, segments of DNAs were folded and squeezed into the same pores, forming “hernias”[32, 33] (Figure 2b), which was considered to result in trapping by an unknown process.[28] In another case, DNA collides with, and hooks around gel fibers (Figure 2d), forming U/J shapes.[34, 35] It is obvious that U-shaped DNA, which has two equal chains would be effectively trapped in DC electrophoresis. However, only a very few hooked DNA precisely end up with a U-shape, insufficient to cause visible trapping.[36] Burlatsky et al proposed that there was a solid friction between J-shape DNA and gel fiber at the pivot, so that some J-shaped DNA could not be unhooked by electric force, thus being trapped.[37] Viovy et al pointed out that all these conformational mechanisms could not explain the irreversibility of DNA trapping observed in PFGE.[38] According to polymer physics theories, after the electric field is turned off or switched, DNA relaxes and releases molecular tensions, which should result in detrapping.[39] A “tight knot” model was proposed by Viovy et al,[14] where the trapped DNA were first arrested by any type of topological trapping discussed above, then driven over a higher conformational energy barrier, for instance, forming a crossover knot (Figure 2c). Experimental evidence and the dynamics of DNA molecules passing through this conformational energy barrier under pulsed fields were not given in this model.

The trapping process in Viovy's model is very abstract. There are many questions to ask: What is that topological trap which initially arrests DNA, U/J shape or hernia? And what is that energy barrier which causes the formation of an irreversible conformation like a "crossover knot"? Several answers to these questions within CSA-based sieve structures are given in Chapter 2, along with the evidence to support our conclusions.

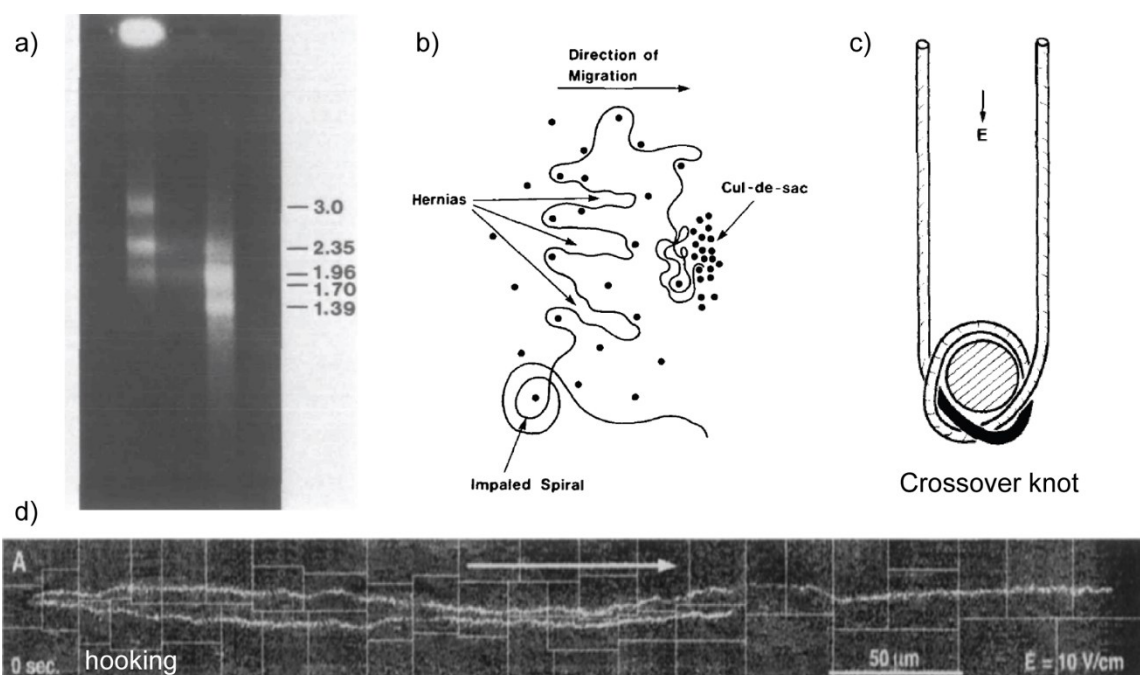


Figure 1-2: a) Separation of yeast chromosomes in gel electrophoresis. The DNA were first separated by pulsed fields in the left lane and then driven to the right lane by DC field. Trapping and band smearing are obvious. The numbers indicate DNA sizes in megabase pair unit. b-d) DNA trapping mechanisms proposed in several papers. Reprinted with permission from a-b) ref [28] © 1990 Oxford University Press, c) ref [14] © 1992 VCH Verlagsgesellschaft mbH and d) ref [15] © 1999 The National Academy of Sciences.

### 1.2.3.2 The conformations of confined DNA: stretching, U/J shape and hernias

The reproducible and well characterized topology of micro- and nanostructures facilitates quantitative description of DNA electrophoresis. The dynamics of DNA electrophoresis in

microarrays and crystalline nanoparticle structures were studied by Duke et al[19] and Nazemifard et al,[40] respectively. In these theoretical studies, the mathematical expressions of key parameters in pulsed field electrophoresis, such as DNA reorientation time  $t_{or}$  and relaxation time  $t_R$ , were given, and the optimal field strengths and frequencies for DNA separation were calculated, some of which are very consistent with experimental results, particularly for small DNA ( $< 48$  kbp). However, these theoretical studies fail to predict trapping, because they are based on the “DNA forms a tube” model and leave out cases in which the ratchet motion is confounded by complex DNA conformations.

DNA conformation in confined structures is an important subject in polymer physics, and the fundamental theory was established by de Gennes in the 1970s.[41, 42] Assuming that DNA is effectively confined in a “tube-like” region, de Gennes’ theory explains most of experimental results in DNA gel electrophoresis.[43] Evidence for the leakage of tubes and the formation of U/J shapes and hernias was obtained using the fluorescent microscope and occurred in the late 1980s.[34] Taking account of the presence of these complex conformations, a quantitative description of DNA motion in non-uniform gel media becomes more difficult. Since micro- and nanostructures allow study of DNA conformations in given confined dimensions, they are widely applied in such studies,[44, 45] though the results were not directly linked to two-dimensional DNA separation in pulsed fields. Here, we detailed some results that are used in Chapter 2.

Reisner et al utilized nanochannels to study the transition of stretched DNA from the de Gennes regime to the Odijk regime.[46] Both regimes describe stretched “tube-like” DNA

in confined structure, as shown in Figure 3a. In the de Gennes regime,[47] the molecule chain is partially coiled and the elongation is due to excluded volume interactions between molecular segments. In contrast, the Odijk regime[48] works at the strong confinement limit where the molecule is more stretched, and backfolding is restricted by the interplay between the channel walls and DNA's intrinsic elasticity. From the perspective of interactions, the two regimes predict different scaling relations of the hydrodynamic friction coefficient of DNA with pore size (or channel width). Reisner found the critical channel width for the transition is about twice the DNA persistence length  $P$  ( $P = 53$  nm). Therefore, according to their results, DNA separated in photolithographically fabricated microarrays are moderately elongated as described in de Gennes' model, while in gels and crystalline nanoparticle arrays, DNA are more stretched as described in Odijk's model. In Chapter 2, 690 nm silica particles were selected to construct a 105 nm pore size, and DNA extension length and hydrodynamic friction coefficients predicted from Odijk's model were employed in calculations.

Randall and Doyle studied formation and unhooking dynamics of U/J shaped DNA molecules using PDMS microfluidic device.[49] DNA collides with, and hooks around PDMS posts during electrophoresis, giving rise to U/J shaped conformations (Figure 3b). The authors proposed unhooking time of U/J shaped DNA are based on rope-on-pulley dynamics:

$$t_{unhooking} = -\frac{L}{2\mu E} \ln\left(1 - \frac{2x_1}{L}\right) \quad (\text{Equation 1-1})$$

where  $L$  is DNA contour length,  $\mu$  is mobility,  $E$  is field strength and  $x_1$  is the length of short arm of U-shape. Rope-on-pulley is a simplified model, and it was later modified for more complex situations. Randall et al[50] and Holleran et al[51] proposed modified unhooking time models, respectively, taking account of diffusive fluctuations and DNA relaxation at the weak field regime. In Chapter 2, we identify that another force is present at the apex of U/J-shaped DNA, resulting in infinite unhooking time, which cannot be predicted by Equation 1.1.

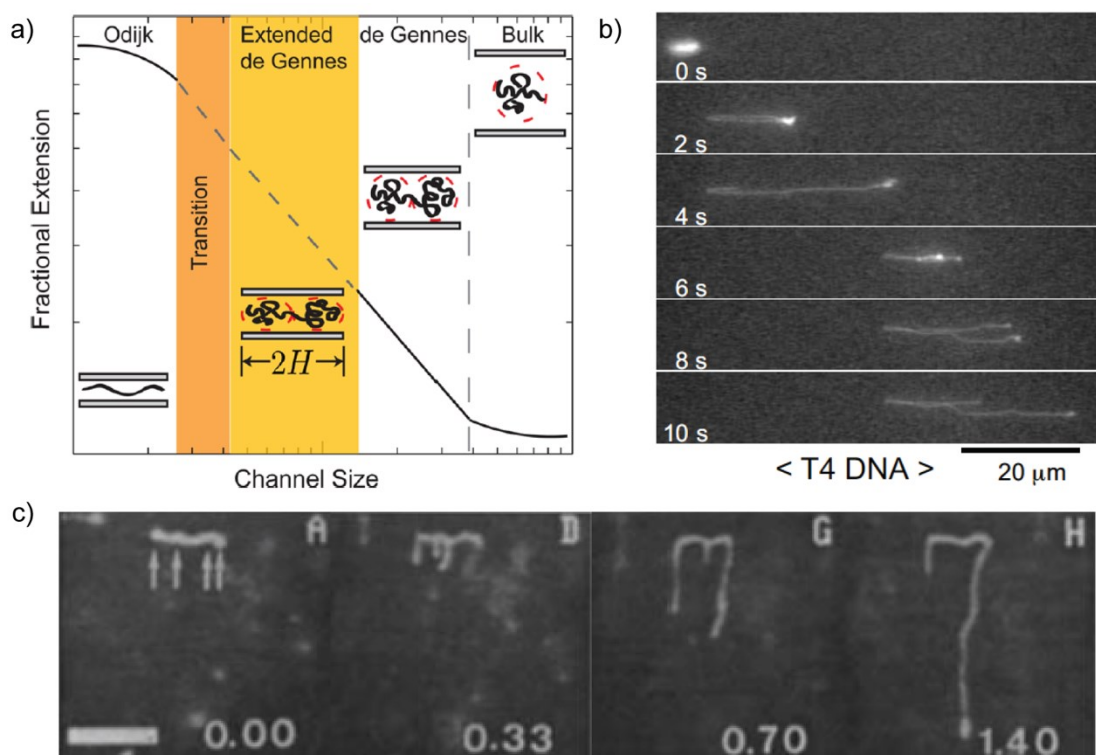


Figure 1-3: a) Conformations of stretched DNA in strong confinement, weak confinement and bulk solution. b) Time-lapse images showing the process of single DNA molecule colliding with obstacle, forming U/J shape and unhooking. c) Time-lapse images showing formation and evolution of hernias after electric field was switched. Reprinted with permission from a) ref [52] © 2011 American Chemical Society, b) ref [22] © 2004 American Chemical Society and c) ref [53] © 1990 American Chemical Society.

Hernias are frequently observed in DNA electrophoresis, in both gels and nano-structured devices, as shown in Figure 3c. The formation and evolution of hernias were theoretically described by Deutsch[54] and Akerman et al.[55] As the electric field is switched, hernias are pulled out from the tube conformation by electric force, overcoming entropic barriers, thus they are predicted to occur only at high field strength. Studies by Viovy[56] and Slater and Noolandi[16] show that the formation of hernias only affect the quantitative prediction of DNA reorientation time in pulsed field electrophoresis, while the ratchet model is still dominant. However, our results show hernias have the ability to confound the ratchet model and ultimately lead to DNA trapping.

### **1.2.3.3 Dielectrophoresis (DEP) trapping of biomolecules in nanostructure**

DNA trapping is a broader concept than the electrophoretic trapping discussed above. In most cases, it is not a problematic phenomenon, but instead applied in single molecule manipulation: DNA sequencing[57, 58] and other biomolecular analysis, such as the DNA entropic trapping method mentioned in Section 1.2.2; dielectrophoresis (DEP) trapping;[59, 60] anti-Brownian electrokinetic trapping[61, 62] and solid-state nanopore trapping.[63] All these techniques require precise control of electric field in nanoscale devices. Importantly for this thesis, we noticed that in a nano-post structure insulator-based DEP (iDEP) trapping of DNA molecules[64] was demonstrated for kb DNA, though at higher field strengths and frequencies than were applied for DNA in this work. Therefore, we concluded there is a possibility that DNA electrophoresis is generally accompanied by DEP phenomenon.

A dielectric particle is subject to DEP force when it is under a non-uniform electric field.[65, 66] Not only restricted to the manipulation of particles, DEP trapping has also been applied in patterning of DNA origami,[66] proteins[67, 68] and cells[69, 70] which have dipole moments induced under electric field. As shown in Figure 4b, DNA is polarizable in buffer solution, due to its negatively charged backbone and positive counterions in the double layer.

In many microchip devices the non-uniform fields needed for DEP trapping are directly controlled by embedded microelectrodes. In 2003, Cummings and Singh first introduced iDEP trapping,[71] where a field gradient was generated by insulating posts in microchannels (Figure 3c), instead of by embedded electrodes. It was also demonstrated that iDEP trapping of single cells can be achieved with DC fields applied to the ends of microfluidic channels.[72] The iDEP trapping of DNA was also reported, but AC fields with high frequencies ( $> 60$  Hz) were required.[64, 73, 74] The iDEP force on DNA at DC fields and low-frequency AC field was found negligible, and for this reason it was not anticipated to contribute to microarray-based DNA separation.

It is apparent that DNA separation media (gel, microarrays, crystalline nanopore) are inhomogeneous in regard to the distribution of the electric field. In studies of collision between DNA and PDMS posts, the deformation of electric field around the posts were mentioned by Randall et al,[23] but further considerations or observations were not given. In Chapter 2, we calculate the electric field gradient generated in nanoporous structures and

demonstrate it is the presence of tiny iDEP forces under DC field that confound the ratchet motion of DNA and cause trapping.

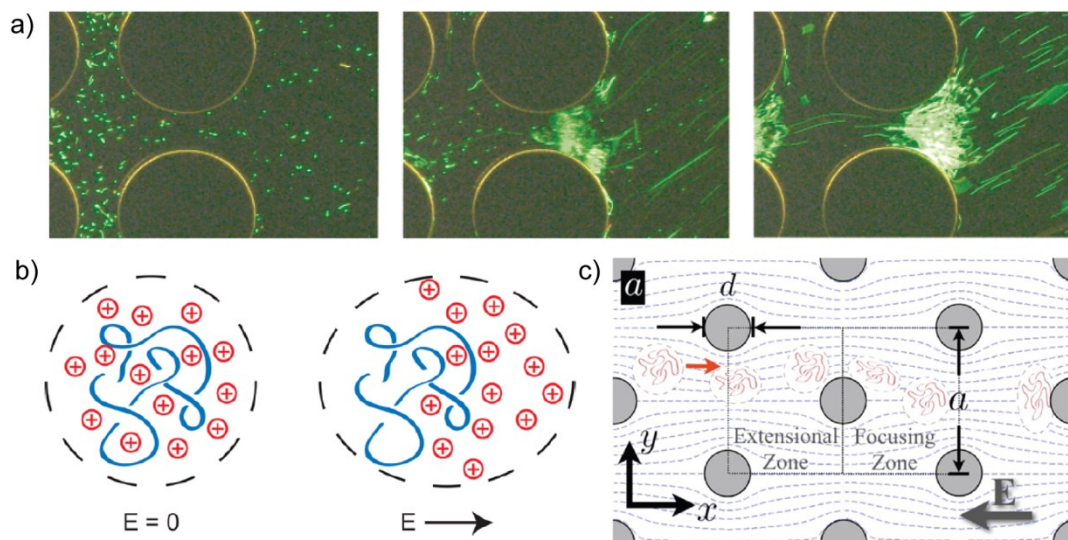


Figure 1-4: a) The DEP trapping of DNA in PDMS microarrays. b) The dipole moment of DNA molecule induced by electric field. c) The deformation of electric field in PDMS microarrays. Reprinted with permission from a) ref [75] © 2004 American Chemical Society, b) ref [76] © 2013 American Chemical Society and c) ref [77] © 2009 The American Physical Society.

### 1.3 Laser desorption/ionization mass spectrometry (LDI-MS) on nanoporous silicon and its application on metabolite analysis

#### 1.3.1 Introduction

Laser desorption ionization (LDI) is a soft ionization technique used in mass spectrometry (MS) that has been widely applied to rapid identification of biomolecules and synthetic macromolecules.[78] Laser-induced desorption ionization technique was developed in the 1960's when laser irradiation was found to be an excellent source for fast surface heating,

and the breakthroughs were made in the late 1980s. The successful implementation of LDI, as demonstrated by Tanaka et al in 1988,[79] has to be assisted by use of a suitable matrix or surface for efficient adsorption of UV radiation (337 nm laser pulses). Samples must be mixed with an organic matrix (e.g.,  $\alpha$ -cyano-4-hydroxycinnamic acid and 2,5-dihydroxybenzoic acid) before being deposited on a metal plate,[80] or deposited alone on a special surface,[81] to effect LDI. The former is the original and most common form of LDI, matrix-assisted LDI (MALDI), while the latter is regarded as a variant and categorized as surface-assisted LDI (SALDI), though different names are usually given to individual surfaces. SALDI is an important application of nanomaterials, as surfaces developed so far are those of either nanoparticles or nanostructured thin films.[82, 83] In this section, the development of SALDI surfaces that do not involve the addition of a MALDI-style matrix is reviewed, as well as the applications. SALDI offers notable performance for small molecule (MW < 1000 Da) detection, thus has been applied in metabolite profiling and imaging.[84, 85] Herein, the advantages and challenges of using SALDI surfaces to analyze metabolites in biological samples is discussed.

### **1.3.2 Desorption/ionization on nanostructured surface for small molecule detection**

The concept of SALDI was first proposed in Sunner and Chen's paper published in 1995 where the authors used graphite nanoparticles (2-150 nm) to assist the LDI of peptide and proteins from liquid solutions.[86] In fact, Tanaka et al mixed protein samples with ultrafine cobalt powders in glycerol solution when the analysis of proteins by LDI-MS was first demonstrated in 1988. However, the advantage of solid surfaces over organic matrices

was not specified then, and MALDI was later developed as a more conventional approach for proteomic studies and other mass spectrometry applications.

SALDI became a successful complement to MALDI, after the desorption/ionization on silicon (DIOS) for small molecule detection was reported by Wei and Siuzdak in 1999.[87] The ionization of the organic matrix in MALDI causes chemical background noise in the low mass range, thus suppressing signals of small analytes.[88] In DIOS, porous silicon fabricated from electrochemical etching serves as the surface for effecting LDI (Figure 5a and 5b). Since the use of an organic matrix is avoided, chemical interference at the low mass range is greatly reduced, and consequently lower limits of detection (LOD) can be obtained. When applied to detect laboratory prepared drugs and trypsin digested peptides, DIOS is able to work at femtomole and attomole levels, respectively, with a time-of-flight (TOF) mass analyzer.[89, 90]

The mechanism of DIOS has been explored by several groups, but a definitive model is not yet available. The results suggest that the nanoporous structure (pore size of 10-100 nm) is essential for DIOS in aspects of trapping analytes, solvent and for adsorbing UV radiation.[87, 91] Surface roughness is considered to enhance UV adsorption and thermal conductivity of silicon,[92-94] but an optimal surface morphology related to both porosity and layer depth has not been predicted. Alimpiev et al investigated the function of nanostructured silicon in the ionization process and proposed in 2001 that analytes were solvated on nanoporous surfaces due to physisorbed water and then ionized under laser

pulses,[95] but the authors then proposed other possible mechanisms in the following years.[96, 97]

In spite of the unclear desorption ionization process, new SALDI surfaces were developed after DIOS and applied to small molecule analysis, such as silica nanoparticles,[98, 99] nanostructured indium tin oxide slides,[100] cobalt nanorods,[101] porous alumina[102, 103] and carbon nanotubes[104-106]. The LODs obtained on these SALDI surfaces are not as distinguished as on DIOS, but on the other hand it is unfair to have them directly compared, since none of these surfaces, including DIOS, is capable of comprehensive study of the vast range of small molecules.[107] Often, analytes that are undetectable by DIOS can be observed on mass spectra using other surfaces. Among all the suitable nanomaterials mentioned above, porous silicon (pSi) is the most popular SALDI surface in both research and commercial applications.[82] Usually, the pSi-LDI surfaces are subdivided according to their fabrication methods. Apart from electrochemical etching used for preparing DIOS chips,[108] other methods involved in fabricating pSi-LDI surfaces are metal assisted chemical etching,[109, 110] vapor-liquid-solid growth,[111, 112] e-beam lithography,[113] reactive-ion etching,[113, 114] etc. Compared to electrochemical etching, these fabrication methods tend to produce more ordered nanostructures, therefore they are often used for investigating the correlations between surface morphology and LDI efficiency.[112, 115] In addition, it was found the performance of DIOS can be degraded due to trapped etchant[116], while the other fabrication methods are cleaner, relatively, and offer a more stable pSi-LDI surface with a longer shelf time.

The pSi-LDI surface used in this thesis are nanocolumnar silicon thin films fabricated by glancing angle deposition (GLAD). GLAD is a thin film deposition technique invented by Robbie and Brett,[117, 118] and Jemere et al have demonstrated that silicon GLAD films are suitable for LDI-MS in 2010.[119] Figure 5c illustrates that nanocolumns form during GLAD deposition as a result of shadowing effect. The incident vapor flux is generated through electron-beam evaporation and then deposited at an oblique angle. The initial atoms that arrive at the substrate are adsorbed on the surface, forming random nucleation points. As these random nuclei grow into columns, the substrate is shadowed from the incoming flux. By rotating the substrate during the deposition, nanocolumns grow normal to the substrate, as shown in Figure 5d. With this fabrication process, performance of GLAD based LDI chips do not obviously degrade after several-month storage in ambient condition. In addition, as a versatile fabrication technique, GLAD is able to fabricate more sophisticated nanoscale architectures, with diverse evaporation materials.[120, 121] A former group member, Reshma Singh, along with Louis Bezuidenhout[122] concluded that higher ionization efficiencies can be obtained on cobalt GLAD films and slanted silicon nanocolumns. Singh also integrated ultra-thin layer chromatography on an LDI surface using silica GLAD film, to achieve serum metabolite separation and detection on a single platform.

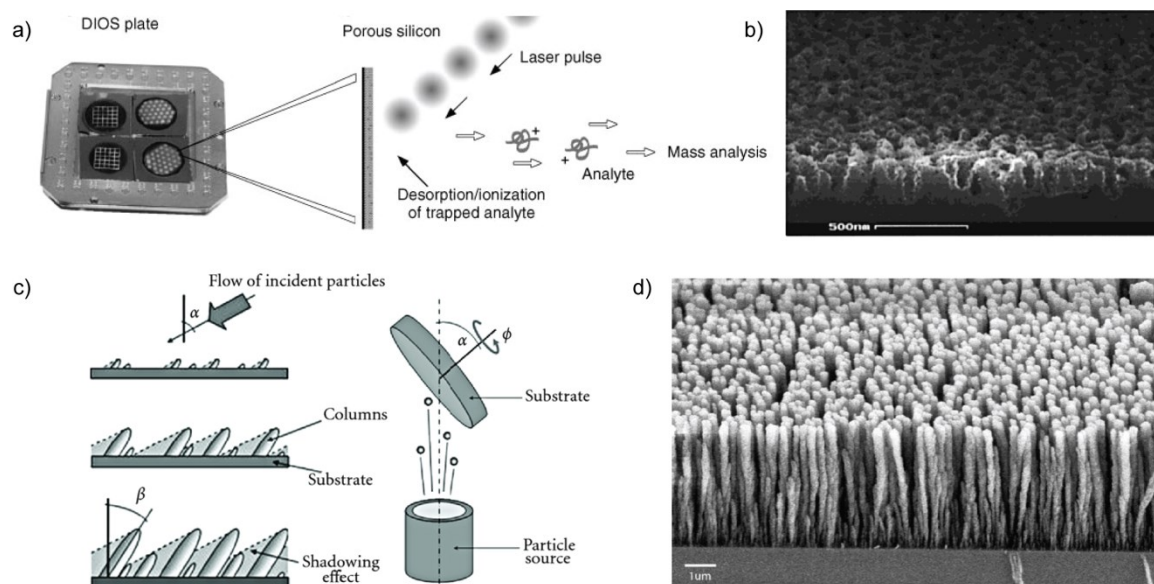


Figure 1-5 : a) Sketch of DIOS-MS. b) SEM image of DIOS chip fabricated by electrochemical etching of silicon wafer. c) Sketch of GLAD process. d) SEM image of vertical silicon nanocolumns fabricated through GLAD. Reprinted with permission from a) ref [87] © 1999 Nature Publishing Group, b) ref [90] © 2001 American Chemical Society, c) ref [123] © 2012 Zdenek Michalcik et al and d) ref [117] © 1997 American Vacuum Society.

### 1.3.3 Improved LDI performance on silylated porous silicon

pSi is the most popular SALDI surface, not only because of excellent ionization efficiency and a mature fabrication process, but also due to the well-developed surface chemistry of pSi. Functionalized pSi is commonly prepared through silanization of an oxidized pSi surface[124, 125] or via hydrosilylation,[126-128] and has been widely employed in immunocapture,[129, 130] DNA sensing[131, 132] and *in vivo* applications.[133, 134]

In the application of LDI, pSi surfaces are mostly modified by silanization, and a comprehensive study of improved LDI performance using silylated pSi was first reported

by Trauger and Siuzdak.[125] Their results suggest that surface modification does not undermine, instead it greatly improves, LDI performance of DIOS. Most notably, the limit of detection (LOD) for des-Arg<sup>9</sup>-bradykinin was improved from attomole to 480 molecules (800 yoctomole) on a pentafluorophenyl-functionalized DIOS chip, making DIOS one of ultra-sensitive MS techniques.

Among all organosilanes tested by Trauger, the perfluoro silanes are the best choices for enhancing ionization efficiency of pSi-LDI, with highest sensitivity and minimal background. There are many possible reasons for this observation.[125, 135, 136] First, the perfluoro coating turns the pSi surface from hydrophilic to hydrophobic, providing some pre-concentration of aqueous samples. Secondly, the perfluoro coating stabilizes the pSi surface by reducing adsorption of contaminants in the air and making it resistant to oxidization/hydrolysis under ambient conditions. Thirdly, the strong C-F bond makes perfluoro coatings less easily ablated by laser pulses than hydrocarbon coatings, reducing ionization interference by the coating. It was also proposed that the perfluoro coating does not adsorb laser irradiation, thus not reducing the energy transfer efficiency of pSi-LDI, although other coatings may also make this claim. The perfluoro siloxanes are also found to be the best initiators for nanostructure-initiator mass spectrometry (NIMS) which has gained success in tissue MS imaging.[108, 137, 138] NIMS is a DIOS-derived MS technique in which liquid siloxane (initiator) was added to electrochemically etched pSi and trapped as a vaporizable liquid within the nanostructure.

A former group member, Chen Peng developed the silanization of silicon GLAD films (Figure 6a) for LDI work.[139] In Peng's method, GLAD films were soaked in 1% reactive silane solution in methanol for 30 min. The results showed that longer reaction times and higher silane concentrations result in cloudy polymerization layers on the GLAD film, with damage and delamination of the nanostructure. At optimal concentrations and reactions times it was found that freshly prepared films should be stored in ambient condition overnight to complete the reaction, followed by critical point drying (CPD) to remove trapped methanol and excess silanes. After CPD, surfaces of GLAD films appear smooth and clean. Characterization by optical and SEM imaging show surfaces were uniformly modified, however, clumping of nanocolumns was observed under some conditions. Peng's MS results show perfluoro coatings greatly suppress chemical background in the low mass range (50-400 Da, Figure 6b and 6c) for LDI on Si-GLAD films, more effectively than UV/ozone treatment on these films. Peng also demonstrated the perfluoro coating improves quantitative analysis of pure samples using pSi-LDI-MS, which will be detailed in Chapter 3.

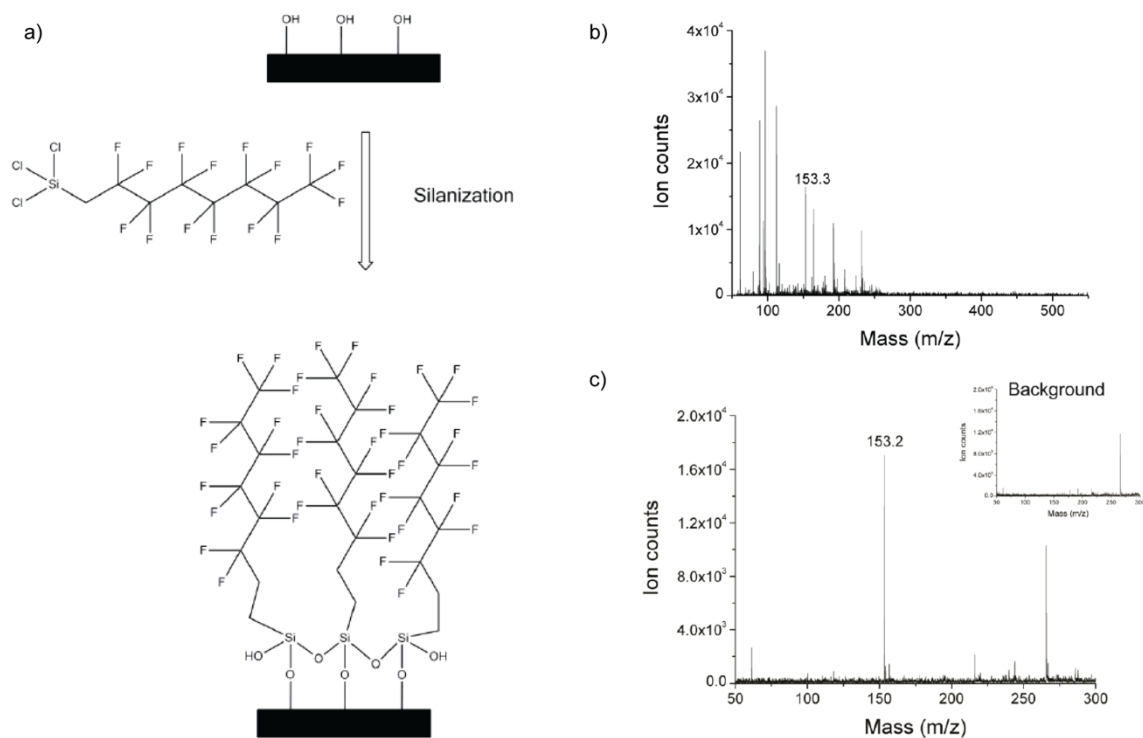


Figure 1-6: a) (1H, 1H, 2H, 2H-perfluorooctyl)trichloro silane (pFSiCl<sub>3</sub>) silanization on Si GLAD film surfaces. b and c) Mass spectra of 200 pmol histidine obtained on b) uncoated and c) pFSiCl<sub>3</sub> modified Si GLAD films, in negative ion mode. Reprinted with permission from ref [139] © 2014 Chen Peng.

Apart from improving LDI performance, functionalized pSi surfaces were also used for sample preparation before LDI-MS measurements, through surface-enhanced selectivity.[140-142] These efforts will be discussed in the next section, as background for using pSi-LDI in metabolite analysis of biological samples.

### 1.3.4 Metabolite analysis by pSi-LDI and challenges in sample preparation

The Metabolome, as an extension of the concept of the Genome, represents a complete set of small molecules involved in cellular processes, and it is considered to more directly

reveal the phenotype from the biochemical perspective.[143-145] Williams et al first proposed in late 1940 that individuals had a distinct metabolite pattern in their biofluids and demonstrated metabolite patterns were associated with diseases using paper chromatography.[146, 147] The advance of analytical techniques later allowed quantitative analysis of metabolites, and the pioneering work of metabolite profiling by gas chromatography–mass spectrometry (GC-MS) was reported by Horning et al in 1971.[148] Since then, metabolite profiling has been increasingly employed in biomarker discovery.[149, 150]

Nuclear magnetic resonance (NMR) and MS are two major analytical tools used in metabolite analysis. Compared to MS, NMR requires minimal sample preparation, but is limited by relatively poor sensitivity (LODs > 10  $\mu$ M).[151] MS offers potential for more universal metabolite profiling due to its high sensitivity in detection.[152] Many associated techniques relative to sample preparation,[153, 154] quantitation,[155] data processing and interpretation[156] have been developed exclusively for application of MS in Metabolomics in recent years, however, benchmarks are not settled in all respects.[157, 158] Since Chapter 3 is about desalting biofluids on pSi-LDI chips, the following discussion will focus on sample preparation for MS analysis of metabolites.

Liquid chromatography – mass spectrometry (LC-MS) is currently the most powerful method in MS-based metabolite profiling.[159, 160] In sample preparation, matrix components, particularly proteins and salts, must be removed ahead of MS measurements. Usually, proteins are removed through methanol precipitation or ultrafiltration, and the

latter is found more efficient in removing small proteins (3-10 kDa).[161] After deproteinization, metabolites are usually separated from salts with reverse phase LC (RPLC) which is conventionally coupled with electrospray ionization (ESI) or nano-ESI for online sample preparation.[162, 163] Highly polar metabolites, such as amino acids, have poor retention on RPLC. These compounds are derivatized before processing by RPLC,[164] or desalted by hydrophilic interaction chromatography,[165, 166] or by capillary electrophoresis.[167] Generally, each separation method introduces bias towards a specific set of metabolites, and the extraction and derivatization steps inevitably lead to loss of metabolites.[165]

As discussed above, pSi-LDI offers notably high sensitivity in small molecule detection, besides which, pSi-LDI produces fewer multiple charged ions compared to ESI.[168] Therefore, it is hoped pSi-LDI may provide direct analysis of small molecules in biofluids (blood, urine, etc.) as a simple spot test. The main challenge of analysing complex samples with pSi-LDI is that deposits of background electrolytes conceal the nanoporous structure, severely impairing desorption ionization activity.[108, 125] Proper sample cleanup is still required in pSi-LDI.

Sample dilution (e.g., biofluid/solvent, 1:100, v/v) was reported useful to quantify some metabolites, such as glucose and sterols, which are rich in biofluids and have larger molecular weights.[85, 169] LDI surfaces are known to be somewhat salt tolerant, compared to ESI, and more sensitive at high mass range (400-3000 Da).[170, 171] It was pointed out by Law et al that further dilutions suppress analyte desorption ionization.[169]

Trauger et al evaluated metabolite desalting by ZipTips which is a miniaturized solid phase extraction for protein desalting in MALDI-MS.[125] Significant losses of metabolites were observed, possibly due to a combination of irreversible adsorption onto the stationary phase for some metabolites, and a lack of retention for others.

Simple sample preparation for small metabolite analysis is available on functionalized pSi surfaces. “Direct” analysis of metabolites in biological samples was achieved by relying on differential adsorption on perfluoro coated pSi surface. Biofluid samples were spotted on perfluoro coated pSi for 30 s and then blown off the surface with nitrogen stream.[137] The sample stain that remained on the solid matrix was detected. Another method, termed “Z-touch”, is also frequently used, in which a sample droplet is pipetted up and down for 5-10 times before being pipetted off the surface.[108, 138] These methods are suitable for less polar analytes that can be bound to silylated pSi surface through hydrophobic interactions. Yanes et al demonstrated quantitative analysis of codeine, alprazolam and morphine spiked in human serum using the Z-touch method.[142]

Desalting for analysis of highly polar metabolites on a pSi surface is complicated. Go et al achieved selective capture of amino acids from human serum utilizing a fluororous affinity tag on the amino acids.[141] When rinsed with water/methanol (50/50) solvent, the labelled amino acids were retained on the perfluoro coated pSi surface due to strong fluorine-fluorine interaction. Mass spectra of amino acids in human serum were obtained, but the analytes were not quantified, possibly because the fluororous esterification is not specific to amino acids and interferences arise from other carboxylic metabolites present in both the derivatization

and detection processes. Lowe and Voelcker reported the selective capture and detection of illicit drugs by combining immunocapture and LDI on a pSi surface, but the sensitivity of pSi-LDI was reduced due to interference from the immobilized antibody.[140] In Chapter 3, a novel on-chip desalting approach for pSi-LDI will be introduced and its feasibility in quantitative analysis of amino acids is demonstrated, as well. In Chapter 4, the pSi surface developed in Chapter 3 is applied to serum metabolite analysis.

## **1.4 Thesis outline**

In Chapter 2, we investigate the trapping mechanism of individual DNA molecules in ordered nanoporous structures generated by crystalline particle arrays. The dynamics of single DNA between the free and trapped states was captured using TIRF microscope. It was observed the trapping starts from hooking, followed by formation of hernias which then form heads that lead the reorientation under a change of electric field direction, confounding the ratchet model. The process is related to DNA molecules that cannot unhook in a timely way from U/J shapes. Fully stretched DNA has longer unhooking times than expected by a classic rope-on-pulley model. We propose a DEP force reduces the mobility of segments at the apex of the U or J, where field gradients are highest, based on simulations and observations of the trapping force dependence on field strength. A modified model for unhooking time is obtained after the DEP force is introduced. The DNA polarizability calculated with the modified model and experimental values of unhooking time is of the same magnitude of reported value, supporting the DEP assumption.

In Chapter 3, we present a solid matrix assisted laser desorption ionization (SMALDI) technique, coupled with fluorocarbon coating, to achieve selective segregation of analyte from background biofluid electrolytes for quantitative mass spectrometric analysis. By controlling the defect density, evaluated through the contact angle, of (1H, 1H, 2H, 2H-perfluorooctyl) trichlorosilane or (1H, 1H, 2H, 2H-perfluorooctyl) dimethylchlorosilane, background electrolytes can be made to segregate from the analyte during a slow drying step on the surface of a highly nanoporous thin film. Silicon films were prepared using glancing angle deposition (GLAD) thin film technology, then coated with fluorocarbon. This desalting method directly separates amino acids from salty biofluids, as demonstrated for artificial cerebral spinal fluid (aCSF). Derivatization, extraction and rinsing steps are not required to separate the analytes from the bio-electrolytes.

In Chapter 4, five highly polar organic acids in serum were successfully quantified, and the SMALDI-MS results obtained on the desalted serum sample spots show both good reproducibility and compare well to sample studies by NMR. Putative identification of a total of 32 metabolites was accomplished in blood using time of flight MS with SMALDI, by comparison to tabulated data.

Chapter 5 concludes the current progress in this work and proposes future research.

# CHAPTER 2 MECHANISM OF DNA TRAPPING IN NANOPOROUS STRUCTURES DURING ASYMMETRIC PULSED FIELD ELECTROPHORESIS<sup>1</sup>

## 2.1 Introduction

The separation of megabase DNA in pulsed-field gel electrophoresis (PFGE) requires more than 24 h, because the electric field is limited to 10 V/cm or less.[15, 172, 173] As field strength is increased, DNA is trapped in the sieving matrix, causing smearing of DNA bands.[28] Large size DNA is essential to genomics research[174], particularly for the isolation, characterization and analysis of genes spanning large regions, construction of chromosome libraries[175], and long-range analysis of complex genomes[176]. Asymmetric pulsed field electrophoresis (APFE) in microfabricated artificial gels, such as nanopost arrays and colloidal crystals, dramatically decreases the separation time of 2 kbp ~209 kbp DNA to 15 s.[13, 17, 20] However, we find large size linear ds-DNA (>100 kbp) are trapped by APFE in three dimensional colloidal crystalline arrays, just as they are in gels, although at higher field strength (>80 V/cm) compared to gels.

The possible mechanisms of DNA trapping in gel electrophoresis have been explored. Turmel et al discussed the trapping of large DNA in gels, in the context of how modulated pulsed field methods could be used to greatly reduce trapping.[28] Using a model of DNA occupying a linear tube volume, DNA trapping was attributed to local conformational

---

<sup>1</sup> A version of this chapter is published in *Analyst*, vol. 139, issue 22, 6044-6051.

“defects”, such as dense regions in the gels and the formation of hernias.[28] Hernias, where multiple segments of a strand attempt to act as the head of the moving chain, causing complex and convoluted shapes, have been observed by single molecule fluorescence microscopy.[34, 177] Turmel et al also suggest that a short reverse field spike can make each segment of the molecule move backward by approximately one pore, which results in the relaxation of “defects”, detrapping DNA. Viovy proposed the trapping doesn’t arise solely from the arrest of chains as discussed by Turme et al. Instead, Viovy envisions DNA is trapped in topological knots around a gel fiber,[14] though the dynamics of such traps have been neither studied nor observed by single molecule imaging yet. The simple U- or J-shaped configuration , or hooked DNA, which can be a stable trap in a continuous field,[15] is not the only factor in trapping in a pulsed-field, since the U can relax through the reorientation induced by the pulsed field. The tension at the apex of a U-shape has been estimated[15, 178] and identified as arising from solid friction between DNA and the gel fiber.[37, 178] However, Viovy has pointed out the solid friction model fails to predict several aspects of experimental observations, such as the onset of a critical trapping voltage.[38]

In this chapter, we present experimental results from single ds-DNA molecule studies that provide insight to the mechanism of DNA trapping in pulsed-field electrophoresis in three dimensional colloidal crystalline arrays. We selected ds-T4 DNA separated in a structure with  $\sim 105$  nm pores as a model system. Utilizing a 2-D microfluidic device with an ordered, crystalline sieving matrix of silica particles[20], we find no evidence that trapping is caused by blockades in dense regions[28] due to the high order of these structures

compared to a gel. We find that trapping starts from a hook with two fully stretched arms. Multiple segments may attempt to serve as the head for motion in the newly applied field direction, creating hernias. Hernias are a common feature of trapped DNA, confounding the intended ratchet motion wherein only apex segments lead the molecular reorientation.[19] Our results demonstrate that at higher electric field, there is a higher probability of forming these hernias. We also find that the unhooking time of U/J shaped DNA is much longer than expected from a simple rope-on-pulley model, even after confinement by a nanoporous structure has been taken into account. The pinning at the apex of U/J is not simply due to the symmetric arm lengths. We present a modified unhooking time model which suggests the reduced mobility of DNA segments at an apex arises from a trapping force localized at the apex, yielding more fully-stretched DNA and near-apex hernias. We assign this trapping force to dielectrophoretic (DEP) forces in the tight confines of the pores, noting that the magnitude and field dependence of trapping observed is consistent with the DEP force model. Differing from DEP trapping of biomolecules in ordered microfabricated structure in other applications,[60, 73-75, 179] the critical field strength and frequency for DNA trapping in pulsed-field electrophoresis is much lower, which we attribute to the participation of hernias. The mechanism proposed here also explains why reverse voltage spikes in the pulse sequence can reduce DNA trapping in both gel[28, 180] and crystalline arrays.

## **2.2 Experimental**

DNA electrophoresis was conducted in a 2D PDMS chip fabricated using standard soft lithography as described elsewhere.[181] A 10  $\mu\text{m}$  thick positive photoresist master (AZ-

4620, Clariant Corp.) was UV patterned on a 4" silicon wafer. Negative PDMS replicas were made by pouring a mixture of PDMS base and curing agent (10:1, w/w, Sylgard 184 silicon elastomer kit, Dow Corning) over the wafer, followed by curing at 60 °C overnight. PDMS replicas were removed from the master, and the reservoirs were cut by razors. PDMS replicas were rinsed with methanol and water, and sealed to piranha cleaned glass slides to assemble the devices.

The separation bed (4 mm × 4mm) and channels (100 μm × 4 mm) were filled with self-assembled arrays of 690 nm silica particles (Bangs Laboratories, particle size in diameter, CV ~15%), constructing a nanoporous structure with 105±15 nm pore diameter (Figure 2-1c, see Appendix A for rationale for using 105 nm pore size). The particles were packed following Yong Zeng's method.[20] After 10 min ultrasonication, 10 μL aqueous suspension of 690 nm silica particle (10% w/v) was injected into the rectangular buffer reservoir at the bottom (Figure 2-1a). The colloidal suspension quickly filled the microfluidic device due to capillary force and stopped at the outlet of channels. Subsequently, 2 μL distilled water was injected into the round sample reservoir to flush the suspension away from the sample injection channel. The flows of water and suspension were balanced at the bottom of the injection channel. The bottom buffer reservoir was subsequently covered with a PDMS film. The solvent was evaporated from other four buffer reservoirs which were left open, inducing the packing of colloidal particles. After packing is finished, the colloidal suspension in the bottom reservoir was replaced with 4×TBE buffer. The entire device, including all the reservoirs, was covered with a PDMS film.

T4 DNA (166kbp, Wako) was stained with YOYO-1 (Invitrogen) at a ratio of 1 dye molecule to 10 base pairs. Loading buffer is 4×TBE with 4% β-mercaptoethanol to suppress photobleaching. To examine the macroscopic behavior of DNA trapping at high field, a plug of T4 DNA (30 ng/μL) was injected into the separation bed with 10 V/cm DC field. After the first few DNA molecules reached the separation bed, asymmetric pulsed fields  $E_1$  and  $E_2$  (Figure 2-1b) were applied to deflect the DNA stream (Figure 2-1b). The angle between pulsed fields is  $135^\circ$  and  $E_1 = \sqrt{2}E_2$ . The DC injection field was turned off one minute after a plug of DNA had entered the separation area. The trace of the deflection band was visualized with an epi-fluorescence microscope (Olympus 4X and 10X objective). The captured image stacks were processed with ImageJ. As shown in Figure 2-1b, the intensity of a T4 DNA deflection band over time was measured at 0.54 mm downstream (white dash line). The dynamics of individual DNA molecules under APFE was studied with a total internal reflection fluorescence (TIRF) microscope (Nikon Eclipse TiE) using a 60x oil immersion objective (Nikon). The space resolution is 0.24 μm per pixel, as determined by calibration with a standard. The videos were captured by CCD camera (Photometrics QuantEM:512SC) at 30 frames per second in overlap mode and processed by NIS-Element. The trapping of molecules was analyzed frame by frame. We selected some videos to support the discussions in this chapter, and the video captions are listed in Appendix B. The videos are available with the electronic archive. See DOI: 10.1039/c4an01364f

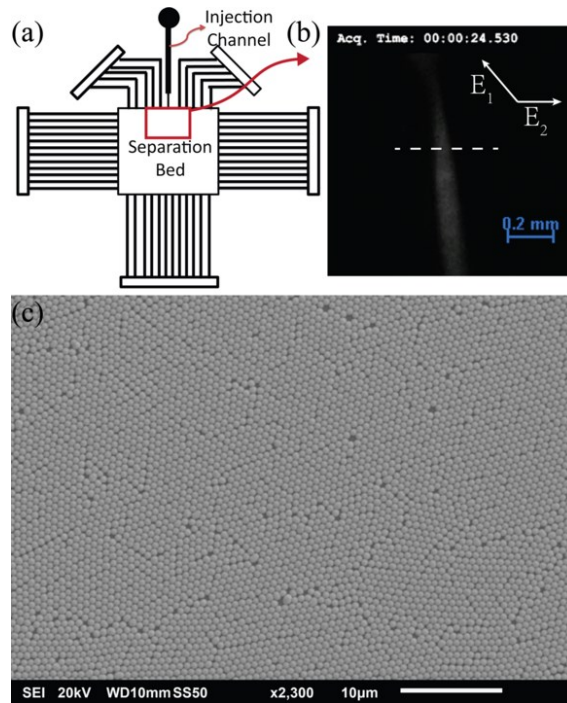


Figure 2-1: a) Schematic of the microchip for DNA separation. The separation bed and microchannels are filled with a colloidal crystal of silica particles, except for the injection channel. b) Fluorescence micrograph (4X objective) of deflection band of a T4 DNA plug under asymmetric pulsed field electrophoresis (APFE).  $E_1$  and  $E_2$  are two square wave pulses in APFE.  $E_1 = \sqrt{2} E_2$ . Frequency is 0.5 Hz. The dashed line represents the position for measuring fluorescent intensity. c) SEM image of the polycrystalline silica (690 nm diameter) in the separation bed.

Lengths of hooked DNA were measured, and those in the range of 55 to 65  $\mu\text{m}$  observed length were evaluated using the rope on pulley model. At 202.2 V/cm, our measured contour length is  $62 \pm 2 \mu\text{m}$ . (The true contour length of unlabeled T4 DNA is 55.8  $\mu\text{m}$ , with an observed length for fluorescence detection of the labeled molecule ranging from 60 to 65  $\mu\text{m}$ . [182, 183]) For analysis,  $t = \text{zero}$  was established at the time where no coiling was visible on the shorter segment, and the total length lay within the stated range above.

## **2.3 Results and discussions**

### **2.3.1 Macroscopic behavior of T4 DNA trapping**

Without trapping, the motion of DNA in APFE should follow a ratchet model,[13, 40, 184] wherein a DNA stream or plug migrates vertically while being deflected at a certain angle (Figure 2-2, a-c). As the voltage switches, the head and tail of the stretched DNA switch roles, leading to angular dispersion dependent upon size, when conditions are appropriate for the ratchet model to apply. However, trapping of large DNA at higher fields occurs within the nanoporous particle lattice. In Figure 2-2c, an injection plug of DNA was formed by turning off the voltage on the injection channel after a brief injection, while retaining voltage in the separation bed. The snapshot (Figure 2-2d), taken 7 min later, shows that instead of moving out of the view field, part of the DNA plug was trapped in the nanoporous structure. Figure 2-2e shows the intensity profile of the pixels along the arrow in Figure 2-2d, indicating DNA molecules were trapped.

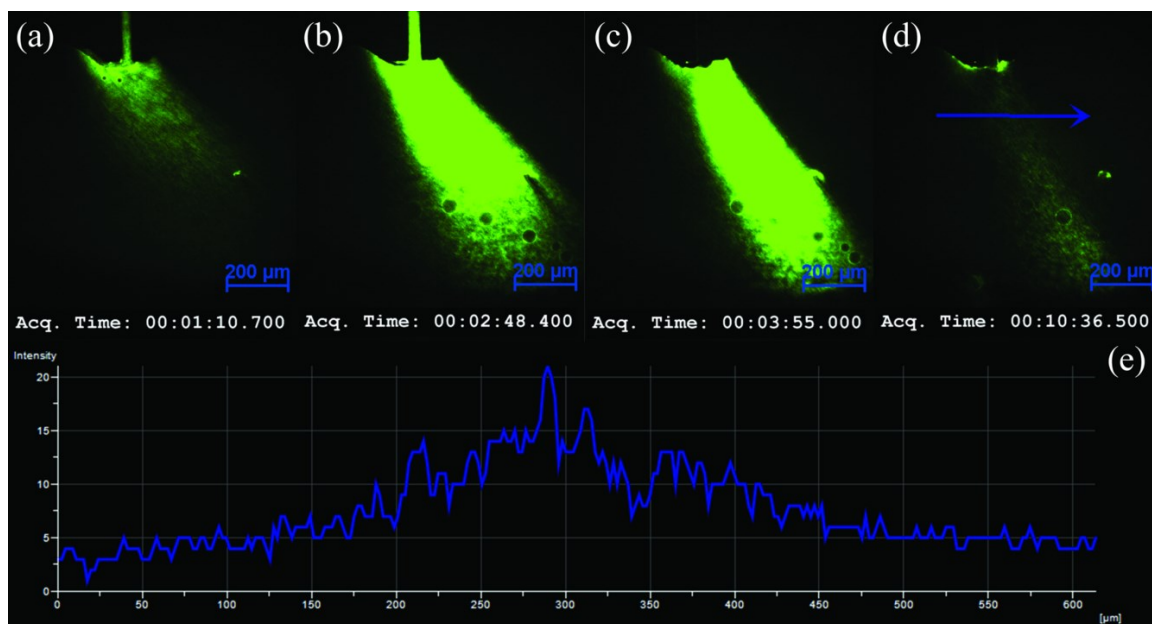


Figure 2-2: a-d) Migration of a T4 DNA plug in the separation bed captured by fluorescence microscope (10X objective). The field strengths of asymmetric pulsed-fields  $E_1$  and  $E_2$  were 202.0 V/cm and 142.9 V/cm, respectively, with 0.5 Hz frequency. The time trace started at the beginning of 2D separation. In c), continuous injection was stopped, creating an empty injection channel and a plug of injected material. e) The intensity profile along the blue arrow in d), showing some DNA was trapped in the sieves and did not continue along with the main sample plug.

DNA trapping in a porous crystalline lattice of particles occurs when the field strength is beyond a critical value,  $E_{crit}$ . Figure 2-3 shows the intensities of an injected T4 DNA plug as it progresses past the observation line shown in Figure 2-2, as a function of time. The intensities were extracted from the maximum intensities in each frame. At  $E_2=71.4$  V/cm, DNA molecules migrate through the bed without being trapped, showing a sharper band, or narrower injected plug width, in Figure 2-3a. DNA is partially trapped at 114.3 V/cm and 142.9 V/cm, giving longer transit times across the observation line, seen as broader bands in Figure 2-3. The trapping in a particle-based lattice follows the same trend as in a gel,[14, 28] except that  $E_{crit}$  is much higher than that in gel, leading to more rapid separations.

DNA trapping is reduced when reverse spikes  $E_1^*$  and  $E_2^*$  are inserted into the two primary pulsed fields (Figure 2-3b). A reverse spike was applied, following each forward pulse, in the opposite direction with half the magnitude (parameters given in Table 2-1). As expected, the apparent mobility is decreased by the reverse spikes. The effect of reverse spikes on a single DNA molecule is illustrated by TIRF videos 2-1 and 2-2, which compare results without and with the spikes, respectively. The electric fields applied in videos 2-1 and 2-2 are the same as those for the black and red curves in Figure 2-3b, correspondingly. Without reverse spikes, DNA molecules are trapped by high electric field ( $E_2=142.9$  V/cm) by the end of video 2-1, while the molecules are not trapped in video 2-2. The videos cover a period of time of 28 and 41 seconds, respectively. The importance of the effect of reverse spikes on understanding trapping is further explored below.

Table 2-1: Parameters of forward pulses and reversed spikes

|                              | $E_1$   | $E_1^*$   | $E_2$  | $E_2^*$   |
|------------------------------|---|---|--|---|
| <b>direction</b>             |  |  |  |  |
| <b>Field strength (V/cm)</b> | 202.1   | 101.0   | 142.9  | 71.4  |
| <b>Duration time (s)</b>     | 1.0   | 0.1   | 1.0  | 0.1   |

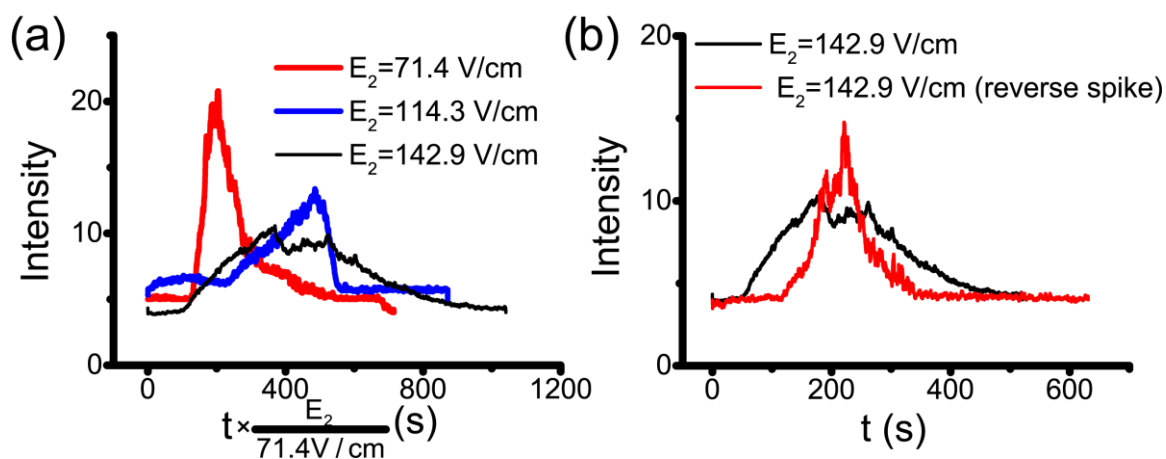


Figure 2-3: a) Intensity-time curves at several fields pulsed at 0.5Hz. Intensity was measured 0.54 cm downstream (dashed line in Figure 2-1b). Time was normalized by field strength. Trapped DNA causes a broad band, while mobile DNA gives sharper spikes. b) Effect of reversed spikes on DNA trapping at high electric field.  $E_2 = 142.9$  V/cm,  $f = 0.5$ Hz.

### 2.3.2 Dynamics of single DNA trapping and the role of hernias

Single molecule observations captured the dynamics of DNA trapping in crystalline sieves, as illustrated in Figure 2-4 and Video 2-3. As a first step the molecule hooks around a silica particle and is stretched (Figure 2-4a), then, after the field switches to  $E_2$ , hernias form and grow, with various segments vying to act as the head of the molecule (Figure 2-4b). The molecule does not move as predicted by the ratchet model, and ends up trapped in the matrix (Figure 2-4c). We note that these effects are field dependent, and do not occur at lower fields, such as 71.4 V/cm, ruling out adsorptive interactions with the silica as a primary cause. Additionally, the 4x TBE buffer was selected to reduce electroosmotic flow and zeta potential of the silica, which reduces DNA-silica interactions.

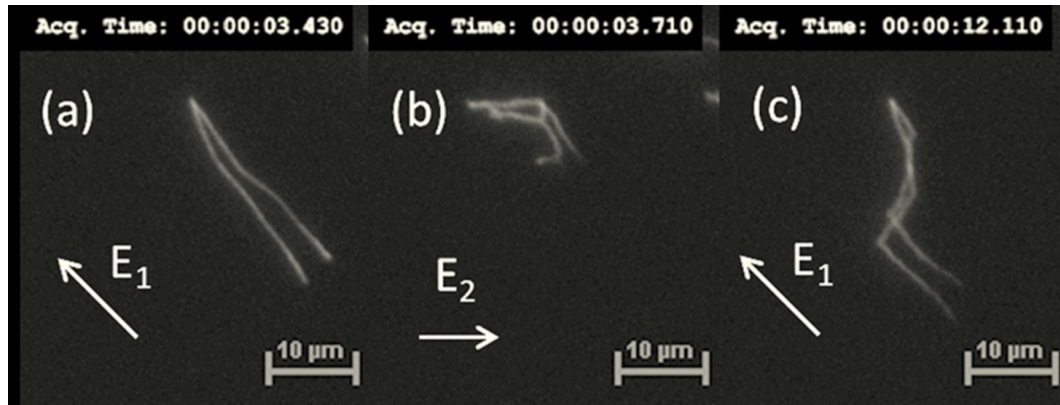


Figure 2-4: TIRF micrograph of a single DNA trapped in APFE.  $E_2 = 142.9$  V/cm,  $f = 2$  Hz. a) DNA collides with, then hooks around a silica particle. b) Hernias form after electric field switches. c) The conformation of trapped DNA at 2 Hz. The process of single DNA being trapped at the same field strength, but 0.5 Hz, was recorded and is displayed in video 2-3.

Apart from the field strength, the length of a hernia also depends on DNA conformation, as part of a molecule may be coiled before it is reoriented by the electric field, and the coiled segments are more favorably disposed to form hernias than the stretched part. The formation of a hernia from a coiled region is commonly referred to as leakage from the tube model for DNA. Fortunately, the results of the reverse spike experiments offer a route to simplify the analysis of trapping. When reverse spikes are inserted into the two primary pulsed fields, DNA molecules are not trapped, as the fully stretched U-shapes are relaxed and released. A similar result is observed when the field is intermittently interrupted at the same frequency as used for reverse spikes. We infer that being fully-stretched can be treated as a requisite for the trapping, so that our analysis can be confined to the study of fully stretched DNA.

The influence of hernias on DNA trapping at different fields is shown in Figure 2-5. According to the ratchet model, it is the apex segments that lead the reorientation of hooked DNA, and for the DNA shown in Figure 2-5a, the hernias are segments  $h_1$  and  $h_2$ . The length of a hernia as it grows from an individual fully stretched U-shaped molecule was plotted as a function of time (Figure 2-5), once the field was switched to  $E_2$ . The results show at low fields the hernias tend to shorten and often are extinguished over time, while at higher electric fields, the hernias are longer in duration and in physical length. Thus, there is a higher probability of forming hernias and those hernias have a greater chance to be substantially stretched, trapping the molecule, when fields are higher. Hernias are very common in pulsed-field electrophoresis in general, and their lengths are theoretically predicted to increase with electric field,[32, 54] consistent with our results in the crystalline sieves.

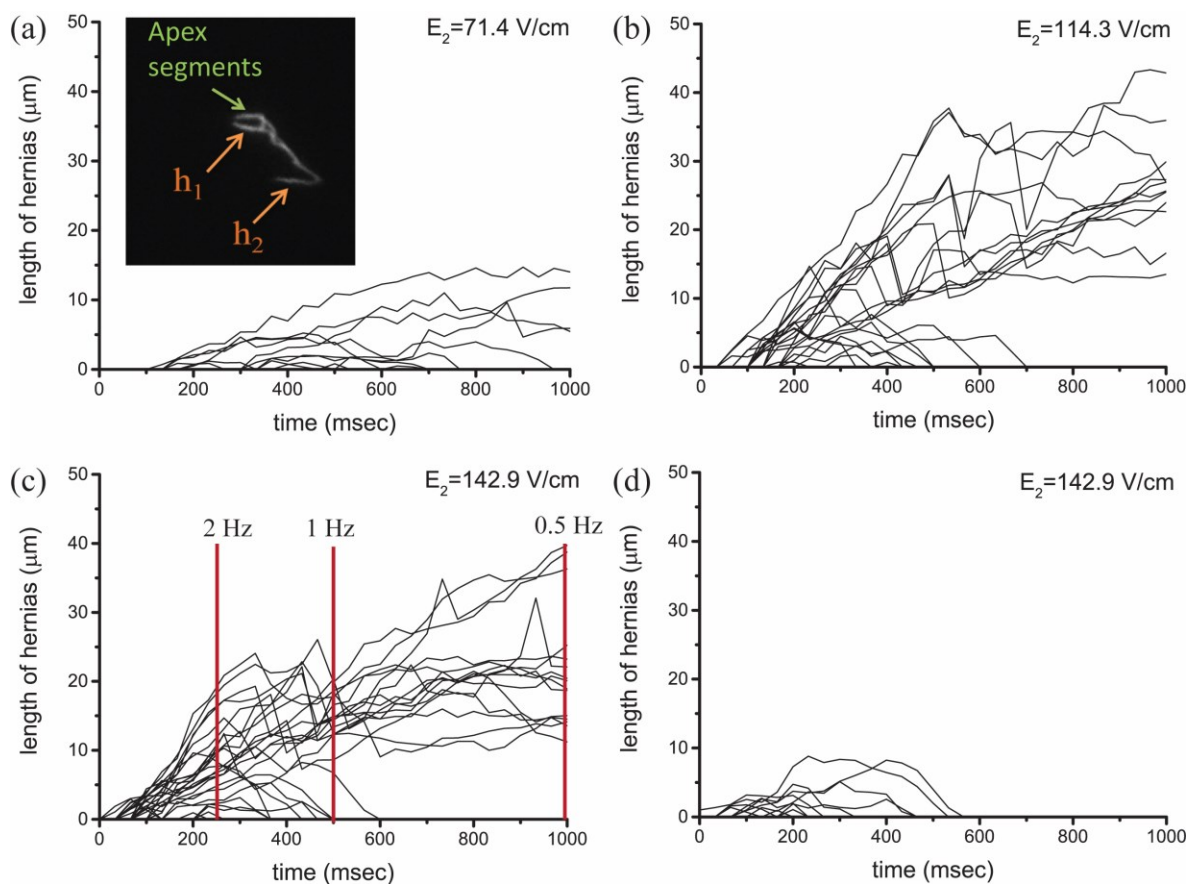


Figure 2-5: a) The comb-like conformation of hernias after electric field switching. Apart from the apex segments, which should lead the molecule's reorientation according to the ratchet model, other segments responding to the field are labelled as hernias. For all studied molecules, the length of hernias was measured every 33 ms after the field was switched to  $E_2$ . For the molecule shown in the image, the total length of hernias =  $2h_1 + h_2$ . a-c) The total lengths of hernias are shown as a function of time at several field strengths, with 50 molecules presented in each graph. The red lines in c) represent the duration time of the  $E_2$  portion of the field pulse on the x-axis for the frequencies indicated. d) 30 hernias formed at  $E_2 = 142.9 \text{ V/cm}$  were identified as either distant hernias or near-apex hernias (within  $2.8 \mu\text{m}$  of the apex, 5% of contour length). The evolution traces isolated for distant hernias is shown in d), indicating all the long lasting hernias in c) are near-apex hernias.

The data in Figure 2-5 were extracted from 0.2 Hz APFE experiments, in which the duration time of each pulse is longer than the reorientation time. This pulse period is long enough that the field strength is the physically dominant variable for the study of hernias,

allowing evaluation of the formation, stretching and elimination from an initially fully-stretched U/J shape. The trapping dynamics are followed for molecules transitioning from the free state, to the U/J hooked state, and then into hernia formation and evolution. The results show  $\sim 0.5$  s is a watershed for the growth of hernias at high field, as many hernias are eliminated at this point. Surviving hernias beyond 0.5 s are substantially stretched and lead the reorientation when the field switches, instead of the apex segments.

For the same electric field, hernia evolution is cut short as a result of the shorter pulse durations at higher frequencies, as suggested by the red lines in Figure 2-5c. For example, at 2 Hz, most of the dangling hernias like  $h_2$  will not be eliminated during the reorientation and may cause trapping. Video 2-4 and Figure 2-6 show DNA trapped at 0.5 Hz ( $E_2=142.9$  V/cm). When compared to the conformation of trapped DNA at 2 Hz (Figure 2-4c, video 2-3), it is clear that at 0.5 Hz the DNA only loses its mobility at the apex, with the two arms still shuttling through nanopores under the pulsed-fields (Figure 2-6). Notably, it is hernias near the apex location that tend to become extended and trapped, as no distant hernias survive after  $\sim 600$  ms; all long lived hernias reside in the near apex region, as indicated in Figure 2-5d. This observation is significant given that those near-apex hernia segments, like  $h_1$  in Figure 2-5a, clearly exhibit comparable or larger mobility than the apex segments, and attempt to act as the head of a molecule after the electric field switches.

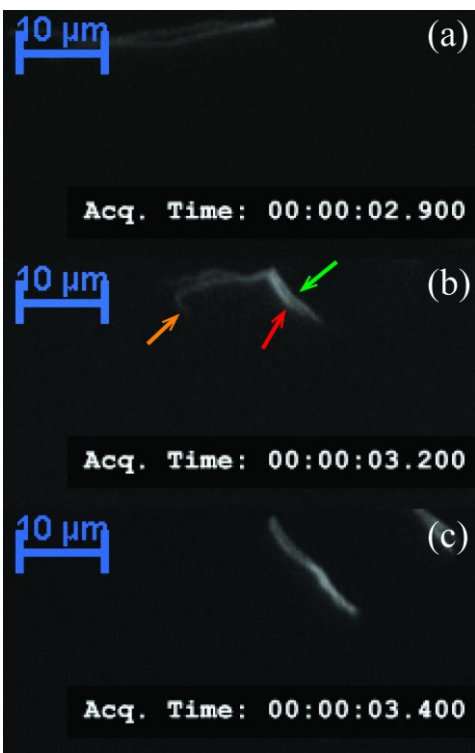


Figure 2-6: Time-lapse images of video F4. DNA is trapped at 0.5 Hz. In b), both near-apex hernia (red arrow) and distant hernias (orange arrow) form. The green arrow points to the apex segment which has reoriented, along with the near-apex hernia pointed by the red arrow. The distant hernia disappears with time as seen in c), while the near-apex hernia is substantially stretched. As an overall result, the apex is immobilized.

It is clear from our data that trapping of the apex itself is a significant feature of the trapping phenomenon, even though the formation of hernias is a more visually obvious trapping characteristic. This conclusion is further supported by the fact that reverse spikes reduce trapping, even though these spikes can actually increase the rate of hernia formation through forming more coiled segments via DNA relaxation. Taken with the results presented below, and in Figure 2-5 (c-d) for high fields, it is evident that long lived hernias are generated as a result of affects near the pinned apex state, not from tube leaks generated from coiled segment lengths or other defects. We conclude that hooking is the primary

requisite for trapping, and that hernias, while appearing significant in causing trapping are actually a consequence of the hooks that are the primary source of trapping.

### 2.3.3 Role of hooking

Hooking has also been recognized as playing a role in trapping DNA. The U/J shaped hook, and the time to release this hook, has been described by a rope-on-pulley model.[185, 186] However, unhooking times observed at fields where trapping occurs are much longer than predicted by the rope-on-pulley model. Video 2-5 shows a J-shaped DNA that cannot be unhooked under high electric field ( $E_1=202$  V/cm). We propose that the factors that account for the delayed unhooking, also accounts for the decreased mobility seen at the apex of herniated DNA as electric field is switched, discussed above.

We measured the unhooking time of fully-stretched U/J shaped DNA in crystalline sieves and compared the results with an unhooking time model[50]:

$$t_{unhook} = -\frac{L}{2\mu E} \ln\left(1 - \frac{2x_1}{L}\right) \quad (\text{Equation 2-1})$$

which is derived from the rope-on-pulley model. In Equation 2-1,  $L = 55.8 \mu\text{m}$  is the contour length of T4 DNA and  $x_1$  is the length of the short arm (Figure 2-6a). The model was initially proposed to describe the unhooking dynamics after DNA collides with a single post in free solution. To apply Equation 2-1 to the nanoporous structure, we retain a rope-on-pulley model, but account for strong restrictions of motion in this confined structure, by replacing the free solution mobility  $\mu_0$  with  $\mu$ , the mobility of confined DNA.

Mobility  $\mu$  cannot be directly obtained by measuring the DNA migration time, because DNA molecules frequently collide with silica particles and transform among different conformations, slowing down the migration rate. In free solution, for the situation in which a polyelectrolyte is fully stretched by a strong field, we use a local force model in which the frictional force is equivalent to the electric field force, giving:

$$\xi\mu E = Eq_{\text{eff}} \quad (\text{Equation 2-2})$$

where  $q_{\text{eff}}$  is the effective charge of DNA and  $\xi$  is the hydrodynamic friction coefficient. Equation 2-2 is generally applied to the ideal unhooking of U/J at high field.[50, 187] We assume  $q_{\text{eff}}$  of T4 DNA does not change with DNA conformation. Therefore, according to Equation 2-2, mobility is inversely proportional to the friction coefficient

$$\frac{\mu}{\mu_0} = \frac{\xi_0}{\xi} \quad (\text{Equation 2-3})$$

The friction coefficient in free solution is [188]

$$\xi_0 = 6\pi\eta g_r \quad (\text{Equation 2-4})$$

With equation 2-2 and 2-4, we calculate  $q_{\text{eff}} = 0.034$  electrons per base pair (see Appendix C), consistent with the value obtained by Smith.[189] Because the pore diameter in crystalline sieves is about 105 nm, twice the DNA persistence length (50 nm), the DNA confined in the nanoporous structure falls into Odijk's regime, leading to a friction coefficient[46, 190]

$$\xi = \frac{2\pi\eta L}{\ln(4D/\pi w)} \quad (\text{Equation 2-5})$$

Substituting Equation 2-4 and 2-5 into Equation 2-3, with radius of gyration  $g_r = 1.31 \mu\text{m}$ , [191] pore diameter  $D = 105 \text{ nm}$  and diameter of DNA  $w = 2.4 \text{ nm}$ , we get  $\mu = 0.279 \mu_0$ . The measured free solution mobility  $\mu_0$  of DNA in 4x TBE buffer is  $(3.175 \pm 0.059) \times 10^{-8} \text{ m}^2/(\text{v} \cdot \text{s})$ .

After rewriting the mobility expression, the theoretical unhooking time (solid curves in Figure 2-7, b-d) can fit most experimental values (dots) at low field ( $E_2=74.1 \text{ V/cm}$ ). The unhooking time was measured as starting when the short arm was fully-stretched under the pulse  $E_1$ , not from the initial collision. At this point in time, given the high field strength and confining pore structure, the long arm of a hook is highly extended. As field strength is increased, the experimental values deviate from the theoretical plots. At higher fields, some U/J shaped molecules are pinned at the apex, showing infinite unhooking time. Experimentally, unhooking times longer than 1.5 s at  $E_2 = 74.1 \text{ V/cm}$  and those longer than 1 s at  $E_2 = 114.3$  and  $142.9 \text{ V/cm}$  are taken as infinite, and plotted as red dots in Figure 2-7.

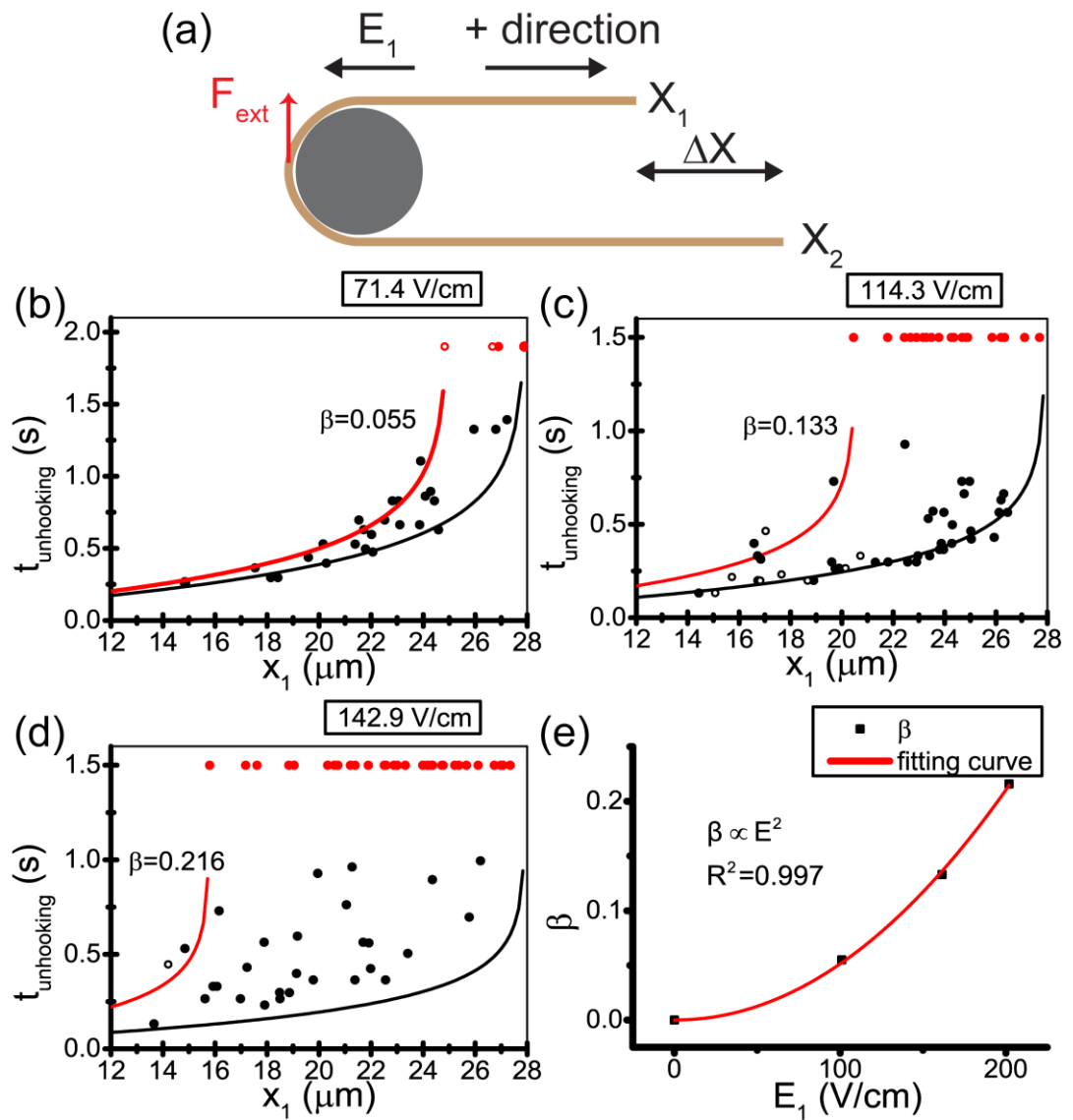


Figure 2-7: a) Scheme of “rope-on-pulley” model. The negatively charged molecule should slip away from the J-shape under the external electric field  $E_1$ , due to the unequal lengths of the two arms. b-d) Unhooking times of U/J shaped DNA at different electric fields. The solid lines follow the theoretical model of Randall et al. with  $\beta = 0$ . The red lines follow the modified model of Equation 2-7, for the maximum of  $\beta$  as determined at different field strengths. Dots represent experimental unhooking times. Red dots represent infinite unhooking time, appearing at 1.5 s on the y-axis. The solid dots represent the first data set which was obtained from complete sample statistics in several TIRF videos. The hollow dots represent a second data set which only focused on shorter  $x_1$ . e) Scaling relation between dielectrophoresis parameter  $\beta$  and electric field strength.

Based on the experimental unhooking time data, we propose there is an external force other than the electrophoretic force acting on the apex segments and resisting the rope-on-pulley motion. Randall et al gave the equations of motion of two arms in the simple rope-on-pulley model[50]

$$j\xi\left(\frac{dx_1}{dt} - \mu E\right) = -T \quad (\text{Equation 2-6a})$$

$$(N - j)\xi\left(\frac{dx_2}{dt} - \mu E\right) = -T \quad (\text{Equation 2-6b})$$

where  $j$  is the number of base pairs on the short arm,  $N=166$  kbp for T4 DNA, and  $T$  is the intramolecule tension connecting the short arm and the long arm at the apex. Assuming there is an external force  $F_{ext}$  at the apex, Equation 2-6a is changed to

$$j\xi\left(\frac{dx_1}{dt} - \mu E\right) = -T + F_{ext} \quad (\text{Equation 2-6c})$$

$F_{ext}$  resists the short arm sliding over the hooking spot while it is stretched by electrophoretic force, which results in more fully-stretched DNA. As described in the paper by Randall et al., the unhooking time can be solved by integrating the difference of Equation 2-6b and 2-6c, using  $dx_1/dt = dx_2/dt$  and  $j/N = x_1/L$ :

$$t_{unhook} = -\frac{L}{2\mu E} \ln\left(1 - \frac{1}{1-\beta} \frac{2x_1}{L}\right) \quad (\text{Equation 2-7})$$

In Equation 2-7, the newly defined parameter

$$\beta = F_{ext}/\xi\mu E \quad (\text{Equation 2-8})$$

The new unhooking time model requires  $1 - 2x_1/(1 - \beta)L > 0$ , predicting that unhooking is only possible when the length difference of two arms  $\Delta x > \beta L$ . Otherwise, the unhooking time is infinite.

The value of  $\beta$  can be obtained from the critical condition  $\Delta x = \beta L$ . The critical  $\Delta x$  of each subplot from Figure 2-7b to 2-7d is determined by the leftmost red dot, using  $L = 2x_1 + \Delta x$ . The dashed lines in Figure 2-7 are plots of Equation 2-7. The two unhooking time models form the left and right bounds of a 2D value domain for experimental values at different electric fields. The solid dots in Figure 2-7 were collected from a complete sample, which reflects the real distribution of unhooking times of substantially stretched  $U/J$  at different fields. A second data set, shown as hollow dots, was collected, focusing on shorter values of  $x_1$  to ensure the accuracy of  $\beta$  and test the new model. These data points for more extreme J-shaped configurations also fit within the bounded domain of the two equations.

### 2.3.4 Dielectrophoretic trapping

We propose the source of  $F_{\text{ext}}$  is a dielectrophoretic (DEP) force. Figure 2-7e shows the scaling relation between  $\beta$  and field strength is  $\beta \sim E^2$ , suggesting  $F_{\text{ext}}$  must quickly increase with  $E$ , according to Equation 2-8. In a non-uniform electric field, polarizable molecules are subjected to a DEP force  $F_{\text{DEP}}$ :

$$F_{\text{DEP}} = \alpha \nabla |E|^2 \quad (\text{Equation 2-9})$$

where  $\alpha$  is a molecules polarizability.[73, 192] The electric field in the separation bed is non-uniform, owing to the different permittivity's and conductivities of 4x TBE buffer and silica particles. Simulation results (Figure 2-8) show both the electric field and the field gradient  $\nabla|E|^2$  are significantly higher at the contact zone of two particles along the direction of the field. The electrophoretic force on the two arms of U/J molecules presses the apex segments close to the particle where E and  $\nabla|E|^2$  are higher in comparison to the pore, and the positive DEP force traps apex segments at the high field strength region, resisting unhooking.  $\nabla|E|^2$  is relatively small at other possible hooking spots on the particle surface. Therefore,  $F_{DEP}$  is variable at different hooking spots, just as is parameter  $\beta$ . We correlate the dashed lines in Figure 2-7 with the unhooking time model applicable at the highest field gradient areas shown in red in Figure 2-8, while DNA hooked at the lower field gradient, blue areas, have shorter unhooking time with a smaller  $\beta$ . This interpretation explains the scattered distribution of experimental values, lying in a range between the extreme trapping of the maximum value of  $\beta$  and that of the original rope-on-pulley model with a  $\beta$  of zero.

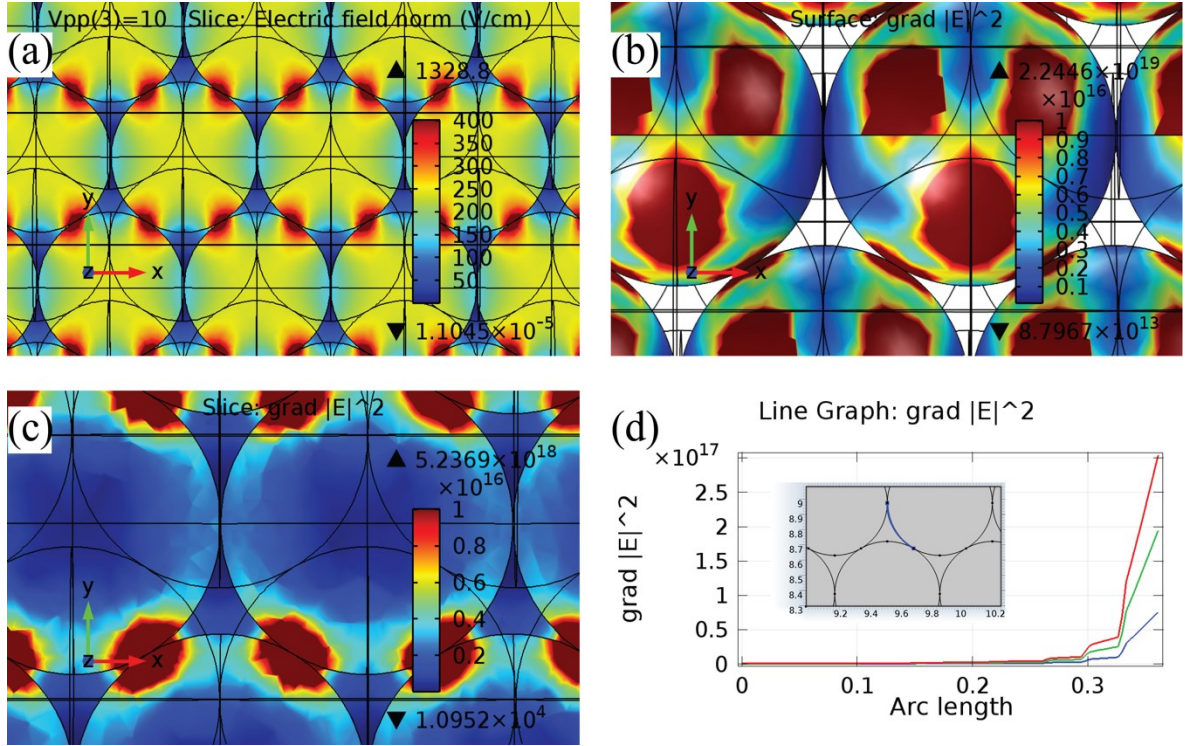


Figure 2-8: Simulation results of electric field gradient  $\nabla|E|^2$  in the nanoporous structure. The permittivity of 4X TBE buffer and silica particle are  $77.232 \epsilon_0$  [193] and  $4.2 \epsilon_0$ , respectively. The conductivity of buffer and silica are 0.22 and  $1 \times 10^{-10}$  S/m, respectively. The direction of applied electric field is from left to right. Field strength  $E$  is non-uniform in the nanoporous structure. a) Field strength  $E$  is non-uniform in the nanoporous structure. b-c) Field gradient  $\nabla|E|^2$  plotted in 2D graphs, showing b) the gradient on the silica surface, as a projection of the upper surface onto a plane passing through the particle's centre, parallel to the direction of the field, and c) a two-dimensional slice taken along the same plane, showing the field gradient in the pore. Red is high field gradient, blue is low. d) Field gradient on a selected buffer-silica interface (blue arc in the inset). The red, green and blue lines represent the field gradient at an average field  $E_1 = 202.0, 161.6$  and  $101.0$  V/cm, respectively.

Using the assumption that a DEP force is the external force at the apex, we calculated the T4 DNA polarizability  $\alpha = \beta \xi \mu E / \nabla|E|^2$  by substituting Equation 2-9 into Equation 2-8. At  $E_2 = 142.9$  V/cm, where trapping is obvious, we calculate  $\alpha = 1.31 \times 10^{-29} \text{ Fm}^2$ , using  $\beta = 0.216$  which is obtained from the unhooking time experiment (Figure 2-7d),  $\xi \mu = 6\pi \eta g_r \mu_0$  (Equation 2-3 and 2-4) with viscosity  $\eta = 1.16$  cP, [194]  $E = E_1 = 202.1$  V/cm

and the maximum field gradient  $\nabla|E|^2 = 3.04 \times 10^{17} \text{ mkg}^2/(\text{s}^6\text{A}^2)$  at the contact area of two particles (Figure 2-8d). The calculated DNA polarizability is of the same magnitude of the reported value,[64] strongly supporting our DEP force model.

There are two other possible external forces, hydrodynamic friction and solid friction. In unhooking time models, hydrodynamic friction is already included through the mobility  $\mu$ , and cannot lead to infinite unhooking times according to Equation 2-7. Burlastky et al. proposed solid friction between DNA and gel.[37] Assuming the friction coefficient is  $\mu_f$  and substituting  $F_{ext} = \mu_f E q_{eff}$  into the definition formula of  $\beta$ , the parameter  $\beta = \mu_f q_{eff} / \mu \xi$  becomes field independent, in contrast to the observed scaling relation. Interaction between DNA and the electrical double layer at the silica interface is another potential source of an external force. For the buffer used here, the Debye length is 0.743 nm, which is substantially smaller than the region of high external field gradient that can generate a DEP force (see Appendix D).

From Equation 2-2, we obtain  $\beta = F_{ext} / \xi \mu E = F_{DEP} / F_{EP}$ . The physical meaning of parameter  $\beta$  is the ratio of DEP force at the apex to the electrophoretic force on the entire DNA molecule. The calculated values of  $\beta_{max}$  at different field strength are much smaller than 1, indicating that the DEP force is a modest perturbation on DNA electrophoresis. The dominant force in APFE experiments remains electrophoretic force, so the DNA plug can migrate downwards in Figure 2-2. However, at higher fields, the mobility of apex segments is reduced due to the presence of a positive DEP force, and the molecule becomes

pinned, forming U/J shaped hooks. Pinning at the apex then results in near-apex hernias, arising from the attempted reorientation of the molecules when the potential switches to create a ratchet and the apex cannot respond, so another portion of the molecule acts as the head, further compounding the trap for the DNA. Reverse spikes inserted within a given field direction of APFE dislodges the molecules from the high  $F_{\text{DEP}}$  zone, either directly, or through sufficient relaxation and recoil to mobilize away from the apex region, thus reducing trapping (video 2-6).

## 2.4 Conclusion

We reveal the primary mechanism of DNA trapping in colloidal crystal during pulsed-field electrophoresis is due to hooking, and show this is consistent with a dielectrophoretic trapping force. We have shown that as the field strength is increased, the magnitude of trapping force increases with a field dependence consistent with dielectrophoretic forces. Modeling of the electric field and field gradient at the contact zone of the particles shows the dielectrophoretic force available increases much faster than the electrophoretic force. Using the calculated force from dielectrophoresis and the observed trapping force provides an estimate of the polarizability of the molecule that is in agreement with literature values. At lower frequency ( $< 1$  Hz), the pinning of DNA at the apex of a hook to form the U/J shape is the trigger of trapping, followed by extended stretching of the DNA. Hernias are then formed, as other segments of the molecule attempt to become the head instead of the immobile apex, when the field direction is switched. These hernias can become permanent and compound the strength of the trap. At higher frequency (2 Hz), hernias appear to cause the trapping of T4 DNA, because the following reorientation takes place while the apex

segments and hernias are competing to act as head. However, the near apex hernias tend to dominate over time, and it is clear these form because of pinning of the apex, again illustrating that trapping at the apex is the initial trigger for irreversible trapping.

The trapping mechanisms discussed for gels are more varied than those we report here for a particle-based sieve structure. Trapping in the particle beds is readily understood in terms of macroscopic forces (DEP) and polymer dynamics, in contrast to DNA trapping in gels. As discussed in the introduction, a friction force at the hooking intersection of DNA and gel strand has been invoked, but the model does not describe all of the experimental results, yet evidence that pinning at the origin of the hook for a U-shape does exist. In the particle matrix, the macroscopic dielectrophoretic force does explain the importance of hooking in trapping of DNA. In both gels and in the particle sieves investigated here, the effect of reverse spikes in the field is to relax the DNA strands and allow them, or encourage them, to mobilize away from the apex trapping points associated with hooks. In the case of the particle sieves the mechanism of trapping by hooking can clearly be linked with dielectrophoresis, while it remains partly obscured in gels.

The model proposed here is applicable to linear ds-DNA. Insulator-based dielectrophoresis (iDEP) trapping of single strand DNA and supercoiled plasmid DNA has been reported by several groups, confirming that similar forces will be at play with those materials. However, to apply the model we have developed, one would have to take into account how the polymer physics changes for these forms of DNA relative to the linear, ds-DNA studied here.

**CHAPTER 3 SALT SEGREGATION AND SAMPLE  
CLEANUP ON PERFLUORO-COATED**

# NANOSTRUCTURED SURFACES FOR LASER DESORPTION IONIZATION MASS SPECTROMETRY<sup>2</sup>

## 3.1 Introduction

Laser desorption ionization (LDI) from porous silicon (pSi)[87, 90] and other porous nanostructured materials[102, 104, 195-197] is a useful method for soft ionization of low mass samples in the range of 100 to ~3000 Da. The high sensitivity offered by pSi-LDI in this mass range makes it an optional detection method for metabolites. However, its advantage in convenient biofluid metabolite analysis is controversial or limited, as discussed in Chapter 1. Minimal sample preparation is needed for quantitation of less polar metabolite,[142, 169, 198] whereas the challenges from sample matrix components are significant in detecting highly polar metabolites.[125, 140, 141] In this chapter, we examine the sensitivity of a pSi-LDI surface fabricated from glancing angle deposition (GLAD) in metabolite analysis, and develop a desalting method for GLAD based pSi-LDI, allowing the convenient analysis of highly polar metabolites in salty samples.

Jemere et al have previously demonstrated solid matrix LDI (SMALDI) using silicon thin films fabricated by GLAD.[119] GLAD is an easily engineered and controlled thin film fabrication process wherein a flux of atoms evaporated by e-beam was deposited on

---

<sup>2</sup> This chapter is a portion of a paper submitted to Analytical Chemistry. Chen Peng is a co-author. She developed the perfluoro coating method on silicon GLAD film, and the results in Section 3.1 are summarized from her thesis. I developed the desalting method.

substrate at an obtuse angle ( $86^\circ$  in this thesis) and nanocolumns form due to a shadowing effect.[120, 199] Sub-fmol detection limits were achieved in Jemere's work using an older Voyager elite AB-Sciex MALDI-TOF instrument for molecular masses above 400 Da, low enough for evaluating laboratory prepared chemicals and peptides derived from tryptic digestion in proteomic analysis. Metabolite analysis requires high sensitivity to molecules in the mass range below 250 Da,[200] but the sensitivity of SMALDI is decreased below 400 Da due to background interferences.[139] Herein, we evaluate the challenges from background chemical noise below 250 Da, and explore the use of per-fluoro coatings on GLAD based SMALDI to reduce the background.

Using fluorocarbon coatings to improve the sensitivity of pSi-LDI has been demonstrated by the Siuzdak group using electrochemically etched pSi surfaces.[125] However, the performance is severely reduced by deposition of salt from biological samples,[108, 201] which undermine the aptitude of pSi-LDI for metabolite profiling. In this chapter, we demonstrate a novel, on-chip desalting technique for improving quantitative analysis by segregating metabolites from interfering background electrolytes, effected using a defect-laden perfluoro coating.

As a vehicle to evaluate the desalting performance of SMALDI chips, we have targeted free amino acids (FAA) which are important in neurotransmission and are implicated in neurotoxicity,[202, 203] and the salt matrix in this study is artificial cerebral spinal fluid (aCSF). Fonteh et al determined concentration changes in FAA of CSF in probable Alzheimer's disease (pAD) subjects as a potential metabolite biomarker family of

responses.[204] They compared pAD subjects with control subjects using liquid chromatography and electrospray ionization tandem mass spectrometry (LC-MS<sup>2</sup>), following a sample derivatization procedure. In this study, we demonstrate SMALDI chips can achieve detection of FAA concentration changes in aCSF, without any derivatization or chromatographic separation.

## **3.2 Experimental section**

### **3.2.1 SMALDI chip preparation**

Vertical nanocolumns 500 nm tall were deposited on piranha cleaned silicon wafer substrates (Silicon Materials, prime grade, 500  $\mu\text{m}$  thick) using GLAD. Substrates were maintained at a fixed deposition angle of  $86^\circ$  from normal, and substrate rotation was employed throughout the deposition (2.4 nm deposited/rotation). Electron-beam evaporation of silicon (Kurt J. Lesker, p-type, 99.999% purity) held in a Ta crucible and heated under vacuum was employed. The base pressure was  $\sim 5 \times 10^{-7}$  Torr, and the Si deposition rate (as measured with a quartz crystal thickness monitor oriented normal to the crucible) was  $\sim 1.6$   $\text{\AA}/\text{s}$ , leading to a column growth rate of  $\sim 5.5$  nm/min.

After deposition, the silicon GLAD films were handled in an ambient air environment, and therefore a native oxide formed on the silicon surface. The silanol-rich chip surface was fluorinated by soaking the chips in dilute solutions of (1H, 1H, 2H, 2H-perfluorooctyl) trichlorosilane (pFSiCl<sub>3</sub>, Gelest) or (1H, 1H, 2H, 2H-perfluorooctyl) dimethylchlorosilane (pFMe<sub>2</sub>SiCl, Gelest) for 30 min at ambient temperature. The silane solutions were

prepared by adding 10-200  $\mu\text{L}$   $\text{pFSiCl}_3$  or  $\text{pFMe}_2\text{SiCl}$  into 5 mL distilled methanol followed by 30 s of vortex mixing. The chips were then stored in a petri dish overnight. During this time the polymerization continued. The chips were then rinsed with liquid  $\text{CO}_2$  in a critical point drier (Tousimis Research Corporation) to remove trace methanol and excess silane reagent.

### 3.2.2 Sample preparation

Analyte standards (purity >99%) of histidine, glutamine, asparagine, lysine and des-Arg<sup>9</sup>-bradykinin were purchased from Sigma-Aldrich and prepared as stock aqueous solutions, diluted with water/methanol (50/50, v/v, purity of methanol > 99.9%) to obtain concentrations from 0.05 to 100  $\mu\text{M}$ . Des-Arg<sup>9</sup>-bradykinin solutions were diluted with 0.1% TFA/methanol (70/30, v/v). Artificial cerebral spinal fluid (aCSF) solution was prepared following the protocol from ALZET, and the components are listed in Table 3-1. To prepare the aCSF samples, the pure analytes were diluted with aCSF solutions from the stock to 0.5-100  $\mu\text{M}$ . For internal standard (IS) calibration curves of aCSF samples on 1% concentration  $\text{pFSiCl}_3$  coated surfaces, samples were prepared by mixing 1 aliquot of aCSF sample (10-100  $\mu\text{M}$  histidine or glutamine), 1 aliquot of 10  $\mu\text{M}$  asparagine in water as IS, and 4 aliquots of methanol. On  $\text{pSiFMe}_2\text{Cl}$  surfaces coated with a 1.2% solution, salt dilution of the sample was minimized, in order to mark the chips' high salt tolerance. A 200  $\mu\text{L}$  aliquot of aCSF samples was spiked with 2  $\mu\text{L}$  of IS in water. The original "analytical" concentrations in the aCSF samples are stated throughout.

Table 3-1: Artificial CSF (aCSF) composition and concentration (pH=7.3)

| Ion in artificial CSF         | Concentration (mM) |
|-------------------------------|--------------------|
| Na <sup>+</sup>               | 150                |
| K <sup>+</sup>                | 3.0                |
| Ca <sup>2+</sup>              | 1.4                |
| Mg <sup>2+</sup>              | 0.8                |
| PO <sub>4</sub> <sup>3-</sup> | 1.0                |
| Cl <sup>-</sup>               | 155                |

Source: [http://www.alzet.com/products/guide\\_to\\_use/cfs\\_preparation.html](http://www.alzet.com/products/guide_to_use/cfs_preparation.html)

### 3.2.3 Sample deposition and on-chip desalting

Pure samples in 0.8  $\mu$ L aliquots were spotted on 1% concentration pFSiCl<sub>3</sub> coated SMALDI chips and open-air dried at room temperature. For aCSF samples, 1.5  $\mu$ L aliquots were spotted on 0.3 % pFSiCl<sub>3</sub> or 1 % pFMe<sub>2</sub>SiCl fluorinated SMALDI chips with contact angles of 110-120°. To achieve desalting, the sample drops were dried in a small petri dish (Fisherbrand, 35 mm x 10 mm) at 4 °C for several hours.

### 3.2.4 Mass spectrometry

SMALDI chips were attached to a modified MALDI target plate with conductive double-sided carbon tape (Electron Microscopy Sciences). MS measurements were performed on a Voyager Elite MALDI-TOF mass spectrometer (AB Sciex) equipped with a pulsed nitrogen laser (337 nm, 3 ns pulse). Mass spectra were acquired in reflector, delayed extraction mode, and each spectrum is an output of 100 laser shots. Other instrument settings (Table 3-2) were applied for optimal resolution and S/N in the mass range below 400 Da.

Table 3-2: Instrument Settings of MALDI-TOF-MS

| <b>Ion Mode</b> | <b>Acceleration voltage (kV)</b> | <b>Grid Voltage (%)</b> | <b>Guide Wire Voltage (%)</b> | <b>Delay Time (ns)</b> | <b>Laser Intensity(a.u.)</b> |
|-----------------|----------------------------------|-------------------------|-------------------------------|------------------------|------------------------------|
| <b>Negative</b> | 18                               | 72                      | 0.05                          | 150                    | 2100                         |
| <b>Positive</b> | 20                               | 69                      | 0.07                          | 350                    | 2000                         |

### 3.2.5 Quantitative analysis

The S/N of peaks were calculated from raw spectral data by Data Explorer 4.0 (AB Sciex) without any data pre-processing. Limits of quantitation were defined as S/N of 10 and estimated from plots of S/N versus analyte concentration. The IS calibration curves were constructed by plotting the peak height ratios of analyte to IS versus the concentrations of analyte in aCSF; error bars represent the standard deviation from 10 sample spots. The statistical analysis for LOQs and interpolation of concentrations followed standard practice, outlined in Appendix E.

## 3.3 Results and discussion

### 3.3.1 Perfluoro coating improvements for low mass analytes

A series of studies were performed on Si-GLAD films prepared at 86° deposition angle, rotated so as to give vertical posts with a 20-50 nm columnar spacing, nominally 500 nm in film thickness. The films gave SMALDI detection of des-Arg<sup>9</sup>-bradykinin (904 Da) with a 0.6 fmol limit of quantitation (LOQ, defined throughout as a signal to noise ratio (S/N) of 10) in positive ion mode, comparable to the results reported for etched silicon surface

DIOS.[87] Background chemical noise and ion suppression due to the sample matrix components result in far poorer limits of detection on the same films for a low mass compound such as histidine (155 Da). In positive ion mode sample concentration below 250  $\mu\text{M}$  could not be detected, while 20  $\mu\text{M}$  was detectable in negative ion mode with a high background signal, comparable to performance reported for histidine on etched porous silicon.[200] Background chemical noise, arising from adsorption of atmospheric ambient chemical contamination could be eliminated by UV-ozone treatment above  $\sim 400$  Da,[119, 205] but at lower mass ranges the treatment simply rearranged the mass distribution without improving LOQ. Since many metabolite biomarkers are present in the 20  $\mu\text{M}$  range or lower, and quantitative work requires better precision than found near the LOQ, it is important to reduce the background chemical noise in this mass range.

Siuzdak and coworkers showed that per-fluoro-chlorosilane coatings could be used with etched porous silicon and a high quality mass spectrometer to give a zeptomole detection limit for des-Arg<sup>9</sup>-bradykinin.[125] It was proposed the coating facilitates adsorption of analytes on the surface for pre-concentration, and that the hydrophobic character of the surface prevents droplet spreading, thus concentrating the dried sample in a smaller spot. It is also clear from their data that the coating greatly reduces background noise, making perfluoro coatings an excellent candidate to improve low mass detection limits on GLAD films.

Modification of Si-GLAD films with a 1% concentration of (per-fluorooctyl) trichlorosilane ( $\text{pFSiCl}_3$ ) yields a super-hydrophobic surface. Aqueous samples have to be

mixed with methanol to spot them on the surface from a pipet tip; a 50/50 mixture gives a contact angle of  $\sim 112^\circ$  and a droplet size of  $\sim 2$  mm. High quality mass spectra can be obtained in negative ion mode from 1-200  $\mu\text{M}$  analytical concentrations for histidine with these coatings, as shown for 1, 2 and 10  $\mu\text{M}$  in Figure 3-1. (Analytical concentrations are the concentration of sample before dilution with any additional reagents such as methanol.) The LOQ for pure samples of asparagine, glutamine and histidine in negative ion mode were 470, 340, and 340 fmol, or 0.6, 0.4 and 0.4  $\mu\text{M}$ , correspondingly, extrapolated from S/N versus concentration plots that show very high linearity ( $R^2 > 0.99$ ). Positive ion mode was not applied to amino acid analysis due to a dominant interference peak at  $m/z$  130.0 which suppresses the signals of amino acids. Coated surfaces showed no change in LOQ or background chemical noise in the low mass range over 7 days of atmospheric exposure. Direct calibration curves are subject to considerable ionization suppression at higher concentrations, so use of an internal standard is required. Selecting 10  $\mu\text{M}$  asparagine as an internal standard, linear calibration curves using peak height ratios were obtained for glutamine ( $R^2 = 0.99$ ) and histidine ( $R^2 = 0.98$ ) samples in the range of 0.5 to 50  $\mu\text{M}$ . LOQ were  $\sim 0.1$   $\mu\text{M}$  with 0.8  $\mu\text{L}$  sample spot delivery.

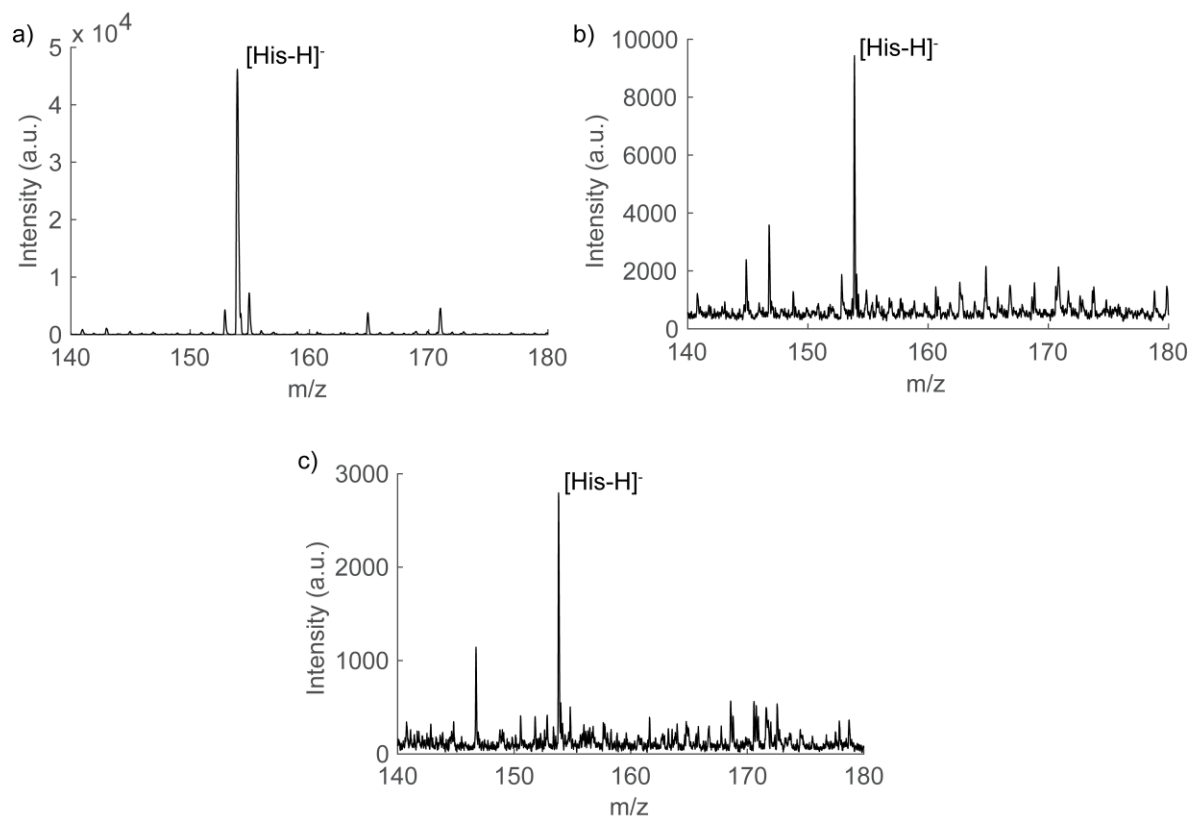


Figure 3-1: Mass spectra of a) 10 b) 2 and c) 1  $\mu\text{M}$  pure histidine solution obtained on a 1% concentration  $\text{pFSiCl}_3$  SMALDI chip.

The results obtained with SMALDI on  $\text{pFSiCl}_3$  coatings show a very high performance level can be achieved for small molecules using the perfluoro coating when the samples are relatively pure, as they may be in the study of synthetic samples, drug purity evaluations, etc.

### 3.3.2 Segregation of salt interferences on perfluoro surfaces

Cerebral spinal fluid (CSF) has been shown to provide a fingerprint of metabolites, including several amino acids,[204, 206] whose concentration changes indicate pAD. A

common artificial CSF composition consists of a mixture of salts (Table 3-1), with 150 mM NaCl dominant, and was used in this study. Salt reduces the quality of the SMALDI data notably on the pFSiCl<sub>3</sub> coated surface (prepared at 1% concentration), as illustrated in Figure 3-2, where depositing a 50/50 methanol/sample mixture yielded salts crystallized over the entire spot surface, significantly masking the GLAD film underneath, and reducing signal strength. For 20 μM histidine the S/N ratio observed was 18 ± 4, and even at 50 μM ~ 30% of the laser shots gave zero signal. The negative impact of salt on LDI from Si substrates has been frequently reported.[108, 125, 201] By using internal standards (IS), and diluting the original aCSF sample to 16.7 % of its analytical concentration, as described in the Experimental section, the salt problem was partially alleviated. The analytical concentration that could be reliably detected was in the range of 10-100 μM, yet calibration errors increased compared to salt free aqueous/methanol samples ( $R^2 = 0.96$ ). More directly, the standard error in using these calibration curves to interpolate the concentration of an unknown in the central region of the curves is ~24%, obviously increasing at the extremes of the calibration range. The concentration change of histidine in pAD is about 22%, and other FAA have smaller percentage concentration changes.[204]

The alternative of rinsing these surfaces following drying of the sample spot showed the amino acids were as poorly retained as the background electrolyte. Desalting the aCSF samples with strong cation exchange ZipTips was not effective; only >1 mM histidine in aCSF was detectable by SMALDI-MS, and glutamine was not observed at any concentration. The similarity of retention of electrolytes and amino acids mean that chromatographic methods are the most effective means of sample preparation, in general.

We found that by reducing the deposition concentration of pFSiCl<sub>3</sub> to 0.3 %, the surface contact angle was reduced, eliminating the need to dilute with methanol, and that higher quality SMALDI data could be obtained for aCSF samples. Further improvement was achieved by drying the sample droplets slowly (several hours) in a closed chamber at 4 °C. Figure 2d shows that on a surface with a 120° aqueous contact angle, several large, localized salt crystals form, leaving much of the SMALDI surface with no visible salt deposit, Figure 2e. High quality MS measurements were obtained from regions without visible crystals, as shown by Figure 2f.

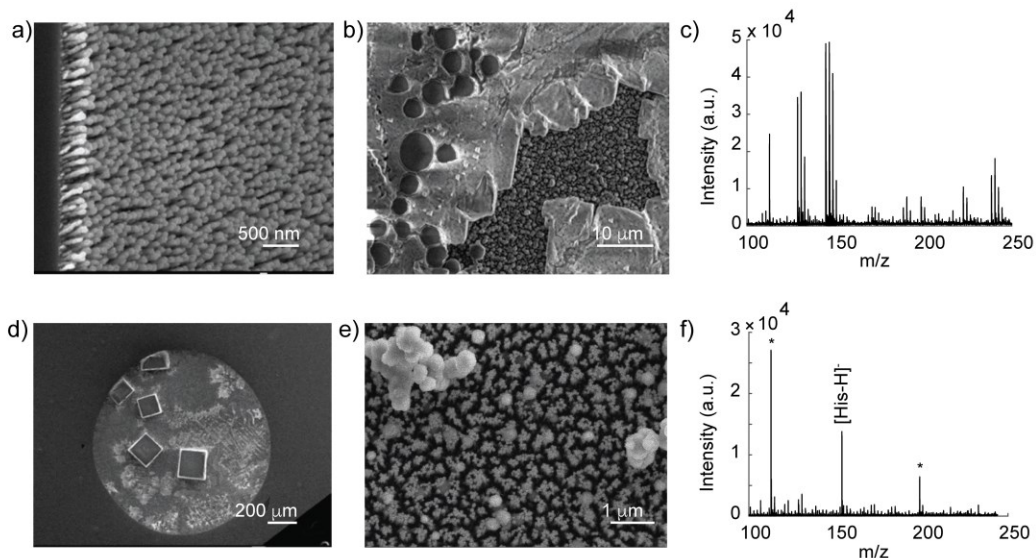


Figure 3-2: a) The nanostructured Si thin films fabricated using GLAD, wherein silicon is evaporated and deposited at an incidence angle of  $86^\circ$  onto silicon wafers, forming vertical nanocolumns. In b) and c), artificial cerebral spinal fluid (aCSF) was deposited on a pFSiCl<sub>3</sub> coated SMALDI chip (1% pFSiCl<sub>3</sub> coating concentration). Salt in the aCSF formed a thick layer, masking the nanoporous structure. (See Appendix F for the SEM image showing the entire sample spot.) 10  $\mu$ M histidine spiked in aCSF was not ionized and detected by SMALDI-MS. In d-f), the same sample was deposited on a pFSiCl<sub>3</sub> surface (pFSiCl<sub>3</sub> coated at 0.3% concentration to give a  $120^\circ$  contact angle) and slowly dried at  $4^\circ\text{C}$  in a closed chamber. After slow air-drying, the background electrolyte formed large crystals. Many of the nanopores are salt-free, in contrast to the salt deposits in b). The MS measurements were taken in regions without visible crystals. The interference from salt was greatly reduced. The [His-H]<sup>+</sup> peak at m/z 154.0 was detected. The asterisks mark background peaks at m/z 112.9 and 199.9.

While optimizing the deposition concentration of the pFSiCl<sub>3</sub> coating, we found that the primary indicator of success was obtaining an average contact angle in the range of  $\sim 105 - 120^\circ$ . These contact angles are indicative of a lower quality film, with defects in the coverage of the silica surface functionality on the columnar structure. Shifting to the monochloro derivative (per-fluorooctyl)dimethylchlorosilane (pFMe<sub>2</sub>SiCl) from pFSiCl<sub>3</sub> made it far easier to obtain contact angles of  $120^\circ$  as a function of coating concentration and reaction time, when testing with a 2  $\mu$ L aCSF droplet. The results for both coating

materials are shown in Figure 3-3, evaluated for aCSF samples. Figure 3-3a shows the S/N is highest, with the least variance in S/N, for coatings in the range of 105-120° contact angle, while S/N is very poor at the highest contact angles. Contact angles in the range of 120-135° are difficult to predictably achieve, and tend to either work effectively or not work at all, resulting in the large variance in S/N for this contact angle range. Contact angles were manipulated by varying the concentration of either pFMe<sub>2</sub>SiCl or pFSiCl<sub>3</sub>, as indicated in Figure 3-3b. Concentration values that gave large standard deviations in contact angle represent the critical concentrations at which the state of the surface between hydrophilic, hydrophobic or superhydrophobic is difficult to control. Concentrations giving low standard deviation in the contact angle are far more attractive to use, since the intended contact angle is much more readily achieved at these concentrations. Figure 3-3c presents the data in an alternate format that emphasizes the relationship between signal, noise and coating concentration, and suggests decrease of S/N at high coating concentration is due to loss of signal.

We also noted that the age of the GLAD film prior to coating was a significant factor. Surfaces that were coated on the day the film was fabricated showed higher contact angles for a given coating concentration. It was far easier to achieve the apparently optimal contact angle (105-120°) across a broad range of coating concentrations for surfaces at least briefly stored under ambient conditions. The shaded box in Figure 3-3b highlights conditions that provide the optimal performance for the various surfaces tested. We conclude that SMALDI chips stored in ambient conditions for a week or longer, then coated with a 1.2% concentration of pFMe<sub>2</sub>SiCl will routinely result in formation of large

salt crystals and give highly reproducible desalting performance, as determined by the S/N ratio for histidine in aCSF samples.

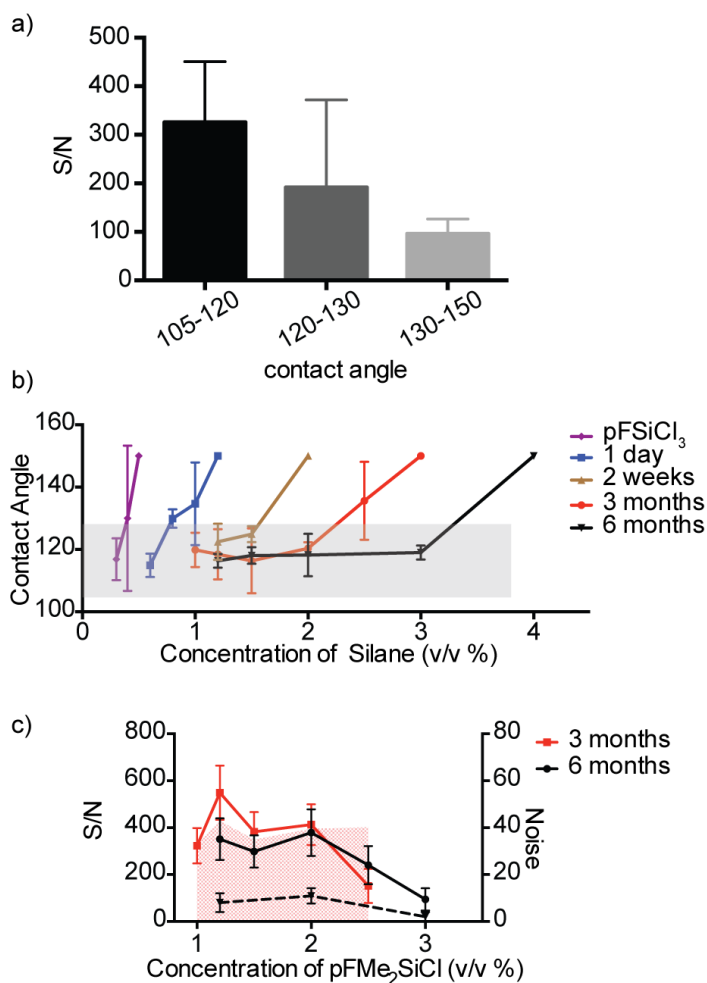


Figure 3-3: a) S/N of 10  $\mu$ M histidine spiked in aCSF on perfluoro coated SALDI surfaces with different contact angles. b) The contact angles on fluorinated SALDI surfaces, controlled by varying the silane, the silane coating concentration and the storage times of GLAD films (1 day – 6 months). The leftmost line is for pFSiCl<sub>3</sub> coatings on a 3-month old surface; the other lines are for pFMe<sub>2</sub>SiCl coatings, differentiated by GLAD film storage times before surface modification. The error bar in b) is SD of 9 individual measurements. c) The relationship between S/N (lines), noise (shadow) and coating concentration. Red represents the 3-month old film and black represents the 6-month old film. The samples were dried in humid chamber at 4°C (solid lines) or room temperature (dash line), and the duration times of drying are  $\sim$ 5 h and  $\sim$ 1 h, respectively. Slow air drying amplifies the desalting performance, and could consistently be associated with the appearance of a few large salt crystals. Referring to b), the S/N significantly decreases on superhydrophobic surfaces, independent of film age and drying time.

With the on-chip desalting, the linear response of a S/N versus concentration plot for histidine in aCSF extends from 1 to 100  $\mu\text{M}$  ( $R^2 = 0.99$ ). The S/N at 1  $\mu\text{M}$  is  $29 \pm 16$ ; considerably better performance than seen on the 1% concentration pFSiCl<sub>3</sub> coated surface, which did not allow for the salt segregation technique. Figure 3-4 shows that a mix of 20  $\mu\text{M}$  amino acids (Leu, Gln, His and Tyr) can be readily determined simultaneously in an aCSF matrix, when using the salt segregation process.

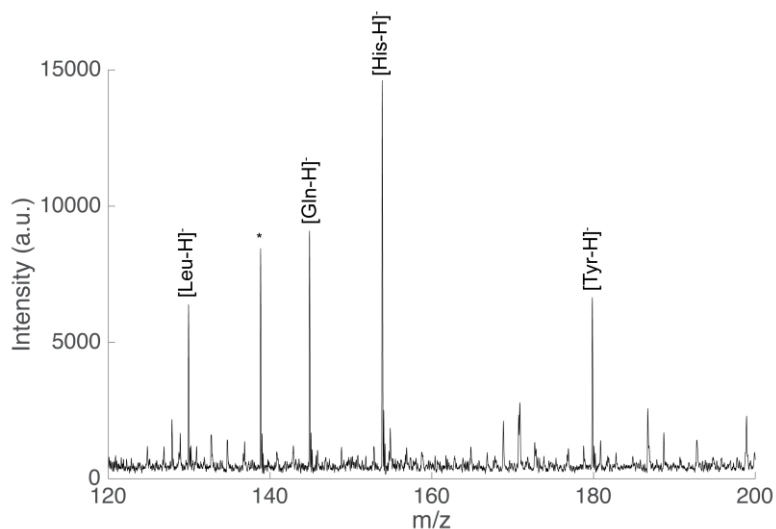


Figure 3-4: A mass spectrum of aCSF sample containing leucine, glutamine, histidine, and tyrosine, 20  $\mu\text{M}$  for each, obtained on 0.3% concentration pFSiCl<sub>3</sub> SMALDI chip with slow air drying.

Using asparagine spiked at 20  $\mu\text{M}$  as IS, the calibration curve for histidine in aCSF shows good linear response from 2 to 50  $\mu\text{M}$ , with improved  $R^2$  values of 0.99, as shown in Figure 3-5. Using 1-methylhistidine spiked at 50  $\mu\text{M}$  as IS, the calibration curve for histidine gave a linear range from 1-100  $\mu\text{M}$ . Using glutamine for the IS gave a good

curve with  $R^2$  of 0.98 from 2 to 50  $\mu\text{M}$ . The error for interpolation of an unknown across the full range of these calibration curves varies from 14 % at the extremes to 1 % in the centre of the curve, making desalting segregation on SMALDI a good tool to detect FAA concentration changes for early diagnosis of pAD. Clearly, a variety of IS choices may be made, giving flexibility in quantitative measurement of multiple components.

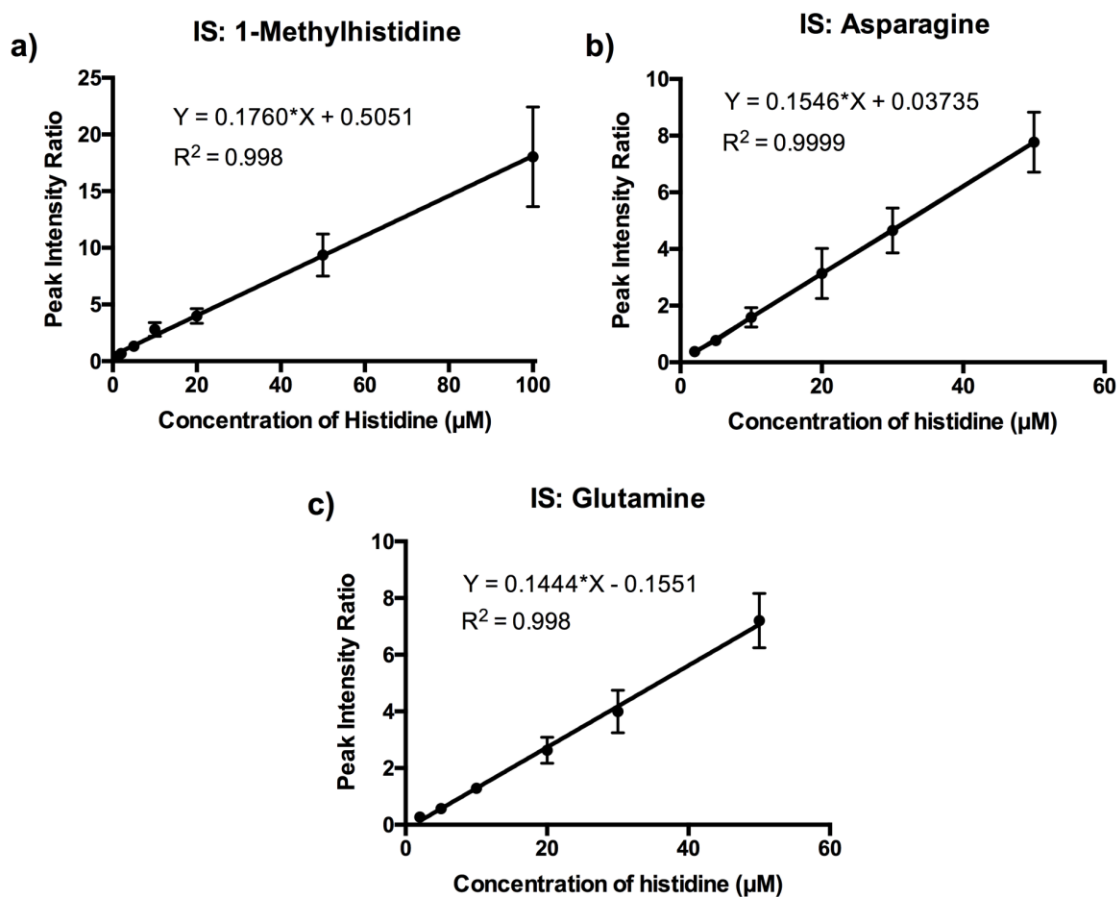


Figure 3-5: The internal standard calibration curves of histidine in aCSF using 20  $\mu\text{M}$  a) 1-methylhistidine, b) glutamine and c) asparagine as internal standards. The linearity ranges are 1-100  $\mu\text{M}$  in a) and 2-50  $\mu\text{M}$  in b) and c). The error bar represents SD of 10 individual measurements.

### **3.4 Conclusions**

Perfluoro-coatings on GLAD films have been shown to have greatly reduced background chemical noise in the low mass range relevant to small biomarkers, allowing accurate measurements to be made of relatively clean samples. Through the generation of a coated, nano-structured surface with a controlled extent of defects, as evidenced by contact angle measurements, we have developed a method to desalt the sample matrix during slow air drying. Coating defects generated in the surface modification encourage segregated crystallization of the dominant salt content from the analyte ions. Combining with the on-chip desalting, precisions of SMALDI-MS are improved in quantitative analysis of salty samples.

## CHAPTER 4 SERUM METABOLITE ANALYSIS BY SMALDI-MS <sup>3</sup>

### 4.1 Introduction

Biofluid metabolites are end-products of genome driven cellular processes and serve as an excellent probe to phenotype.[207-209] Fingerprinting biofluid metabolites by mass spectrometry (MS) has become a main approach in quantifying phenotypes,[144, 210] but it requires the ability to reduce sample matrix interference prior to MS analysis.[168, 211] Liquid chromatography and electrospray MS (LC-MS) is a standard and powerful tool in metabolite fingerprinting,[212, 213] partially due to convenient on-line sample preparation by the LC. As an alternative, fluorinated porous silicon laser desorption ionization (pSi-LDI) offers remarkably high sensitivity in detecting small molecules, and its application in biofluid metabolite analysis has been explored.[125, 137, 214] Even though pSi-LDI requires minimal sample preparation, it is crucial that samples be prepared in a way to greatly reduce the challenges associated with a complex sample matrix.[108] On-chip, porous Si methods take advantage of hydrophobic interactions between metabolites and the fluorocarbon coatings, for less polar and higher mass analytes. Differential adsorption can be carried out through repetitive pipetting of the sample solution on and off the surface, a process named “z-touch”. [108, 125, 142] However, for low mass ionic metabolites, such as amino acids in serum, derivatization of the analytes is needed to enhance extraction onto the coated LDI substrate, so as to retain the analytes when other

---

<sup>3</sup> Part of this chapter has been submitted for publication to Analytical Chemistry. The NMR analysis was done by co-author Rupasri Mandal.

matrix components are removed by rinsing.[125, 141] When more sophisticated sample preparation steps have to be involved to improve performance, the advantages of pSi-LDI as an easy-to-operate tool for biofluid metabolite analysis are reduced and its suitability for quantitative analysis is in doubt.

We presented a coating and a procedure for SMALDI for on-chip desalting in Chapter 3. Here, we apply the SMALDI chips and the desalting process to serum metabolite analysis. We demonstrate that SMALDI, as a direct-infusion MS technique, without any chromatographic separation, can achieve biofluid metabolite quantitation with a simple spot test.

## **4.2 Experimental section**

### **4.2.1 SMALDI chip preparation**

The film fabrication and surface modification procedures are described in Chapter 3. The silane solution used in surface modification was a 1.2 v/v% methanol solution of (1H, 1H, 2H, 2H-perfluorooctyl) dimethylchlorosilane (pFMe<sub>2</sub>SiCl, Gelest, PA).

### **4.2.2 Serum sample preparation**

Human serum (pooled normal, Innovative Research, MI) was thawed on ice, then deproteinized through ultrafiltration. Centrifugal filter units (EmdMillipore, Amicon Ultra-4, 3K molecular weight cut-off) were pre-rinsed to remove glycerol bound to the ultrafiltration membranes. 4 mL of deionized water was added to each centrifugal filter

unit, followed by a 10-minute spin at 4,000 g with a swinging bucket rotor (Beckman Coulter, Allegra X-22). The serum sample was then transferred into the rinsed centrifugal filter units and spun at 4,000 g and 4 °C for 30 min. The downstream filtrate was collected and acidified by HCl at 0.2 M to denature any remaining protein and acidic lipids. Then, the samples in 1.5 µL aliquots were spotted on 1.2 % pFMe<sub>2</sub>SiCl fluorinated SMALDI chips with contact angles of 110-120° and dried in a small petri dish (Fisherbrand, 35 mm x 10 mm) at 4 °C to complete sample cleanup.

#### **4.2.3 Quantitative analysis by MS and NMR**

The parameter settings on the AB Sciex mass spectrometer are the same as described in Chapter 3, except that the laser intensities in positive ion mode are 1900, 2000 and 2100 a.u. at m/z 50-110, 110-300, and 300-1000, respectively. The metabolites in serum were quantified by SMALDI-MS using the standard addition method. Six centrifugal filter units were pre-rinsed and each was filled with 0.5 mL serum. Then various volumes of standard solutions of metabolite (taurine, histidine, aspartic acid, glutamic acid and malic acid) were spiked in serum samples. The mixture was diluted to a total volume of 1 mL and thoroughly mixed before ultrafiltration.

As a comparison, the concentrations of the serum metabolites quantified by SMALDI-MS were also quantified by <sup>1</sup>H-NMR spectroscopy. The ultrafiltration step was used in the NMR sample preparation as well. Subsequently, 70 µl of D<sub>2</sub>O and 30 µl of a standard buffer solution (11.7 mM sodium 2,2-dimethyl-2-silapentane-5-sulfonate, 730 mM

imidazole, and 0.47% NaN<sub>3</sub> in H<sub>2</sub>O) was added to 600 µl serum filtrate. The sample (700 µL) was then transferred to a standard NMR tube for spectral analysis. All <sup>1</sup>H-NMR spectra were collected on a 500 MHz Inova spectrometer (Varian Inc.) equipped with a 5 mm HCN Z-gradient pulsed-field gradient room-temperature probe. <sup>1</sup>H-NMR spectra were acquired at 25°C using the first transient of the NOESY-pre-saturation pulse sequence, chosen for its high degree of quantitative accuracy. All free induction decays were zero-filled to 64 K data points and subjected to line broadening of 0.5 Hz. The singlet produced by the DSS methyl groups was used as an internal standard for chemical shift referencing (set to 0 ppm) and for quantification. All <sup>1</sup>H-NMR spectra were processed and analyzed using the Chenomx NMR Suite Professional Software package version 7.1 (Chenomx Inc). The spectral fitting for metabolites was done using the standard Chenomx 500 MHz metabolite library. We used sample spiking to confirm the identities of assigned compound. Sample spiking involves the addition of 20-200 µM of the suspected compound and examination of the resulting spectra to determine whether the relative NMR signal intensity changed as expected.

## **4.3 Results and discussion**

### **4.3.1 Serum sample analysis**

The workflow of biofluid metabolite analysis by SMALDI-MS is illustrated in Figure 4-1. The serum samples were deproteinized with ultrafiltration. The filtrates were acidified by HCl at 0.2 M and spotted on SMALDI chips for sample cleanup and MS analysis. We found it is essential to thoroughly remove proteins to effect salt segregation on coated SMALDI surface. Serum proteins over 6 kDa can be removed by ultrafiltration using a 3

kDa molecular weight cut-off membrane. Small proteins were subsequently denatured by HCl at a concentration  $> 0.05$  M. By then acidifying serum filtrate with 0.2 M HCl, salt in the serum segregated as the sample was slowly dried, and many of the nanopores were left salt-free (Fig. 4-3a and 4-3b), similar to the results observed for aCSF samples. Without these preparation steps, the dried sample spots mask nanoporous structure and impede desorption ionization (Figure 4-2). Quantitation of each serum metabolite was performed on the same batch of SMALDI chips. Figure 4-3d and 4-3e show the mass spectra of the human serum in low mass range. Peaks with  $m/z$  over 300 in negative ion mode and peaks with  $m/z$  over 1000 in positive mode were not observed.

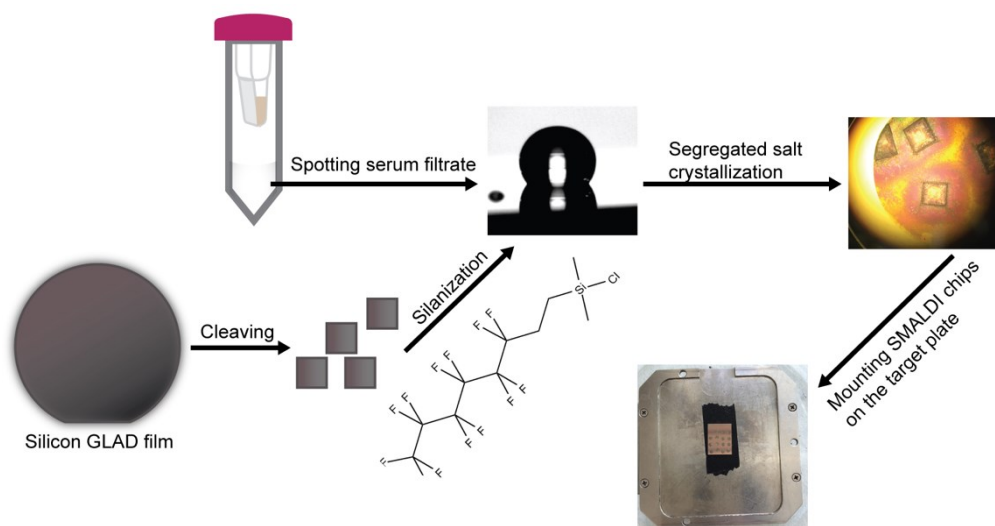


Figure 4-1: Workflow for biofluid sample analysis by SMALDI, including silicon GLAD film surface silanization, deproteinization by ultrafiltration, on-chip desalting through segregated salt crystallization and SMALDI-MS acquisition.

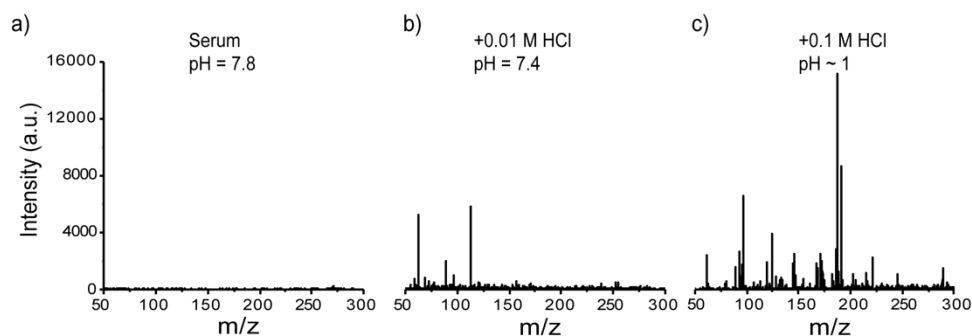


Figure 4-2: SMALDI-MS spectra of human serum. The serum samples were deproteinized through ultrafiltration, and then acidified in b) and c) by adding HCl. The samples were desalted on 1.2 % pFMe<sub>2</sub>SiCl coated SMALDI chips during slow air drying.

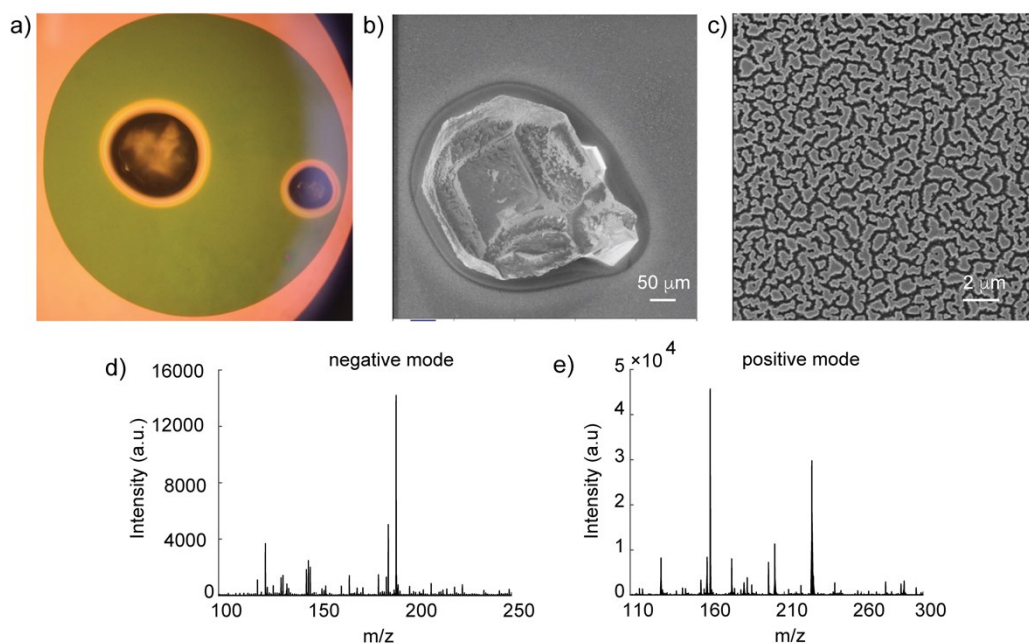


Figure 4-3: SMALDI-MS for the analysis of metabolites in human serum. The deproteinated serum was spotted on a pFMe<sub>2</sub>SiCl SMALDI coated chip (1.2% coating concentration) and slowly air dried. The salt in the sample aggregated in a small region of the dried sample spot, as observed under a) optical and b) helium ion microscope. c) shows the nanopores are salt free after the sample deposition, but there is some nanocolumn clumping. The MS measurements in d) and e) were taken in regions without visible crystals, obtained in negative and positive ion modes, respectively. The mass spectra of serum metabolites in the low mass range are assigned in accompanying tables.

Five putative metabolites in the serum samples, taurine, aspartic acid, malic acid, glutamic acid and histidine, ionized in the form of  $[M-H]^-$ , were identified and quantified using a standard addition method (Figure 4-4). The coefficients of variation (CVs) of all five metabolites were below 30%. The results are summarized in Table 4-1 and compared with the normally observed concentrations in blood, along with results from NMR spectroscopy on commercial serum samples. The concentrations of taurine, malic acid and histidine observed by SMALDI are within the physiological ranges. The concentrations of aspartic acid and glutamic acid are out of the normal ranges, but consistent with the NMR results, indicating the two metabolites are abundant in the commercial serum sample. Malic acid and taurine are not quantifiable by NMR. Combined with on chip desalting, the SMALDI chip works in a similar concentration range as NMR for quantitative analysis of serum metabolites, but detects and quantifies a complementary list of metabolites. The method is easy to apply in terms of sample preparation and offers rapid batch analysis of multiple metabolites.

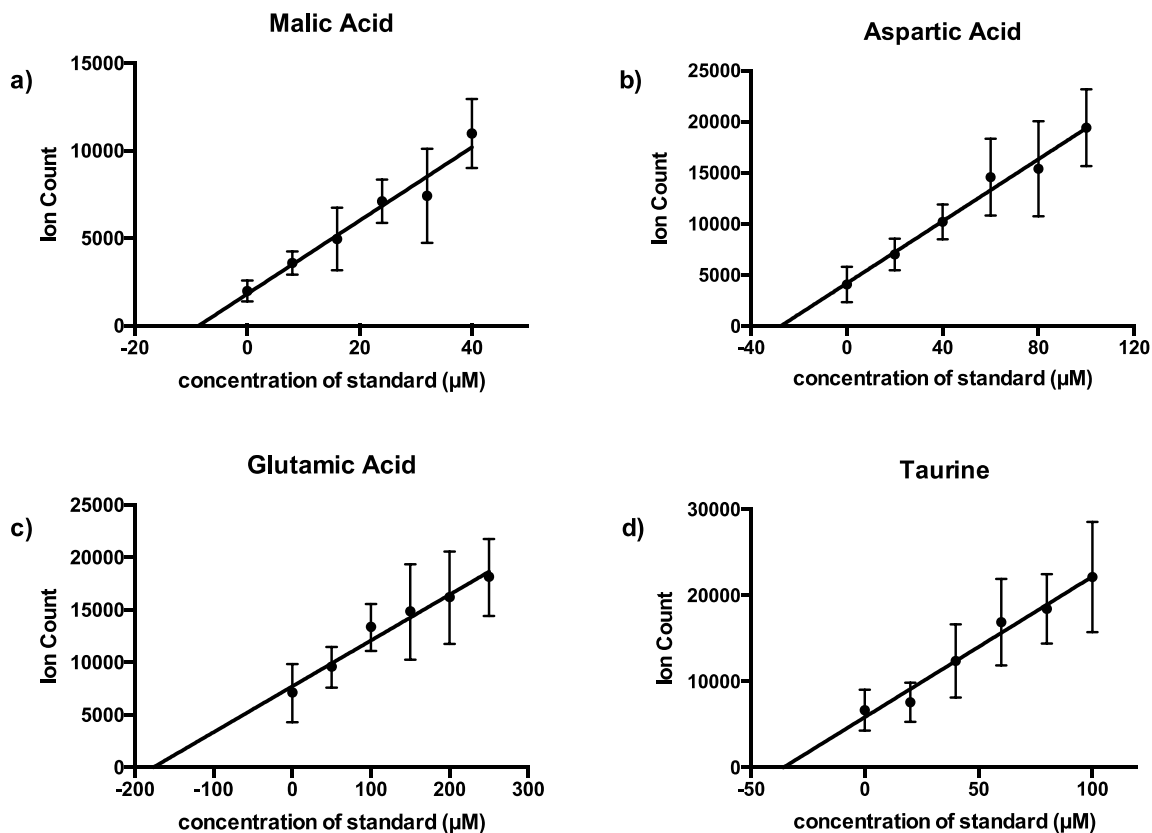


Figure 4-4: The standard addition curves of a) malic acid, b) aspartic acid, c) glutamic acid and d) taurine in human serum. SMALDI chips were coated with a 1.2% concentration of pFMe<sub>2</sub>SiCl, 120° contact angle. Before deproteinization by ultrafiltration, 0.5 ml serum was mixed with standard solution and subsequently diluted to 1 ml. The x-axis in a-d) represents the final concentration of the standard in the 1 ml mixture. Therefore, the readings at y=0 represents half of the analyte concentrations in the serum sample. The error bar is the SD of 9 individual measurements.

Table 4-1: The concentrations of metabolites in human serum quantified by SMALDI-MS and NMR, compared with the normal concentrations in blood.

| <b>Metabolite</b> | <b>MW (Da)</b> | <b>SMALDI-TOF-MS<br/>(<math>\mu\text{M}</math>)</b> | <b>DATA BASE*<br/>(<math>\mu\text{M}</math>)</b> | <b>NMR<br/>(<math>\mu\text{M}</math>)</b> |
|-------------------|----------------|---|--|---|
| Taurine           | 125.01         | 72  | 45-130   | N/A                                       |
| Aspartic Acid     | 133.04         | 55.3  | <25  | 62.7                                      |
| Malic Acid        | 134.02         | 17.3  | 12.0 (0.0-21.0)                                  | N/A                                       |
| Glutamic Acid     | 147.05         | 353.2   | <100   | 261.5                                     |
| Histidine         | 155.07         | 85.7  | 26-120   | 114.0                                     |

\*Data are from Human Metabolome database (HMDB, [www.hmdb.ca](http://www.hmdb.ca)).

The TOF mass analyzer we employed offers a mass accuracy of  $\pm 0.2$  Da below  $m/z$  3500, so using  $m/z$  as the only observable makes unequivocal identification of the many compounds observed difficult. Nevertheless, we evaluated the reproducibility of the MS results obtained on 8 desalted serum sample spots. Figure 4-5 shows the coefficients of variation (CV) of signal intensities for the strong peaks at  $m/z$  100-250 detected in negative ion mode, and for the strong peaks at  $m/z$  110-300 detected in positive ion mode. Excluding peaks with S/N less than 20, there were 36 and 34 peaks detected in negative and positive ion modes, respectively. The CVs of the peaks are mainly in the 20-40% range, comparable to the range seen using other MS techniques in metabolite profiling.[215, 216] Negative ion peaks were assigned to metabolites using the Human Metabolome Database (HMDB, [www.hmdb.ca](http://www.hmdb.ca)), assuming the adduct is  $[\text{M}-\text{H}]^-$ . The molecular weight tolerance was  $\pm 0.1$  Da, and only metabolites known to be found in blood were considered. Table 4-2 shows that 32 of 35 peaks observed could be assigned, and most of these putative species were compounds with carboxyl functionality. The good reproducibility of the spot

tests on SMALDI demonstrates its potential in clinical applications and suggests it can be readily coupled with MS/MS for identification of serum metabolites.

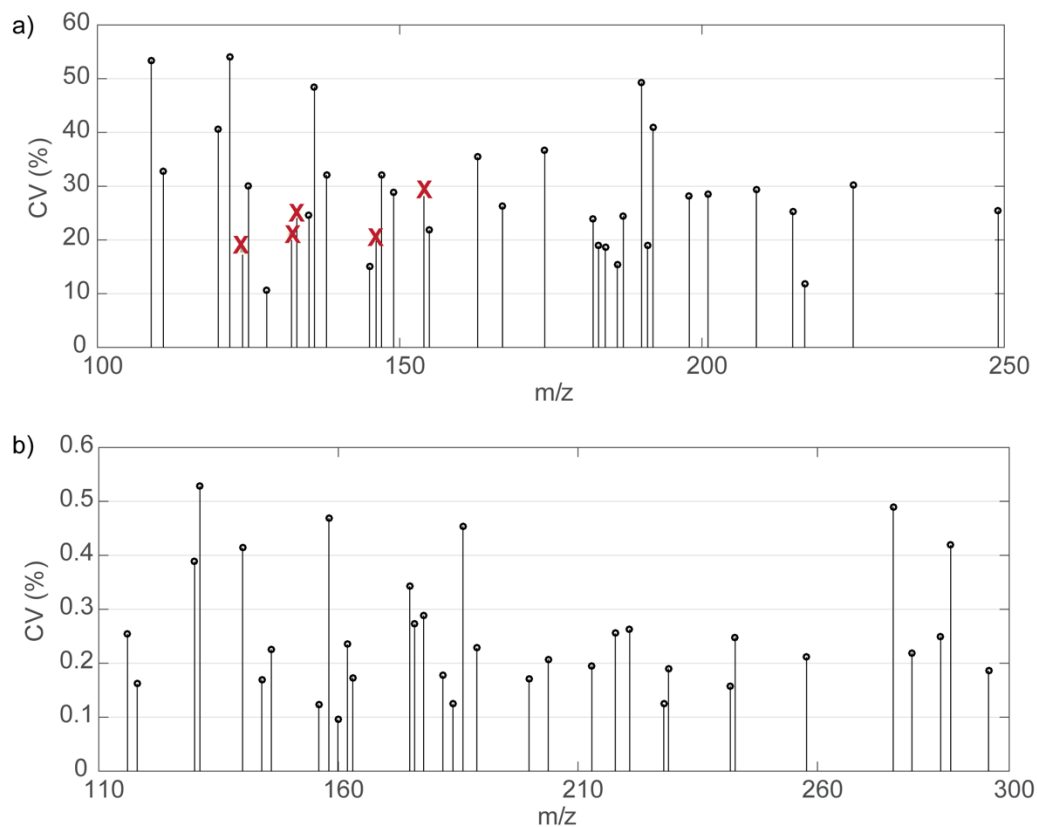


Figure 4-5: The coefficients of variation (CVs) of the peak heights at a) m/z 100-250 (negative ion mode) and b) m/z 110-300 (positive ion mode). The CVs were calculated from mass spectra of 8 serum sample spots on SMALDI chips. Excluding the peaks with S/N less than 20, 36 and 34 peaks were detected in negative mode. Red Xs in a) represent the five quantified metabolites in Table 4-1.

Table 4-2: The putative metabolites for peaks detected in human serum in negative ion mode by SMALDI-MS

| Observed m/z | Assigned metabolite*   | Adduct MW (Da) | $\Delta$ m/z | CV (%) |
|--------------|--|----------------|--------------|--------|
| 108.8923     | N/A  |                |              | 53.40  |
| 110.8816     | Thiosulfate  | 110.9216       | 0.0400       | 32.73  |
| 119.9362     | Cysteine   | 120.0125       | 0.0763       | 40.64  |
| 121.9334     | Isonicotinic acid/ Nicotinic acid/ Picolinic acid  | 122.0248       | 0.0914       | 53.96  |
| 124.0001     | Taurine  | 124.0074       | 0.0073       | 18.06  |
| 128.0315     | Pyroglutamic acid  | 128.0353       | 0.0038       | 10.58  |
| 132.0302     | Aspartic acid  | 132.0302       | 0            | 20.9   |
| 133.0057     | Malic acid   | 133.0142       | 0.0085       | 24.99  |
| 135.0202     | Erythronic acid/ Threonic acid   | 135.0299       | 0.0097       | 24.54  |
| 135.9220     | N/A  |                |              | 48.50  |
| 137.9042     | N/A  |                |              | 32.11  |
| 145.0376     | Adipic acid/ Methylglutaric acid/ 2-Methylglutaric acid  | 145.0506       | 0.0160       | 15.07  |
| 146.0439     | Glutamic acid  | 146.0459       | 0.0020       | 20.74  |
| 146.9736     | 2-Hydroxyglutaric acid/ 3-Hydroxyglutaric acid/ Citramalic acid  | 147.0299       | 0.0563       | 32.11  |
| 148.9814     | 4-Ethylbenzoic acid/ Hydrocinnamic acid  | 149.0608       | 0.0794       | 28.78  |
| 154.0698     | Histidine  | 154.0622       | 0.0076       | 29.10  |
| 154.9306     | 2,5-Furandicarboxylic acid   | 154.9986       | 0.0680       | 21.91  |
| 162.9517     | Coumaric acid/ 4-Hydroxycinnamic acid/ Phenylpyruvic acid/ 2-Oxo-3-phenylpropanoic acid  | 163.0401       | 0.0884       | 35.44  |
| 167.0301     | Homogentisic acid/ Vanillic acid/ 3-Hydroxymandelic acid/ p-Hydroxymandelic acid/ 5-Methoxysalicylic acid/ 3,4-Dihydroxybenzeneacetic acid | 167.0350       | 0.0050       | 26.28  |
| 174.0042     | N-Acetyl-L-aspartic acid   | 174.0408       | 0.0366       | 36.65  |
| 181.9689     | 4-Pyridoxic acid   | 182.0459       | 0.0770       | 23.91  |
| 182.9579     | 4-O-Methylgallic acid/ 3,4-Dihydroxymandelic acid  | 183.0299       | 0.0720       | 18.93  |
| 183.9653     | Phosphoserine  | 184.0016       | 0.0363       | 18.58  |
| 185.9969     | N/A  |                |              | 15.48  |
| 187.0194     | Azelaic acid   | 187.0976       | 0.0782       | 24.50  |

|          |   |          |        |       |
|----------|---|----------|--------|-------|
| 189.9928 | 5-Hydroxyindoleacetic acid                          | 190.0510 | 0.0582 | 49.34 |
| 191.0197 | Citric acid/ Isocitric acid                         | 191.0197 | 0      | 18.94 |
| 192.0240 | 4-Anilino-4-oxobutanoic acid/ 2-Methylhippuric acid | 192.0666 | 0.0426 | 40.88 |
| 197.9291 | O-Phosphothreonine                                  | 198.0173 | 0.0882 | 28.18 |
| 201.0420 | Sebacic acid  | 201.1132 | 0.0712 | 28.57 |
| 208.9871 | N/A   |          |        | 29.37 |
| 215.0313 | Bisnorbiotin/ 6-Aminopenicillanic acid              | 215.0496 | 0.0183 | 25.27 |
| 217.0264 | 3-Hydroxysebacic acid/ 2-Hydroxydecanedioic acid    | 217.1081 | 0.0817 | 11.80 |
| 224.9676 | 3-Nitrotyrosine                                     | 225.0517 | 0.0841 | 30.15 |
| 249.0001 | Gamma-Glutamylcysteine                              | 249.0551 | 0.0550 | 25.49 |

\* Peaks were assigned to metabolites using Human Metabolome Database (HMDB, [www.hmdb.ca](http://www.hmdb.ca)). The adduct type is limited to  $[M-H]^-$  which is the most likely ionization form in negative ion mode using pSi-LDI chips. The molecular weight tolerance is  $\pm 0.1$  Da. Aspartic acid and citric acid were used as references for mass calibration, so  $\Delta m/z$  at 132.0 and 191.0 are zero. When assigning possible metabolites to peaks detected, we only considered the metabolites that have been detected in blood. 5 of 37 peaks were not assigned, among which the peak at  $m/z$  186.00 is a known background peak.

#### 4.3.2 SMALDI on Bruker UltrafleXtreme

As discussed above, it is necessary to couple SMALDI with MS/MS for convincing metabolite identification. Here, we present some preliminary efforts in adapting SMALDI chips on UltrafleXtreme and discuss the problems that must be solved in future work to achieve biofluid metabolite identification by SMALDI-MS/MS with the Bruker instrument available to us. We note that previous work by Reshma Singh with a Sciex TOF/TOF successfully resulted in preliminary  $MS^2$  results, however, that instrument had a catastrophic pump failure and became unavailable, leading us to work with the Bruker machine.

UltrafleXtreme is the most advanced MALDI-TOF/TOF mass spectrometer marketed by Bruker Daltonics. It has been used by other research teams together with SALDI surfaces for metabolite imaging, providing high quality MS and MS/MS results.[100, 217] The UltrafleXtreme is equipped with a frequency-tripled Nd:YAG laser (355 nm), whereas a nitrogen laser (337 nm) was applied in previous SMALDI-MS measurements. The Nd:YAG laser offers a higher repetition rate, allowing faster MS data acquisition. It has been demonstrated that the small shift in wavelength does not significantly affect the UV adsorption of both MALDI matrix and porous silicon.[218, 219] However, the focusing of the laser in the Bruker instrument requires preparation of a thin matrix/analyte layer on the target plate.[220]

Even though an organic matrix is not used in SMALDI analysis and electrolytes in biological samples can be isolated on the 1.2% pFMe<sub>2</sub>SiCl coated surface, we found the amount and density of sample still has subtle effects on the performance of SMALDI. High quality mass spectra of 15 pmol histidine were obtained using 1.2 % pFMe<sub>2</sub>SiCl coated SMALDI chips (Figure 4-6a), once a large number of parameters were adjusted, as discussed below. However, higher quantities, such as 300 pmol histidine deposited on the same surface resulted in lower signal intensity and S/N, suggesting some form of saturation of the space charge region where the sample ionizes, the ion optics, or the detector. Dilute amino acid standards, in 1.5  $\mu$ l aliquot, could not be effectively ionized from perfluoro coated SMALDI surface, when a small sample spot (< 0.5 mm) forms. Ionization was achieved when we controlled the diameter of sample spot to obtain 1-2 mm, by using a surface with  $\sim$ 120° contact angle or by mixing organic solvent into aqueous samples.

The optimal instrument settings for the MS measurement are listed in Table 4-3. The parameters that substantially affect the MS results are laser spot size, pulsed ion extraction (PIE) delay time and ion source (IS) voltage 1 and 2. Varying any of them from the Table values results in poor MS results. The focal diameter of the Nd:YAG laser is  $< 10 \mu\text{m}$ , too small for efficient desorption ionization. Therefore, a multi-spot pattern modulated by SmartBeam mode was used to increase the overall laser spot size to “large”.

When the laser beam hits the sample spot, the same voltages (IS1) are applied on both target plate and the second voltage plate (P2, Figure 4-7), which continues for tens of nanoseconds (PIE delay time). During this phase, the SMALDI surface adsorbs laser irradiance and transfers energy to the analytes, which are then desorbed from the SMALDI surface, ionized, and obtain an initial kinetic energy to move toward P2, without being exposed to an electric field. After the PIE delay, the voltage applied on P2 is decreased to IS2 to accelerate the slower ions, so that the ions of the same  $m/z$  but different initial velocity can reach the detector at the same time.

The optimization parameters that work best for PIE delay time, IS1 and IS2 voltages indicate a weak desorption process, possibly caused by insufficient thermal energy transfer from the SMALDI chips to the sample. In our study, the optimized PIE delay time (10-20 ns) is much larger than the reported value (0 ns) for small molecule analysis using pSi with a mass spectrometer of the same series. Considering the PIE delay time for protein analysis is  $\sim 50$  ns, a difference of 20 ns in delay time is relatively significant for small molecule analysis. In addition, the voltage ratio of IS2 to IS1 we have used is the lowest

that can be applied on the instrument. This suggests that most ions (i.e., [His-H]<sup>+</sup>) have a very low initial energy, though a very few of them received high enough energy to move to the second plate without an electric field. Insufficient thermal energy transfer from SMALDI surface to analytes is one of the possible reasons for such a low energy.

The SMALDI might be improved by choosing solid matrix materials which have low thermal conductivity, in which the energy adsorbed from laser irradiation can be transferred to the analytes more efficiently. In the literature, most metabolite profiling by pSi-LDI was done on AB Sciex mass spectrometers. The laser equipped with AB Sciex instruments has been advanced from a nitrogen laser to an on-axis Nd:YAG OptiBeam system, both of which work well with various pSi-LDI surfaces (DIOS, NIMS, NALDI, etc.).[221, 222] Only a few papers report using pSi-LDI on Bruker mass spectrometer for metabolite imaging.[223-225] Difficulties in selecting MS parameters were not noted, but the reported settings did not work for SMALDI. De Laorden et al reported quantitative analysis of lactose in milk using a nanostructured indium tin oxide (ITO) slide on a Bruker UltrafleXtreme.[100] A 87% IS2/IS1 ratio was applied, and high quality mass spectra of metabolite standards were obtained in the range of m/z 100-600. The electrical resistivity of ITO is 0.002 Ω·cm, similar to that of pSi on SMALDI (0.005-0.02 Ω·cm), but the thermal conductivity of ITO (11-12 W/(m·K)) is ~10 times lower than silicon (149 W/(m·K)), consistent with the above assumption that a SALDI surface with lower thermal conductivity may significantly increase its performance on Bruker UltrafleXtreme.

Table 4-3: The optimal instrument settings for SMALDI-MS on UltrafleXtreme (negative ion mode)

|  |             |
|--|-------------|
| Number of laser shots                  | 200         |
| Laser frequency                        | 10          |
| Laser spot size                        | “4-Large”   |
| Laser Intensity                        | 27%         |
| Pulsed ion extraction (PIE) delay time | 10 or 20 ns |
| Ion Source voltage 1 (IS1)             | 20 kV       |
| Ion Source voltage 2 (IS2)             | 15 kV       |
| Lens voltage                           | 6.8 kV      |
| Reflector voltage 1                    | 26.45 kV    |
| Reflector voltage 2                    | 13.45 kV    |

With the acquisition parameters optimized to the extent possible, the UltrafleXtreme accommodated SMALDI surfaces and offered good signal with and low chemical background in detection of metabolite standards (Figure 4-6a). Figure 4-6b shows the mass spectrum of human serum acquired by UltrafleXtreme. The serum sample was deproteinated and desalted following the same protocol described above. Though the baseline is relatively noisy, all the  $m/z$  peaks listed in Table 4-2 were also observed in this mass spectrum.

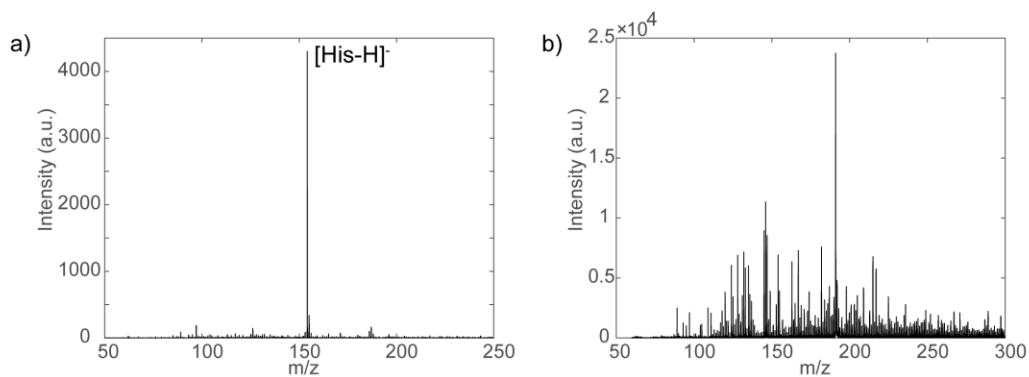


Figure 4-6: Mass spectra of a) 15 pmol (10  $\mu$ M) histidine and b) deproteinated human serum deposited on 1.2 % pFMe<sub>2</sub>SiCl coated SMALDI film, taken in negative ion mode using UltrafleXtreme.

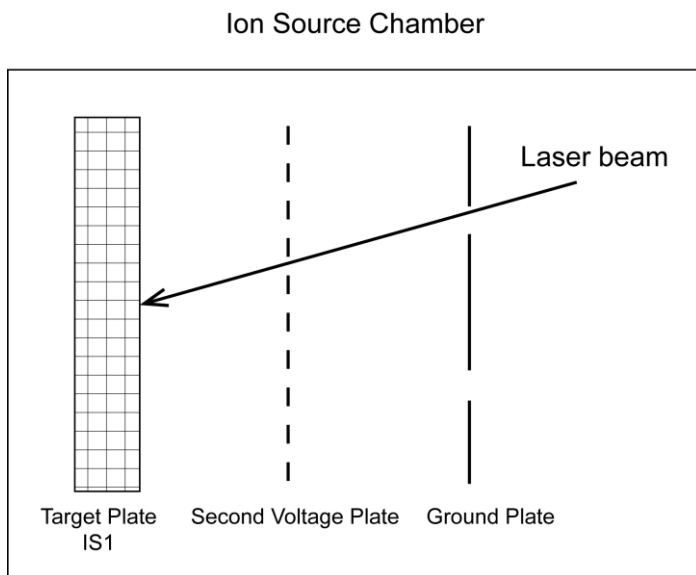


Figure 4-7: Schematic of time-lag ion source.

Our goal here is to identify serum metabolites through MS/MS spectra. However, we have not accomplished this yet, because mass calibration of the Bruker in the TOF/TOF mode are currently far off, leading to difficulties in selecting precursor ions. Figure 4-8 shows MS and MS/MS spectra of  $\alpha$ -cyano-4-hydroxycinnamic acid (CHCA) acquired on the

UltrafleXtreme. CHCA saturated solution (water/acetonitrile, 50/50), in aliquots of 1.5 $\mu$ l, was deposited on 1% pFSiCl<sub>3</sub> coated SMALDI surface and air-dried. In addition to the instrument settings shown in Table 4-3, a 9.8 kV LIFT1 voltage and a 2.3 kV LIFT2 voltage were used in the TOF/TOF mode to accelerate fragments ions. Other parameters are the same as in the TOF mode, except that the PIE delay time was increased to 40 ns. After acquiring high quality MS spectrum of CHCA, we selected m/z 188.0 as the precursor ion ([M-H]<sup>-</sup>) and set the mass tolerance to  $\pm 2$  Da. However, signals were not observed in the MS/MS spectra. Through manually changing the mass range of precursor ion, we obtained an MS/MS spectrum, as shown in Figure 4-8b. Apparently, the mass of precursor ions [M]<sup>-</sup> and [M-H]<sup>-</sup> shifted  $\sim 38$  Da to the left. The peak at m/z 83.7 possibly represents a fragment ion. Therefore, it is not possible to obtain the MS/MS spectra of serum metabolites without calibrating the instrument in the low mass range. However, the calibration system in Bruker mass spectrometers is complex and not isolated for different mass ranges. We were not able to accurately calibrate mass in the low mass range to date, so that more efforts are required to achieve metabolite identification with SMALDI-MS/MS.

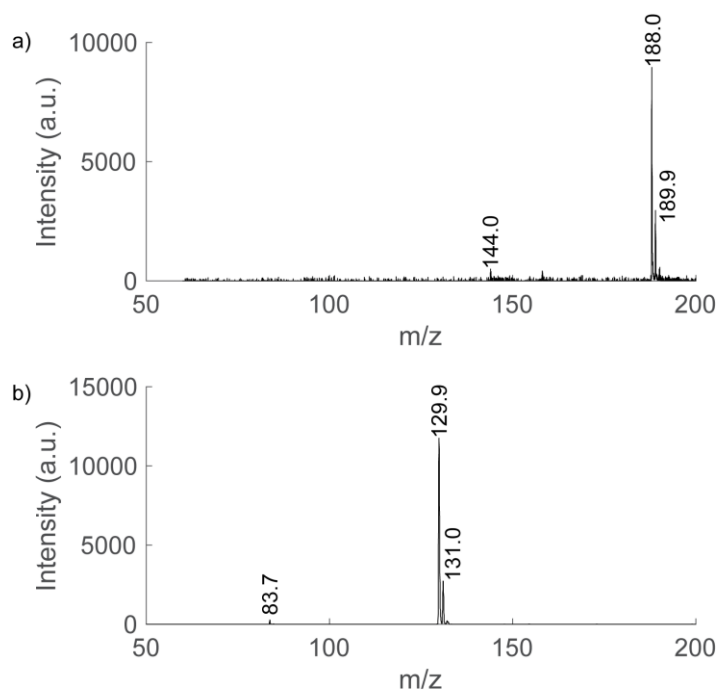


Figure 4-8: a) MS and b) MS/MS spectra of CHCA saturated solution (water/acetonitrile, 50/50) acquired in negative mode. The sample was spotted on 1% pFSiCl<sub>3</sub> coated SMALDI chip. In a), the m/z peaks at 189.9, 188.0 and 144.0 represent [M]<sup>-</sup>, [M-H]<sup>-</sup> and [M-CO<sub>2</sub>H]<sup>-</sup> ions, respectively, consistent with the record on MassBank ([www.massbank.jp](http://www.massbank.jp), Accession: MCH00004).

#### 4.4 Conclusions

Coupled with the perfluoro coating to effect desalting, SMALDI is suitable for the detection and quantification of highly polar metabolites in serum with a simple spot test. SMALDI has potential to detect more than 70 metabolites in serum and offers acceptable reproducibility. However, identification of these metabolites requires SMALDI working with a mass analyzer which offers higher mass precision than TOF or provides structural information for the component of interest.

## **CHAPTER 5 CONCLUDING REMARKS AND FUTURE WORK**

### **5.1 Concluding remarks**

There are two major parts in this thesis: investigating the mechanism of DNA trapping during pulsed field electrophoresis; and biofluid metabolite analysis using porous silicon (pSi) based LDI-MS. Both research topics are related to developing the fundamentals of new approaches to analytical techniques. Nanoporous structures serve as platforms for these studies, simplifying the complexity of the problems and assisting us to achieve the objectives, but, possibly, making less clear the connections between our results and broad research interests.

We investigated the mechanism of DNA trapping in nanoporous structure during pulsed field electrophoresis, using crystalline nanoarrays constructed by self-assembly of crystals of silica particles in a microfluidic device. We found that trapping is primarily caused by the interference from small DEP forces at the apex of hooked molecules, which reduces the mobility of apex segments and cause hernias, confounding the motion of DNA under pulsed fields. The trapping mechanism is strongly evidenced by direct observation of single DNA trapping under a microscope, and the unusual unhooking times of U/J shaped DNA. The companion of DEP phenomenon in DNA electrophoretic separation has always been ignored and never been considered as a cause of trapping. Our work provides a new understanding of the problem in particle based or microbaricated sieve structures. We did not find any reference which estimates the electric field gradient in gels around the fibrous

structures gels formed, although its presence is obvious due to the non-uniformity of the separation media. As a result, it is not clear if our findings in nanoporous structures can be directly projected to trapping in gels, because the magnitude of DEP forces may be different in gels from silica nanoporous structures. It has been demonstrated by other studies that intermittent fields can effectively alleviate trapping in both separation media, suggesting tension on hooked molecules is the primary reason for trapping, rather than hernias, consistent with our results. In addition to the proposed mechanism for DNA trapping, our research supplements the extensive theoretical and simulation studies on the motion of DNA under electrophoresis, in regards of DNA collision, hooking and formation of hernias in confined structures.

In Chapter 3 and 4, we developed a perfluoro coating on GLAD film based pSi-LDI (SMALDI) for convenient on-chip sample cleanup, and achieved biofluid metabolite quantitation using the device. Perfluoro coatings on pSi are known to minimize the chemical background generated from the LDI surface in MS analysis, and the same proved true on GLAD based Si films. Newly recognized in our work is that using defect-laden perfluoro coatings for on-chip desalting allows less sample preparation and provides a batch analysis method, particularly, for analysis of highly polar metabolites. pSi-LDI is an important complementary detection technique for metabolomics studies. The desalting method and coating approach explored here is very likely to apply to various pSi surfaces prepared by other methods, such as by etching. Also, the direct separation of highly polar small molecules from background electrolytes through crystallization on coating defects may be adapted to broader applications. Although we did not have the instrumental tools

available to identify all the metabolites detected by SMALDI, our results show that it is a promising method to detect more than 70 metabolites if coupled with MS/MS analysis. The precision offered by LDI is not competitive with LC-ESI, but pSi-LDI has notable advantages in high sensitivity and ease of use as a routine, batch analytical technique. The SMALDI platform shows promise that it can be developed for a wide range of metabolomic studies. In the next stage of research, following satisfactory MS/MS interfacing, SMALDI can follow SALDI as a tool to provide broad coverage of metabolites, and lead to better understanding of associated metabolic pathways.

## 5.2 Future work

As the next step, it will be worthwhile to complete current studies on metabolite profiling by SMALDI. The workflow of serum sample analysis by SMALDI-MS illustrated in Figure 4-1 probably also applies to analysis of more complex samples, such as blood and urine. The suitability will be easy to prove or disprove. More effort should be placed on customizing a MALDI-TOT/TOF mass spectrometer for SMALDI. It is essential to identify all the metabolites detected by SMALDI to validate the method. Moreover, it is useful to know which adduct ions are formed in the LDI process. According to results from SMALDI and other pSi-LDI surfaces,[114]  $[M-H]^-$  is the main and almost the only adduct formed in negative ion mode, whereas  $[M+Na]^+$  and  $[M+K]^+$  can appear in positive ion mode along with  $[M+H]^+$ , which raises difficulty in metabolite identification by  $m/z$  alone. The applicability of Bruker UltrafleXtreme for silicon SMALDI chips is problematic, based on the results in Chapter 4, and the 6-month time already spent in trying to optimize the instrument for this low mass application. Obtaining access to an AB Sciex

TOF/TOF 4800 for future work in MS-MS is probably the most efficient path forward, given past success with that instrument. This may require partnering with another research team, since the existing unit suffered a turbo pump failure that spread so much metallic particulate through the instrument that it may not be repairable.

Chapters 3 and 4 are undergoing review at the time of drafting this thesis. The reviewers requested information on the mechanism of salt segregation, but while this an interesting questioning it is also a challenging one to address. Since surface contact angle clearly plays a major role, studying the effect of contact angle on a few reasonably easily observed variables might provide some further insight into the process. Contact angle could be evaluated as a function of the entire drying cycle, as the salt concentration rises to saturation. This would provide some insight into the last stages of crystallization, and when it begins to occur. The droplet evaporation could also be monitored visually over time, both from above, and from below with a transparent substrate in use. Super hydrophobic characteristics on a post or porous surface arise in part from the way in which the contact droplet penetrates the pores. Following changes in the view of the droplet from underneath, based on the effects of index of refraction differences where water penetrates the pores, could provide a means to further understand the effect of 150 and 120 ° contact angles on nucleation and crystallization. These studies would provide some rapid insight, however, a true evaluation of mechanism is likely to be a long complex project.

Other than metabolite profiling, SMALDI has potential to serve as a platform for studies on metabolism processes. Teemu Nissila et al coated a thin layer of TiO<sub>2</sub> on silicon

micropillars and utilized the photocatalyzed redox reactions on  $\text{TiO}_2$  to mimick phase I in drug metabolism.[226] Drug metabolism usually takes place in the human liver and consists of three phases. Phase I includes modifications of drugs through oxidation, reduction and hydrolysis reactions, catalyzed by cytochrome P450 enzymes. The  $\text{TiO}_2$  layer is used to catalyze oxidation and reduction of drugs (e.g., verapamil), and the silicon micropillar substrate functions as a nanoreactor to increase the surface area and so the reaction rates. An ESI tip was integrated on the  $\text{TiO}_2$  nanoreactor chip to detect the photocatalytic products of selected drugs. The results show that coverage of 80% of phase I metabolic products can be obtained using this  $\text{TiO}_2$  nanoreactor/ESI chip. However, this mimicking system is not comparable to *in vivo* metabolism in which phase II and III are involved.

This above idea is very feasible to implement on SMALDI. GLAD can fabricate  $\text{TiO}_2$  coated silicon nanocolumns and other variants for higher reaction efficiency. Drug metabolism products can be directly detected by SMALDI-MS without integration of an ESI tip. In addition, it is possible to develop the technique by immobilizing phase II enzymes, such as glutathione S-transferases, on SMALDI chip. Chen Peng has demonstrated immobilized tryptic digestion for peptide mass fingerprinting on SMALDI.[139]

The study by Teemu Nissila et al is just one example of using nanoreactors for metabolic engineering. In recent years, there is growing research interest in immobilizing two or more enzymes on nanostructures to assemble efficient metabolic pathways.[227] This

work is motivated by observations that indicate cellular metabolism is regulated by multi-enzyme complexes on the membrane that perform multiple reaction steps.[228, 229] Nanoporous structure is a good choice for engineering the spatial organization of metabolic enzymes for cascade reactions.[6] The potential of GLAD thin films in this research field is unknown. Some pSi-LDI research groups have evaluated the performance of silicon nanowires as single enzyme nanoreactors,[230] although the application in metabolomic studies has not been reported. One possible drawback to this concept has to be raised, which is that GLAD thin films are a delicate nanostructure. GLAD films can clump or even collapse, in what is called a nanocarpet effect,[231] during multiple different solution exposures such as would be experienced with multistep surface functionalization. Avoiding the nanocarpet effect is a challenge that can be foreseen and would need to be avoided.

## REFERENCES

1. Arlett, J.L., E.B. Myers, and M.L. Roukes, *Comparative advantages of mechanical biosensors*. Nat Nano, 2011. **6**(4): p. 203-215.
2. Rosi, N.L. and C.A. Mirkin, *Nanostructures in Biodiagnostics*. Chemical Reviews, 2005. **105**(4): p. 1547-1562.
3. Anglin, E.J., et al., *Porous silicon in drug delivery devices and materials*. Advanced Drug Delivery Reviews, 2008. **60**(11): p. 1266-1277.
4. Vasir, J.K., M.K. Reddy, and V.D. Labhasetwar, *Nanosystems in drug targeting: opportunities and challenges*. Current Nanoscience, 2005. **1**(1): p. 47-64.
5. Allen, T.M. and P.R. Cullis, *Drug delivery systems: entering the mainstream*. Science, 2004. **303**(5665): p. 1818-1822.
6. Kuchler, A., et al., *Enzymatic reactions in confined environments*. Nat Nano, 2016. **11**(5): p. 409-420.
7. Rios, A., M. Zougagh, and M. Bouri, *Magnetic (nano)materials as an useful tool for sample preparation in analytical methods. A review*. Analytical Methods, 2013. **5**(18): p. 4558-4573.
8. Song, S., et al., *Functional nanoprobe for ultrasensitive detection of biomolecules*. Chemical Society Reviews, 2010. **39**(11): p. 4234-4243.
9. Erickson, D., et al., *Nanobiosensors: optofluidic, electrical and mechanical approaches to biomolecular detection at the nanoscale*. Microfluidics and Nanofluidics, 2008. **4**(1): p. 33-52.
10. Singh, S.P., et al., *Use of Pulsed-Field Gel Electrophoresis for Molecular Epidemiologic and Population Genetic Studies of Mycobacterium tuberculosis*. Journal of Clinical Microbiology, 1999. **37**(6): p. 1927-1931.
11. Champion, O.L., E.L. Best, and J.A. Frost, *Comparison of Pulsed-Field Gel Electrophoresis and Amplified Fragment Length Polymorphism Techniques for Investigating Outbreaks of Enteritis Due to Campylobacters*. Journal of Clinical Microbiology, 2002. **40**(6): p. 2263-2265.
12. Viovy, J.-L., *Electrophoresis of DNA and Other Polyelectrolytes: Physical Mechanisms*. Reviews of Modern Physics, 2000. **72**: p. 813-872.
13. Huang, L.R., et al., *A DNA Prism for High-speed Continuous Fractionation of Large DNA Molecules*. Nature Biotechnology, 2002. **20**: p. 1048-1051.
14. Viovy, J.-L., et al., *Irreversible Trapping of DNA during Crossed-field Gel Electrophoresis*. Electrophoresis, 1992. **13**: p. 1-6.
15. Gurrir, S., S.B. Smiths, and C. Bustamante, *Trapping of Megabase-sized DNA Molecules during Agarose Gel Electrophoresis*. Proceedings of the National Academy of Sciences of the United States of America, 1999. **96**: p. 453-458.
16. Slater, G.W. and J. Noolandi, *Effect of nonparallel alternating fields on the mobility of DNA in the biased reptation model of gel electrophoresis*. ELECTROPHORESIS, 1989. **10**(5-6): p. 413-428.
17. Volkmuth, W.D. and R.H. Austin, *DNA Electrophoresis in Microlithographic Arrays*. Nature, 1992. **358**: p. 600-602.

18. Bakajin, O., et al., *Separation of 100-Kilobase DNA Molecules in 10 Seconds*. Analytical Chemistry, 2001. **73**(24): p. 6053-6056.
19. Duke, T.A.J., et al., *Pulsed-field Electrophoresis in Microlithographic Arrays*. Electrophoresis, 1996. **17**: p. 1075-1079.
20. Zeng, Y., M. He, and D.J. Harrison, *Microfluidic Self-Patterning of Large-Scale Crystalline Nanoarrays for High-Throughput Continuous DNA Fractionation*. Angewandte Chemie International Edition, 2008. **47**: p. 6388-6391.
21. <DNA electrophoresis in microfabricated devices (2010)\_Kevin D. Dorfman.pdf>.
22. Kaji, N., et al., *Separation of Long DNA Molecules by Quartz Nanopillar Chips under a Direct Current Electric Field*. Analytical Chemistry, 2004. **76**(1): p. 15-22.
23. Randall, G.C. and P.S. Doyle, *Electrophoretic Collision of a DNA Molecule with an Insulating Post*. Physical Review Letters, 2004. **93**(5): p. 058102.
24. Doyle, P.S., et al., *Self-Assembled Magnetic Matrices for DNA Separation Chips*. Science, 2002. **295**(5563): p. 2237-2237.
25. Minc, N., et al., *Quantitative Microfluidic Separation of DNA in Self-Assembled Magnetic Matrixes*. Analytical Chemistry, 2004. **76**(13): p. 3770-3776.
26. Han, J. and H.G. Craighead, *Separation of Long DNA Molecules in a Microfabricated Entropic Trap Array*. Science, 2000. **288**(5468): p. 1026-1029.
27. Sheng, H., *Rapid separation of megabase sized DNA in nanostructures*.
28. Turmel, C., et al., *Molecular Detrapping and Band Narrowing with High Frequency Modulation of Pulsed Field Electrophoresis*. Nucleic Acids Research, 1990. **18**: p. 569-575.
29. Vollrath, D. and R.W. Davis, *Resolution of DNA molecules greater than 5 megabases by contour-clamped homogeneous electric fields*. Nucleic Acids Research, 1987. **15**(19): p. 7865-7876.
30. Smith, C.L. and C.R. Cantor, [28] *Purification, specific fragmentation, and separation of large DNA molecules*, in *Methods in Enzymology*. 1987, Academic Press. p. 449-467.
31. Lee, N., S. Obukhov, and M. Rubinstein, *Deterministic model of DNA gel electrophoresis in strong electric fields*. ELECTROPHORESIS, 1996. **17**(6): p. 1011-1017.
32. Long, D. and J.-L. Viovy, *Theory of Gel Electrophoresis in High Fields: Evolution of a Population of Hernias*. Physica A, 1997. **244**: p. 238-253.
33. Duke, T.A.J. and J.L. Viovy, *Motion of megabase deoxyribonucleic acid during field - inversion gel electrophoresis: Investigation by nonlocal Monte Carlo*. The Journal of Chemical Physics, 1992. **96**(11): p. 8552-8563.
34. Schwartz, D.C. and M. Koval, *Conformational dynamics of individual DNA molecules during gel electrophoresis*. Nature, 1989. **338**(6215): p. 520-522.
35. Oana, H., et al., *Periodic Motion of Large DNA Molecules during Steady Field Gel Electrophoresis*. Macromolecules, 1994. **27**(21): p. 6061-6067.
36. Kim, J.M. and P.S. Doyle, *Brownian Dynamics Simulations of a DNA Molecule Colliding with a Small Cylindrical Post*. Macromolecules, 2007. **40**(25): p. 9151-9163.
37. Burlatsky, S. and J. Deutch, *Influence of Solid Friction on Polymer Relaxation in Gel Electrophoresis*. Science, 1993. **260**: p. 1782-1784.

38. Viovy, J.-L., et al., *Solid Friction and Polymer Relaxation in Gel Electrophoresis*. Science, 1994. **264**(5155): p. 112-113.
39. Sturm, J. and G. Weill, *Direct observation of DNA chain orientation and relaxation by electric birefringence: Implications for the mechanism of separation during pulsed-field gel electrophoresis*. Physical Review Letters, 1989. **62**(13): p. 1484-1487.
40. Nazemifard, N., et al., *DNA Dynamics in Nanoscale Confinement under Asymmetric Pulsed Field Electrophoresis*. Angewandte Chemie International Edition, 2010. **122**: p. 3398-3401.
41. de Gennes, P.G., *Reptation of a Polymer Chain in the Presence of Fixed Obstacles*. The Journal of Chemical Physics, 1971. **55**(2): p. 572-579.
42. De Gennes, P.G., *Dynamics of Entangled Polymer Solutions. II. Inclusion of Hydrodynamic Interactions*. Macromolecules, 1976. **9**(4): p. 594-598.
43. Lumpkin, O.J., P. Déjardin, and B.H. Zimm, *Theory of gel electrophoresis of DNA*. Biopolymers, 1985. **24**(8): p. 1573-1593.
44. Tree, D.R., Y. Wang, and K.D. Dorfman, *Extension of DNA in a Nanochannel as a Rod-to-Coil Transition*. Physical Review Letters, 2013. **110**(20): p. 208103.
45. Walter, R., N.P. Jonas, and H.A. Robert, *DNA confinement in nanochannels: physics and biological applications*. Reports on Progress in Physics, 2012. **75**(10): p. 106601.
46. Reisner, W., et al., *Statics and Dynamics of Single DNA Molecules Confined in Nanochannels*. Physical Review Letters, 2005. **94**: p. 196101.
47. Schaefer, D.W., J.F. Joanny, and P. Pincus, *Dynamics of Semiflexible Polymers in Solution*. Macromolecules, 1980. **13**(5): p. 1280-1289.
48. Odijk, T., *The statistics and dynamics of confined or entangled stiff polymers*. Macromolecules, 1983. **16**(8): p. 1340-1344.
49. Randall, G.C. and P.S. Doyle, *DNA Deformation in Electric Fields: DNA Driven Past a Cylindrical Obstruction*. Macromolecules, 2005. **38**(6): p. 2410-2418.
50. Randall, G.C. and P.S. Doyle, *Collision of a DNA Polymer with a Small Obstacle*. Macromolecules, 2006. **39**(22): p. 7734-7745.
51. Holleran, S.P. and R.G. Larson, *Multiple Regimes of Collision of an Electrophoretically Translating Polymer Chain against a Thin Post*. Macromolecules, 2008. **41**(13): p. 5042-5054.
52. Wang, Y., D.R. Tree, and K.D. Dorfman, *Simulation of DNA Extension in Nanochannels*. Macromolecules, 2011. **44**(16): p. 6594-6604.
53. Gurrieri, S., et al., *Imaging of kinked configurations of DNA molecules undergoing orthogonal field alternating gel electrophoresis by fluorescence microscopy*. Biochemistry, 1990. **29**(13): p. 3396-3401.
54. Deutsch, J.M., *Dynamics of Pulsed-field Electrophoresis*. Physical Review Letters, 1987. **59**: p. 1255-1258.
55. Åkerman, B., *Barriers against DNA-loop formation in a porous matrix*. Physical Review E, 1996. **54**(6): p. 6685-6696.
56. Viovy, J.L., *Reptation-Breathing theory of pulsed electrophoresis: Dynamic regimes, antiresonance and symmetry breakdown effects*. ELECTROPHORESIS, 1989. **10**(5-6): p. 429-441.

57. Asbury, C.L. and G.v.d. Engh, *Trapping of DNA in Nonuniform Oscillating Electric Fields*. Biophysical Journal, 1998. **74**(2): p. 1024-1030.
58. Belkin, M., et al., *Plasmonic Nanopores for Trapping, Controlling Displacement, and Sequencing of DNA*. ACS Nano, 2015. **9**(11): p. 10598-10611.
59. Freedman, K.J., et al., *Nanopore sensing at ultra-low concentrations using single-molecule dielectrophoretic trapping*. Nature Communications, 2016. **7**: p. 10217.
60. Gallo-Villanueva, R.C., et al., *DNA Manipulation by Means of Insulator-based Dielectrophoresis Employing Direct Current Electric Field*. Electrophoresis, 2009. **30**: p. 4195-4205.
61. Wang, Q. and W.E. Moerner, *Optimal strategy for trapping single fluorescent molecules in solution using the ABEL trap*. Applied Physics B, 2010. **99**(1): p. 23-30.
62. Cohen, A.E. and W.E. Moerner, *Method for trapping and manipulating nanoscale objects in solution*. Applied Physics Letters, 2005. **86**(9): p. 093109.
63. Vlassarev, Dimitar M. and Jene A. Golovchenko, *Trapping DNA near a Solid-State Nanopore*. Biophysical Journal, 2012. **103**(2): p. 352-356.
64. Regtmeier, J., et al., *Dielectrophoretic trapping and polarizability of DNA: the role of spatial conformation*. Anal Chem, 2010. **82**(17): p. 7141-9.
65. Jones, T.B., *Basic theory of dielectrophoresis and electrorotation*. IEEE Engineering in medicine and Biology Magazine, 2003. **22**(6): p. 33-42.
66. Kuzyk, A., et al., *Dielectrophoretic Trapping of DNA Origami*. Small, 2008. **4**(4): p. 447-450.
67. Zheng, L., J.P. Brody, and P.J. Burke, *Electronic manipulation of DNA, proteins, and nanoparticles for potential circuit assembly*. Biosensors and Bioelectronics, 2004. **20**(3): p. 606-619.
68. Hölzel, R., et al., *Trapping Single Molecules by Dielectrophoresis*. Physical Review Letters, 2005. **95**(12): p. 128102.
69. Chiou, P.Y., A.T. Ohta, and M.C. Wu, *Massively parallel manipulation of single cells and microparticles using optical images*. Nature, 2005. **436**(7049): p. 370-372.
70. Thomas, R.S., H. Morgan, and N.G. Green, *Negative DEP traps for single cell immobilisation*. Lab on a Chip, 2009. **9**(11): p. 1534-1540.
71. Cummings, E.B. and A.K. Singh, *Dielectrophoresis in Microchips Containing Arrays of Insulating Posts: Theoretical and Experimental Results*. Analytical Chemistry, 2003. **75**(18): p. 4724-4731.
72. Lapizco-Encinas, B.H., et al., *Dielectrophoretic Concentration and Separation of Live and Dead Bacteria in an Array of Insulators*. Analytical Chemistry, 2004. **76**(6): p. 1571-1579.
73. Chou, C.-F., et al., *Electrodeless Dielectrophoresis of Single- and Double-Stranded DNA*. Biophysical Journal, 2002. **83**: p. 2170-2179.
74. Camacho-Alanis, F., L. Gan, and A. Ros, *Transitioning Streaming to Trapping in DC Insulator-based Dielectrophoresis for Biomolecules*. Sensors and Actuators B, 2012. **173**: p. 668-675.
75. Lapizco-Encinas, B.H., et al., *Dielectrophoretic Concentration and Separation of Live and Dead Bacteria in an Array of Insulators*. Analytical Chemistry, 2004. **76**: p. 1571-1579.

76. Dorfman, K.D., et al., *Beyond Gel Electrophoresis: Microfluidic Separations, Fluorescence Burst Analysis, and DNA Stretching*. Chemical Reviews, 2013. **113**(4): p. 2584-2667.
77. Ou, J., et al., *DNA electrophoresis in a sparse ordered post array*. Physical Review E, 2009. **79**(6): p. 061904.
78. Hillenkamp, F., et al., *Matrix-Assisted Laser Desorption/Ionization Mass Spectrometry of Biopolymers*. Analytical Chemistry, 1991. **63**(24): p. 1193A-1203A.
79. Tanaka, K., et al., *Protein and polymer analyses up to m/z 100 000 by laser ionization time-of-flight mass spectrometry*. Rapid Communications in Mass Spectrometry, 1988. **2**(8): p. 151-153.
80. Lewis, J.K., J. Wei, and G. Siuzdak, *Matrix-Assisted Laser Desorption/Ionization Mass Spectrometry in Peptide and Protein Analysis*, in *Encyclopedia of Analytical Chemistry*. 2006, John Wiley & Sons, Ltd.
81. Dattelbaum, A.M. and S. Iyer, *Surface-assisted laser desorption/ionization mass spectrometry*. Expert Review of Proteomics, 2006. **3**(1): p. 153-161.
82. Law, K.P. and J.R. Larkin, *Recent advances in SALDI-MS techniques and their chemical and bioanalytical applications*. Analytical and Bioanalytical Chemistry, 2011. **399**(8): p. 2597-2622.
83. Arakawa, R. and H. Kawasaki, *Functionalized Nanoparticles and Nanostructured Surfaces for Surface-Assisted Laser Desorption/Ionization Mass Spectrometry*. Analytical Sciences, 2010. **26**(12): p. 1229-1240.
84. Dunn, W.B. and D.I. Ellis, *Metabolomics: Current analytical platforms and methodologies*. TrAC Trends in Analytical Chemistry, 2005. **24**(4): p. 285-294.
85. Patti, G.J., et al., *Detection of Carbohydrates and Steroids by Cation-Enhanced Nanostructure-Initiator Mass Spectrometry (NIMS) for Biofluid Analysis and Tissue Imaging*. Analytical Chemistry, 2010. **82**(1): p. 121-128.
86. Sunner, J., E. Dratz, and Y.-C. Chen, *Graphite surface-assisted laser desorption/ionization time-of-flight mass spectrometry of peptides and proteins from liquid solutions*. Analytical chemistry, 1995. **67**(23): p. 4335-4342.
87. Wei, J., J.M. Buriak, and G. Siuzdak, *Desorption-ionization mass spectrometry on porous silicon*. Nature, 1999. **399**(6733): p. 243-246.
88. Peterson, D.S., *Matrix-free methods for laser desorption/ionization mass spectrometry*. Mass Spectrometry Reviews, 2007. **26**(1): p. 19-34.
89. Lewis, W.G., et al., *Desorption/ionization on silicon (DIOS) mass spectrometry: background and applications*. International Journal of Mass Spectrometry, 2003. **226**(1): p. 107-116.
90. Shen, Z., et al., *Porous Silicon as a Versatile Platform for Laser Desorption/Ionization Mass Spectrometry*. Analytical Chemistry, 2001. **73**(3): p. 612-619.
91. Tsao, C.-W., et al., *Dynamic Electrowetting on Nanofilament Silicon for Matrix-Free Laser Desorption/Ionization Mass Spectrometry*. Analytical Chemistry, 2008. **80**(8): p. 2973-2981.
92. Xiao, Y., et al., *Impacts of Surface Morphology on Ion Desorption and Ionization in Desorption Ionization on Porous Silicon (DIOS) Mass Spectrometry*. The Journal of Physical Chemistry C, 2009. **113**(8): p. 3076-3083.

93. Street, R.A., et al., *Reflectivity of disordered silicon nanowires*. Applied Physics Letters, 2008. **93**(16): p. 163109.
94. Shen, Q. and T. Toyoda, *Dependence of thermal conductivity of porous silicon on porosity characterized by photoacoustic technique*. Review of Scientific Instruments, 2003. **74**(1): p. 601-603.
95. Alimpiev, S., et al., *On the mechanism of laser-induced desorption-ionization of organic compounds from etched silicon and carbon surfaces*. The Journal of Chemical Physics, 2001. **115**(4): p. 1891-1901.
96. Alimpiev, S., et al., *On the role of defects and surface chemistry for surface-assisted laser desorption ionization from silicon*. The Journal of Chemical Physics, 2008. **128**(1): p. 014711.
97. Grechnikov, A.A., *Analytical capabilities of surface-assisted laser desorption/ionization in the determination of low-molecular-weight volatile compounds*. Journal of Analytical Chemistry, 2015. **70**(9): p. 1047-1054.
98. Szabo, Z., et al., *Laser desorption/ionization mass spectrometric analysis of small molecules using fullerene - derivatized silica as energy - absorbing material*. Journal of mass spectrometry, 2010. **45**(5): p. 545-552.
99. Lim, A.Y., et al., *Separation of fingerprint constituents using magnetic silica nanoparticles and direct on-particle SALDI-TOF-mass spectrometry*. Journal of Chromatography B, 2011. **879**(23): p. 2244-2250.
100. López de Laorden, C., et al., *Nanostructured Indium Tin Oxide Slides for Small-Molecule Profiling and Imaging Mass Spectrometry of Metabolites by Surface-Assisted Laser Desorption Ionization MS*. Analytical Chemistry, 2015. **87**(1): p. 431-440.
101. Kawasaki, H., et al., *Functionalized graphene-coated cobalt nanoparticles for highly efficient surface-assisted laser desorption/ionization mass spectrometry analysis*. Analytical chemistry, 2012. **84**(21): p. 9268-9275.
102. Nayak, R. and D.R. Knapp, *Effects of thin-film structural parameters on laser desorption/ionization from porous alumina*. Analytical chemistry, 2007. **79**(13): p. 4950-4956.
103. Wada, Y., T. Yanagishita, and H. Masuda, *Ordered porous alumina geometries and surface metals for surface-assisted laser desorption/ionization of biomolecules: possible mechanistic implications of metal surface melting*. Analytical chemistry, 2007. **79**(23): p. 9122-9127.
104. Xu, S., et al., *Carbon nanotubes as assisted matrix for laser desorption/ionization time-of-flight mass spectrometry*. Analytical Chemistry, 2003. **75**(22): p. 6191-6195.
105. Pan, C., et al., *Carbon nanotubes as adsorbent of solid-phase extraction and matrix for laser desorption/ionization mass spectrometry*. Journal of the American Society for Mass Spectrometry, 2005. **16**(2): p. 263-270.
106. Ren, S.f. and Y.l. Guo, *Oxidized carbon nanotubes as matrix for matrix - assisted laser desorption/ionization time - of - flight mass spectrometric analysis of biomolecules*. Rapid communications in mass spectrometry, 2005. **19**(2): p. 255-260.
107. Ng, K.-M., et al., *Ion-Desorption Efficiency and Internal-Energy Transfer in Surface-Assisted Laser Desorption/Ionization: More Implication(s) for the*

- Thermal-Driven and Phase-Transition-Driven Desorption Process*. The Journal of Physical Chemistry C, 2015. **119**(41): p. 23708-23720.
108. Woo, H.-K., et al., *Nanostructure-initiator mass spectrometry: a protocol for preparing and applying NIMS surfaces for high-sensitivity mass analysis*. Nat. Protocols, 2008. **3**(8): p. 1341-1349.
  109. Chen, W.Y., et al., *Fabrication of nanostructured silicon by metal-assisted etching and its effects on matrix-free laser desorption/ionization mass spectrometry*. Analytica Chimica Acta, 2011. **687**(2): p. 97-104.
  110. Xu, Y., C. Ni, and A. Sarangan. *Silicon nanowire photodetectors made by metal-assisted chemical etching*. 2016.
  111. Muck, A., et al., *Lithographically patterned silicon nanowire arrays for matrix free LDI-TOF/MS analysis of lipids*. Lab on a Chip, 2010. **10**(3): p. 320-325.
  112. Dupré, M., et al., *Investigation of Silicon-Based Nanostructure Morphology and Chemical Termination on Laser Desorption Ionization Mass Spectrometry Performance*. Analytical Chemistry, 2012. **84**(24): p. 10637-10644.
  113. Morris, N.J., et al., *Laser desorption ionization (LDI) silicon nanopost array chips fabricated using deep UV projection lithography and deep reactive ion etching*. RSC Advances, 2015. **5**(88): p. 72051-72057.
  114. Korte, A.R., et al., *Large-Scale Metabolite Analysis of Standards and Human Serum by Laser Desorption Ionization Mass Spectrometry from Silicon Nanopost Arrays*. Analytical Chemistry, 2016. **88**(18): p. 8989-8996.
  115. Gulbakan, B., et al., *Laser Desorption Ionization Mass Spectrometry on Silicon Nanowell Arrays*. Analytical Chemistry, 2010. **82**(18): p. 7566-7575.
  116. Kuzema, P.A., *Small-molecule analysis by surface-assisted laser desorption/ionization mass spectrometry*. Journal of Analytical Chemistry, 2011. **66**(13): p. 1227-1242.
  117. Robbie, K. and M.J. Brett, *Sculptured thin films and glancing angle deposition: Growth mechanics and applications*. Journal of Vacuum Science & Technology A, 1997. **15**(3): p. 1460-1465.
  118. Robbie, K., J. Sit, and M. Brett, *Advanced techniques for glancing angle deposition*. Journal of Vacuum Science & Technology B, 1998. **16**(3): p. 1115-1122.
  119. Jemere, A.B., et al., *Matrix-free laser desorption/ionization mass spectrometry using silicon glancing angle deposition (GLAD) films*. Rapid Communications in Mass Spectrometry, 2010. **24**(15): p. 2305-2311.
  120. Taschuk, M.T., M.M. Hawkeye, and M.J. Brett, *Glancing angle deposition*. Handbook of Deposition Technologies for Films and Coatings, 2010: p. 621-678.
  121. Hawkeye, M.M. and M.J. Brett, *Glancing angle deposition: fabrication, properties, and applications of micro-and nanostructured thin films*. Journal of Vacuum Science & Technology A, 2007. **25**(5): p. 1317-1335.
  122. Bezuidenhout, L.W., *Molecular separations using nanostructured porous thin films fabricated by glancing angle deposition*. 2011.
  123. Michalcik, Z., et al., *Photocatalytic Activity of Nanostructured Titanium Dioxide Thin Films*. International Journal of Photoenergy, 2012. **2012**: p. 8.
  124. Xu, D., et al., *Hydrolysis and silanization of the hydrosilicon surface of freshly prepared porous silicon by an amine catalytic reaction*. New Journal of Chemistry, 2003. **27**(2): p. 300-306.

125. Trauger, S.A., et al., *High Sensitivity and Analyte Capture with Desorption/Ionization Mass Spectrometry on Silylated Porous Silicon*. Analytical Chemistry, 2004. **76**(15): p. 4484-4489.
126. Buriak, J.M., et al., *Lewis acid mediated hydrosilylation on porous silicon surfaces*. Journal of the American Chemical Society, 1999. **121**(49): p. 11491-11502.
127. Buriak, J.M. and M.J. Allen, *Lewis acid mediated functionalization of porous silicon with substituted alkenes and alkynes*. Journal of the American Chemical Society, 1998. **120**(6): p. 1339-1340.
128. Boukherroub, R., et al., *Thermal hydrosilylation of undecylenic acid with porous silicon*. Journal of the Electrochemical Society, 2002. **149**(2): p. H59-H63.
129. Guan, B., et al., *Antibody Modified Porous Silicon Microparticles for the Selective Capture of Cells*. Bioconjugate Chemistry, 2014. **25**(7): p. 1282-1289.
130. Gooding, J.J. and Y. Zhu, *5 - Modifying porous silicon with self-assembled monolayers for biomedical applications A2 - Santos, Hélder A*, in *Porous Silicon for Biomedical Applications*. 2014, Woodhead Publishing. p. 81-103.
131. Chan, S., et al., *Nanoscale silicon microcavities for biosensing*. Materials Science and Engineering: C, 2001. **15**(1): p. 277-282.
132. Steinem, C., et al., *DNA hybridization-enhanced porous silicon corrosion: mechanistic investigations and prospect for optical interferometric biosensing*. Tetrahedron, 2004. **60**(49): p. 11259-11267.
133. Serda, R.E., et al., *The association of silicon microparticles with endothelial cells in drug delivery to the vasculature*. Biomaterials, 2009. **30**(13): p. 2440-2448.
134. Low, S.P., et al., *The biocompatibility of porous silicon in tissues of the eye*. Biomaterials, 2009. **30**(15): p. 2873-2880.
135. Kurczyk, M.E., et al., *Nanostructure Imaging Mass Spectrometry: The Role of Fluorocarbons in Metabolite Analysis and Yoctomole Level Sensitivity*. Mass Spectrometry Imaging of Small Molecules, 2015: p. 141-149.
136. Nordström, A., et al., *Surfactant-enhanced desorption/ionization on silicon mass spectrometry*. Analytical chemistry, 2006. **78**(1): p. 272-278.
137. Northen, T.R., et al., *Clathrate nanostructures for mass spectrometry*. Nature, 2007. **449**(7165): p. 1033-1036.
138. Greving, M.P., G.J. Patti, and G. Siuzdak, *Nanostructure-initiator mass spectrometry metabolite analysis and imaging*. Analytical chemistry, 2010. **83**(1): p. 2-7.
139. Peng, C., *Thin Films for Solid Matrix Laser Desorption/Ionization for Biomarker Analysis*.
140. Lowe, R.D., et al., *Combined Immunocapture and Laser Desorption/Ionization Mass Spectrometry on Porous Silicon*. Analytical Chemistry, 2010. **82**(10): p. 4201-4208.
141. Go, E.P., et al., *Selective Metabolite and Peptide Capture/Mass Detection Using Fluorous Affinity Tags*. Journal of Proteome Research, 2007. **6**(4): p. 1492-1499.
142. Yanes, O., et al., *Nanostructure Initiator Mass Spectrometry: Tissue Imaging and Direct Biofluid Analysis*. Analytical Chemistry, 2009. **81**(8): p. 2969-2975.
143. Tweeddale, H., L. Notley-McRobb, and T. Ferenci, *Effect of Slow Growth on Metabolism of Escherichia coli, as Revealed by Global Metabolite Pool ("Metabolome") Analysis*. Journal of Bacteriology, 1998. **180**(19): p. 5109-5116.

144. Fiehn, O., *Metabolomics—the link between genotypes and phenotypes*. Plant molecular biology, 2002. **48**(1-2): p. 155-171.
145. Orešič, M., A. Vidal-Puig, and V. Hänninen, *Metabolomic approaches to phenotype characterization and applications to complex diseases*. Expert review of molecular diagnostics, 2006. **6**(4): p. 575-585.
146. Snell, E.E., B.M. Guirard, and R.J. Williams, *Occurrence in natural products of a physiologically active metabolite of pyridoxine*. Journal of Biological Chemistry, 1942. **143**: p. 519-530.
147. Gates, S.C. and C.C. Sweeley, *Quantitative metabolic profiling based on gas chromatography*. Clinical Chemistry, 1978. **24**(10): p. 1663-1673.
148. Horning, E.C. and M.-G. Horning, *Metabolic profiles: gas-phase methods for analysis of metabolites*. Clinical chemistry, 1971. **17**(8): p. 802-809.
149. Gieger, C., et al., *Genetics meets metabolomics: a genome-wide association study of metabolite profiles in human serum*. PLoS Genet, 2008. **4**(11): p. e1000282.
150. Smedsgaard, J. and J. Nielsen, *Metabolite profiling of fungi and yeast: from phenotype to metabolome by MS and informatics*. Journal of experimental botany, 2005. **56**(410): p. 273-286.
151. Beckonert, O., et al., *Metabolic profiling, metabolomic and metabonomic procedures for NMR spectroscopy of urine, plasma, serum and tissue extracts*. Nat. Protocols, 2007. **2**(11): p. 2692-2703.
152. Want, E.J., et al., *From Exogenous to Endogenous: The Inevitable Imprint of Mass Spectrometry in Metabolomics*. Journal of Proteome Research, 2006. **6**(2): p. 459-468.
153. Guo, K. and L. Li, *High-performance isotope labeling for profiling carboxylic acid-containing metabolites in biofluids by mass spectrometry*. Analytical chemistry, 2010. **82**(21): p. 8789-8793.
154. Birkemeyer, C., et al., *Metabolome analysis: the potential of in vivo labeling with stable isotopes for metabolite profiling*. Trends in biotechnology, 2005. **23**(1): p. 28-33.
155. Wang, W., et al., *Quantification of Proteins and Metabolites by Mass Spectrometry without Isotopic Labeling or Spiked Standards*. Analytical Chemistry, 2003. **75**(18): p. 4818-4826.
156. Johnson, C.H., et al., *Bioinformatics: The Next Frontier of Metabolomics*. Analytical Chemistry, 2014. **87**(1): p. 147-156.
157. Scalbert, A., et al., *Mass-spectrometry-based metabolomics: limitations and recommendations for future progress with particular focus on nutrition research*. Metabolomics, 2009. **5**(4): p. 435-458.
158. Kosmides, A.K., et al., *Metabolomic Fingerprinting: Challenges and Opportunities*. 2013. **41**(3): p. 205-221.
159. Idborg, H., P.-O. Edlund, and S.P. Jacobsson, *Multivariate approaches for efficient detection of potential metabolites from liquid chromatography/mass spectrometry data*. Rapid Communications in Mass Spectrometry, 2004. **18**(9): p. 944-954.
160. Xu, R.N., et al., *Recent advances in high-throughput quantitative bioanalysis by LC-MS/MS*. Journal of Pharmaceutical and Biomedical Analysis, 2007. **44**(2): p. 342-355.

161. Gowda, G.A.N. and D. Raftery, *Quantitating Metabolites in Protein Precipitated Serum Using NMR Spectroscopy*. Analytical Chemistry, 2014. **86**(11): p. 5433-5440.
162. Jiménez-Sánchez, C., et al., *Comprehensive, untargeted, and qualitative RP-HPLC-ESI-QTOF/MS2 metabolite profiling of green asparagus (*Asparagus officinalis*)*. Journal of Food Composition and Analysis, 2016. **46**: p. 78-87.
163. Pellati, F., et al., *HPLC-DAD and HPLC-ESI-MS/MS methods for metabolite profiling of propolis extracts*. Journal of Pharmaceutical and Biomedical Analysis, 2011. **55**(5): p. 934-948.
164. Iwasaki, Y., et al., *Separation Technique for the Determination of Highly Polar Metabolites in Biological Samples*. Metabolites, 2012. **2**(3): p. 496.
165. Ivanisevic, J., et al., *Toward 'Omic Scale Metabolite Profiling: A Dual Separation–Mass Spectrometry Approach for Coverage of Lipid and Central Carbon Metabolism*. Analytical Chemistry, 2013. **85**(14): p. 6876-6884.
166. Chen, J., et al., *Metabonomics study of liver cancer based on ultra performance liquid chromatography coupled to mass spectrometry with HILIC and RPLC separations*. Analytica Chimica Acta, 2009. **650**(1): p. 3-9.
167. Ramautar, R., G.W. Somsen, and G.J. de Jong, *CE - MS in metabolomics*. Electrophoresis, 2009. **30**(1): p. 276-291.
168. Nordström, A., et al., *Multiple ionization mass spectrometry strategy used to reveal the complexity of metabolomics*. Analytical chemistry, 2008. **80**(2): p. 421-429.
169. Law, K.P., *Laser desorption/ionization mass spectrometry on nanostructured semiconductor substrates: DIOS™ and QuickMass™*. International Journal of Mass Spectrometry, 2010. **290**(2–3): p. 72-84.
170. Wen, X., S. Dagan, and V.H. Wysocki, *Small-molecule analysis with silicon-nanoparticle-assisted laser desorption/ionization mass spectrometry*. Analytical chemistry, 2007. **79**(2): p. 434-444.
171. Nayak, R. and D.R. Knapp, *Matrix-free LDI mass spectrometry platform using patterned nanostructured gold thin film*. Analytical chemistry, 2010. **82**(18): p. 7772-7778.
172. Southern, E.M., et al., *A Model for the Separation of Large DNA Molecules by Crossed Field Gel Electrophoresis*. Nucleic Acids Research, 1987. **15**: p. 5925-2943.
173. Gunderson, K. and G. Chu, *Pulsed-field Electrophoresis of Megabase-sized DNA*. Molecular and Cellular Biology, 1991. **11**: p. 3348-3354.
174. Zhang, M., et al., *Preparation of megabase-sized DNA from a variety of organisms using the nuclei method for advanced genomics research*. Nat. Protocols, 2012. **7**(3): p. 467-478.
175. Liu, Y.-G., et al., *Complementation of plant mutants with large genomic DNA fragments by a transformation-competent artificial chromosome vector accelerates positional cloning*. Proceedings of the National Academy of Sciences, 1999. **96**(11): p. 6535-6540.
176. Wing, R.A., H.-B. Zhang, and S.D. Tanksley, *Map-based cloning in crop plants. Tomato as a model system: I. Genetic and physical mapping of jointless*. Molecular and General Genetics MGG, 1994. **242**(6): p. 681-688.

177. Zhang, H. and M.J. Wirth, *Electromigration of Single Molecules of DNA in a Crystalline Array of 300-nm Silica Colloids*. Analytical Chemistry, 2005. **77**(5): p. 1237-1242.
178. Stigter, D., *Influence of Agarose Gel on Electrophoretic Stretch, on Trapping, and on Relaxation of DNA*. Macromolecules, 2000. **33**(23): p. 8878-8889.
179. Srivastava, S.K., A. Gencoglu, and A.R. Minerick, *DC Insulator Dielectrophoretic Applications in Microdevice Technology: a Review*. Analytical and Bioanalytical Chemistry, 2011. **399**: p. 301-321.
180. Bustamante, C., S. Gurrieri, and S.B. Smith, *Towards a Molecular Description of Pulsed-field Gel Electrophoresis*. Trends Biotechnol., 1993. **11**: p. 23-30.
181. Effenhauser, C.S., et al., *Integrated capillary electrophoresis on flexible silicone microdevices: analysis of DNA restriction fragments and detection of single DNA molecules on microchips*. Analytical Chemistry, 1997. **69**(17): p. 3451-3457.
182. Perkins, T.T., et al., *Stretching of a Single Tethered Polymer in a Uniform Flow*. Science, 1995. **268**(5207): p. 83-87.
183. Bakajin, O.B., et al., *Electrohydrodynamic Stretching of DNA in Confined Environments*. Physical Review Letters, 1998. **80**(12): p. 2737-2740.
184. Nazemifard, N., et al., *Nonmonotonous Variation of DNA Angular Separation during Asymmetric Pulsed Field Electrophoresis*. Electrophoresis, 2013. **34**(17): p. 2453-2463.
185. Deutsch, J.M., *Theoretical Studies of DNA during Gel Electrophoresis*. Science, 1988. **240**: p. 922-924.
186. Deutsch, J.M. and T.L. Madden, *Theoretical Studies of DNA during Gel Electrophoresis*. Journal of Chemical Physics, 1988. **90**: p. 2476-2484.
187. Volkmuth, W.D., et al., *DNA electrodiffusion in a 2D array of posts*. Physical Review Letters, 1994. **72**(13): p. 2117-2120.
188. de Gennes, P.-G., *Scaling Concepts in Polymer Physics*. 1979: Cornell University Press.
189. Smith, S.B. and A.J. Bendich, *Electrophoretic charge density and persistence length of DNA as measured by fluorescence microscopy*. Biopolymers, 1990. **29**(8-9): p. 1167-1173.
190. Morse, D.C., *Viscoelasticity of Concentrated Isotropic Solutions of Semiflexible Polymers. 2. Linear Response*. Macromolecules, 1998. **31**(20): p. 7044-7067.
191. Tang, J., N. Du, and P.S. Doyle, *Compression and Self-entanglement of Single DNA Molecules under Uniform Electric Field*. Proceedings of the National Academy of Sciences of the United States of America, 2011. **108**: p. 16153-16158.
192. Jones, T.B., *Electromechanics of Particles*. 1995: Cambridge University Press.
193. Hsieh, S.-S., H.-C. Lin, and C.-Y. Lin, *Electroosmotic Flow Velocity Measurements in a Square Microchannel*. Colloid and Polymer Science, 2006. **284**: p. 1275-1286.
194. Hsieh, C.-C., A. Balducci, and P.S. Doyle, *Ionic Effects on the Equilibrium Dynamics of DNA Confined in Nanoslits*. Nano Letters, 2008. **8**: p. 1683-1688.
195. Go, E.P., et al., *Desorption/Ionization on Silicon Nanowires*. Analytical Chemistry, 2005. **77**(6): p. 1641-1646.
196. Kawasaki, H., et al., *Platinum Nanoflowers for Surface-Assisted Laser Desorption/Ionization Mass Spectrometry of Biomolecules*. The Journal of Physical Chemistry C, 2007. **111**(44): p. 16278-16283.

197. Stumpo, K.A. and D.H. Russell, *Anion Effects on Ionization Efficiency Using Gold Nanoparticles as Matrices for LDI-MS*. The Journal of Physical Chemistry C, 2009. **113**(5): p. 1641-1647.
198. Guinan, T.M., et al., *Direct detection of illicit drugs from biological fluids by desorption/ionization mass spectrometry with nanoporous silicon microparticles*. Analyst, 2015. **140**(23): p. 7926-7933.
199. Hawkeye, M.M. and M.J. Brett, *Glancing angle deposition: Fabrication, properties, and applications of micro- and nanostructured thin films*. Journal of Vacuum Science & Technology A, 2007. **25**(5): p. 1317-1335.
200. Vaidyanathan, S., et al., *A laser desorption ionisation mass spectrometry approach for high throughput metabolomics*. Metabolomics, 2005. **1**(3): p. 243-250.
201. Duan, J., H. Wang, and Q. Cheng, *On-Plate Desalting and SALDI-MS Analysis of Peptides with Hydrophobic Silicate Nanofilms on a Gold Substrate*. Analytical Chemistry, 2010. **82**(22): p. 9211-9220.
202. El Idrissi, A., *Taurine increases mitochondrial buffering of calcium: role in neuroprotection*. Amino Acids, 2008. **34**(2): p. 321-328.
203. Platten, M., et al., *Treatment of Autoimmune Neuroinflammation with a Synthetic Tryptophan Metabolite*. Science, 2005. **310**(5749): p. 850-855.
204. Fonteh, N.A., et al., *Free amino acid and dipeptide changes in the body fluids from Alzheimer's disease subjects*. Amino Acids, 2007. **32**(2): p. 213-224.
205. Kusano, M., et al., *Laser Desorption/Ionization Mass Spectrometry (LDI-MS) of Lipids with Iron Oxide Nanoparticle-Coated Targets*. Mass Spectrometry, 2014. **3**(1): p. A0026.
206. Czech, C., et al., *Metabolite Profiling of Alzheimer's Disease Cerebrospinal Fluid*. PLoS ONE, 2012. **7**(2): p. e31501.
207. Suhre, K. and C. Gieger, *Genetic variation in metabolic phenotypes: study designs and applications*. Nat Rev Genet, 2012. **13**(11): p. 759-769.
208. Weiss, R.H. and K. Kim, *Metabolomics in the study of kidney diseases*. Nat Rev Nephrol, 2012. **8**(1): p. 22-33.
209. Guma, M., S. Tiziani, and G.S. Firestein, *Metabolomics in rheumatic diseases: desperately seeking biomarkers*. Nat Rev Rheumatol, 2016. **12**(5): p. 269-281.
210. Wood, P.L., *Mass Spectrometry Strategies for Clinical Metabolomics and Lipidomics in Psychiatry, Neurology, and Neuro-Oncology*. Neuropsychopharmacology, 2014. **39**(1): p. 24-33.
211. Dettmer, K., P.A. Aronov, and B.D. Hammock, *Mass spectrometry-based metabolomics*. Mass Spectrometry Reviews, 2007. **26**(1): p. 51-78.
212. Jemal, M., *High-throughput quantitative bioanalysis by LC/MS/MS*. Biomedical Chromatography, 2000. **14**(6): p. 422-429.
213. Xiao, J.F., B. Zhou, and H.W. Ransom, *Metabolite identification and quantitation in LC-MS/MS-based metabolomics*. TrAC Trends in Analytical Chemistry, 2012. **32**: p. 1-14.
214. Sweetman, M.J., et al., *Rapid, metal-free hydrosilanisation chemistry for porous silicon surface modification*. Chemical Communications, 2015. **51**(53): p. 10640-10643.
215. Parsons, H.M., et al., *Spectral relative standard deviation: a practical benchmark in metabolomics*. Analyst, 2009. **134**(3): p. 478-485.

216. Dunn, W.B., et al., *Metabolic profiling of serum using Ultra Performance Liquid Chromatography and the LTQ-Orbitrap mass spectrometry system*. Journal of Chromatography B, 2008. **871**(2): p. 288-298.
217. Bernier, M., V. Wysocki, and S. Dagan, *Laser Desorption Ionization of small molecules assisted by Tungsten oxide and Rhenium oxide particles*. Journal of mass spectrometry : JMS, 2015. **50**(7): p. 891-898.
218. Greer, T., R. Sturm, and L. Li, *MASS SPECTROMETRY IMAGING FOR DRUGS AND METABOLITES*. Journal of proteomics, 2011. **74**(12): p. 2617-2631.
219. McLean, J.A., W.K. Russell, and D.H. Russell, *A High Repetition Rate (1 kHz) Microcrystal Laser for High Throughput Atmospheric Pressure MALDI-Quadrupole-Time-of-Flight Mass Spectrometry*. Analytical Chemistry, 2003. **75**(3): p. 648-654.
220. Gross, J.H., *Matrix-Assisted Laser Desorption/Ionization*, in *Mass Spectrometry: A Textbook*. 2011, Springer Berlin Heidelberg: Berlin, Heidelberg. p. 507-559.
221. Go, E.P., et al., *Desorption/Ionization on Silicon Time-of-Flight/Time-of-Flight Mass Spectrometry*. Analytical Chemistry, 2003. **75**(10): p. 2504-2506.
222. Sturm, R.M., et al., *Comparison of NIMS and MALDI platforms for neuropeptide and lipid mass spectrometric imaging in C. borealis brain tissue*. Analytical Methods, 2013. **5**(6): p. 1623-1628.
223. Guinan, T., et al., *Mass spectrometry imaging of fingerprint sweat on nanostructured silicon*. Chemical Communications, 2015. **51**(28): p. 6088-6091.
224. Colantonio, S., et al., *Quantitative Analysis of Phospholipids Using Nanostructured Laser Desorption Ionization Targets()*. Lipids, 2011. **46**(5): p. 469-477.
225. Rudd, D., et al., *Mass spectrometry imaging reveals new biological roles for choline esters and Tyrian purple precursors in muricid molluscs*. Scientific Reports, 2015. **5**: p. 13408.
226. Nissila, T., et al., *Integrated photocatalytic micropillar nanoreactor electrospray ionization chip for mimicking phase I metabolic reactions*. Lab on a Chip, 2011. **11**(8): p. 1470-1476.
227. Conrado, R.J., J.D. Varner, and M.P. DeLisa, *Engineering the spatial organization of metabolic enzymes: mimicking nature's synergy*. Current Opinion in Biotechnology, 2008. **19**(5): p. 492-499.
228. Campanella, M.E., H. Chu, and P.S. Low, *Assembly and regulation of a glycolytic enzyme complex on the human erythrocyte membrane*. Proceedings of the National Academy of Sciences of the United States of America, 2005. **102**(7): p. 2402-2407.
229. Winkel, B.S.J., *METABOLIC CHANNELING IN PLANTS*. Annual Review of Plant Biology, 2004. **55**(1): p. 85-107.
230. Elnathan, R., et al., *Versatile Particle-Based Route to Engineer Vertically Aligned Silicon Nanowire Arrays and Nanoscale Pores*. ACS Applied Materials & Interfaces, 2015. **7**(42): p. 23717-23724.
231. Fan, J.G., et al., *Nanocarpet Effect: Pattern Formation during the Wetting of Vertically Aligned Nanorod Arrays*. Nano Letters, 2004. **4**(11): p. 2133-2138.

## **APPENDIX A: RATIONAL FOR USING 105 NM PORE SIZE**

The most common separation media for the pulsed field electrophoresis is gel. Experimental evaluation of the pore sizes of gels are 150-350 nm and 5-100 nm for agarose and polyacrylamide, respectively.[12] Trapping is observed in these materials across this pore size range. Thus, with a 105 nm pore size in the colloidal crystal arising from the choice of 690 nm particle diameter, a comparison of models for trapping in gels and the particle beds is appropriate based on pore size.

The critical field strength of DNA trapping varies with pore size. The pore size affects the probability of DNA colliding with particles and the formation of the U/J shape. Larger pores will have less collision events, relative to smaller pores. However, with 55.8  $\mu\text{m}$  contour length and 1.31  $\mu\text{m}$  radius of gyration, T4 DNA molecules are strongly confined in 5-350 nm pores. Thus, collision and hooking are frequent across this pore size range, resulting in trapping of large size DNA during electrophoresis. The Odijk model of friction coefficient and relaxation time is appropriate for the specific 105 nm pore size used in this study.

## APPENDIX B: VIDEO LIST

All the videos are captured using a TIRF microscope with a 60x objective. Video 2-3 to Video 2-6 are cropped from the original view field, to highlight the dynamics of single DNA molecules. All the videos are sped up or slowed down, but the real acquisition time is shown in the videos. The video's bit resolution was highly compressed from the originals.

Video 2-1: T4 DNA are trapped under 2D pulse field electrophoresis, at 0.5 Hz. The applied field strength  $E_2 = 142.9$  V/cm,  $E_1 = \sqrt{2} E_2$ . At the beginning of the video, the DNA molecules are at rest without electric field, showing coiled conformation. At  $\sim 20$  s after the pulsed fields are applied, some molecules are immobilized in the separation sieves. The view field is  $123 \mu\text{m} \times 123 \mu\text{m}$ .

Video 2-2: With reverse spikes, T4 DNA are not trapped under pulsed field. The field strength and duration time of forward pulses  $E_1$  and  $E_2$  are the same as those in video F1. The parameters of the reverse spikes are shown in Table 1. The view field is  $123 \mu\text{m} \times 123 \mu\text{m}$ .

Video 2-3: The trapping of a single DNA at 2 Hz, with field strength  $E_2 = 142.9$  V/cm,  $E_1 = \sqrt{2} E_2$ . At the beginning of the video, the observed DNA molecule is in a free state.

Video 2-4: The trapping of a single DNA at 0.5 Hz, with field strength  $E_2 = 142.9$  V/cm,  $E_1 = \sqrt{2} E_2$ . At the beginning of the video, the observed DNA molecule is in a free state.

Video 2-5: At  $E_1 = 202.0$  V/cm, a J-shaped DNA that cannot be unhooked.

Video 2-6: The effect of the reverse spike field modulation. Two J-shaped DNA are observed at  $E_1 = 202.0$  V/cm. One is a freshly hooked DNA, the other one has already been pinned at the apex. The reverse spike relaxes both of the molecules and dislodges them from the apex. Afterwards, the originally pinned DNA follows the ratchet model, completing the reorientation normally.

## APPENDIX C: EFFECTIVE CHARGE DENSITY $\rho_{eff}$

In the analysis of DNA mobility, we assume the frictional force compensates the electric field force, giving:

$$\xi\mu E = Eq_{eff} \quad (\text{Equation C-2})$$

where  $\xi$  is frictional coefficient,  $q_{eff}$  is the total effective charge of T4 DNA. The effective charge density  $\rho_{eff}$  is defined as charge per base pair:

$$\rho_{eff} = q_{eff} / N = \mu_0 \xi_0 / N \quad (\text{Equation C-3})$$

In free solution, the frictional coefficient is:

$$\xi_0 = 6\pi\eta g_r \quad (\text{Equation C-4})$$

Substituting Equation B-4 into Equation B-3, we get the effective charge density of DNA in 4x TBE buffer:

$$\rho_{eff} = 6\pi\mu_0\eta g_r / N = 0.034 e^- / \text{bp}$$

given free solution mobility  $\mu_0 = 3.175 \times 10^{-8} \text{ m}^2 / (\text{v} \cdot \text{s})$ , viscosity  $\eta = 1.16 \text{ cP}$ , radius of gyration of T4 DNA  $g_r = 1.31 \text{ } \mu\text{m}$  and number of base pair  $N = 166 \times 10^3$ . The result is consistent with the value obtained by Smith et al, that  $\rho_{eff} \approx 0.05 \text{ e}^- / \text{base pair}$  in 1/2 TBE buffer[189].

## APPENDIX D: DEBYE LENGTH AND HIGH FIELD GRADIENT REGION

### Debye length $\lambda_D$ :

We calculate the thickness of the Debye layer at the silica particle surface:

$$\lambda_D = \sqrt{\frac{\epsilon_0 \epsilon_b k_B T}{2e^2 N_A}} = 0.743 \text{ nm}$$

given the relative permittivity of 4x TBE buffer  $\epsilon_b = 77.232$ , with ionic strength  $I = 0.165$  mol/m<sup>3</sup>.

### High field gradient region:

The size of the high field gradient region that could cause a significant external force (Red in Figure D) is estimated from Figure D. Because trapping doesn't occur at  $E_1 = 101.0$  V/cm where the maximum  $\nabla|E|^2$  is  $0.8 \times 10^{17} \text{ mkg}^2 / (\text{s}^6 \text{ A}^2)$ , the region with  $\nabla|E|^2 > 1 \times 10^{17} \text{ mkg}^2 / (\text{s}^6 \text{ A}^2)$  was taken as the high field gradient regime. For  $E_1 = 202.0$  V/cm, the high  $\nabla|E|^2$  regime corresponds to the arc length (0, 0.024)  $\mu\text{m}$  in Figure D, which gives a central angle  $\alpha = 0.437$ . Therefore, the length of the yellow segment across which a strong field gradient occurs, shown in Figure D inset, is 34.9 nm. This distance is 47 times the Debye length, indicating the size of high field gradient region is much larger than the double layer. Figure D also shows the size of the high field gradient regime is increased with the field strength.

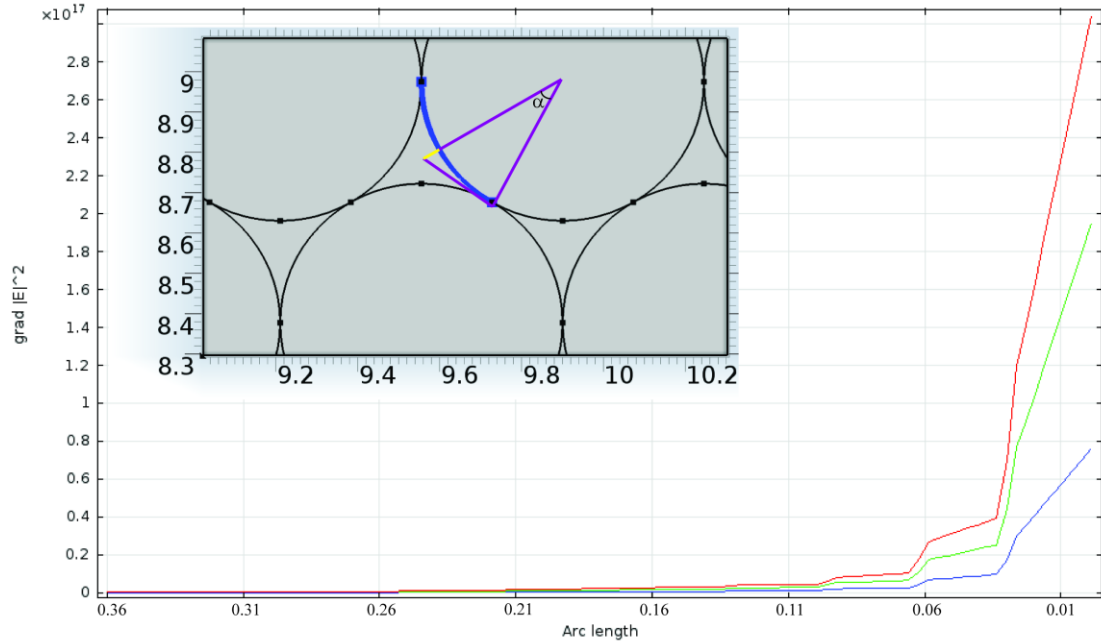


Figure D: Field gradient  $\nabla|E|^2$  (unit:  $mkg^2/(s^6A^2)$ ) on a selected buffer-silica interface (blue arc in the inset). This result is extracted from the same simulation as those shown in Figure 2-8. The red, green and blue lines represent the field gradient at an average field  $E_1=202.0, 161.6$  and  $101.0$  V/cm, respectively. The x-axis shows the arc length in micrometers, with  $x = 0$  occurring when the angle  $\alpha$  shown in the inset is zero, and arc length is a maximum of 0.361 when  $\alpha = 60^\circ$ .

## APPENDIX E: QUANTITATIVE ANALYSIS

The error of estimating the concentration of an unknown,  $s_x$ , from the measured value  $y$  and an internal standard-based calibration curve were analyzed using the least-squares method:

$$s_x = \frac{s_y}{|m|} \sqrt{\frac{1}{k} + \frac{nx_u^2 + \sum(x_i^2) - 2x_u \sum x_i}{n \sum(x_i^2) - (\sum x_i)^2}}$$

where  $m$  is the slope,  $k$  is the number of measurements made of the unknown,  $n$  is the number of  $(x_i, y_i)$  data sets used in the calibration curve,  $x_u$  is the concentration of the unknown determined from the calibration curve and  $s_y$  is the standard deviation of the measurements, given by:

$$s_y = \sqrt{\frac{\sum(y - y_i)^2}{n - 2}}$$

## APPENDIX F

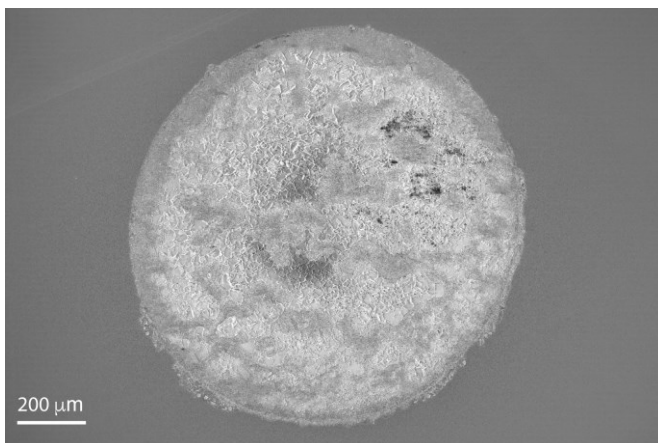


Figure E: SEM image of the entire sample spot shown in Figure 3-2b. 1.5  $\mu\text{l}$  aCSF sample was diluted with methanol (50/50, v/v), spotted on 1% pFSiCl<sub>3</sub> coated surface and air dried at ambient condition. The electrolytes in the sample deposited on the entire sample spot. Crystals of salt did not form due to the presence of methanol.